Numerical Simulation of Compartment Fires: Investigation of Opening Flow Characteristics

Joint Postgraduate Course:
Computational Mechanics

Author:
Dimitrios Pikiokos

Supervisors:

Professor M. Founti

Research Associate D. Kolaitis

ATHENS, February 2016

Acknowledgements

First and foremost I would like to thank Prof. Maria Founti and Research Associate Dionysios Kolaitis, my teachers and guides through the process of making this study. Your encouragement, help and instructions were more than necessary and deeply appreciated. Thank you for believing in me.

I would also like to thank my friend Panagiotis Stamatopoulos for encouraging me to dive into the field of fire research -with this thesis being a small step towards that goal-, while providing me information and help in the form of ideas and troubleshooting. The value of these is priceless.

Last but not least, I cannot thank my family enough for their never ending support and encouragement in every aspect of my life and studies.

Εισαγωγή

Η έκλυση θερμότητος λόγω φωτιάς σε διαμέρισμα κινεί τον περιβάλλοντα αέρα ως αποτέλεσμα διαστολής και άνωσης αερίων. Τα πεδία ροής που δημιουργούνται σε ένα καιόμενο διαμέρισμα είναι τρισδιάστατα. Στην παρούσα εργασία παρουσιάζονται υπολογιστικές προσομοιώσεις με χρήση του κώδικα FDS, με στόχο την βέλτιστη μοντελοποίηση του αναπτυσσόμενου ροϊκού πεδίου και την επαλήθευση των υπολογιστικών αποτελεσμάτων μέσω σύγκρισης με τα διαθέσιμα πειραματικά δεδομένα.

Οι προσομοιώσεις αφορούν δύο πειραματικές διατάξεις, μία μικρής και μία μεγάλης κλίμακας. Λεπτομέρειες σχετικά με τα πειράματα μπορούν να βρεθούν στις δημοσιεύσεις των Suard et al (2015) και Bryant (Bryant, 2009a, Bryant 2009b) για τις αντίστοιχες πειραματικές διατάξεις. Μέσω των προσομοιώσεων διερευνήθηκε η επίδραση της χρήσης διαφορετικών πλεγμάτων διακριτοποίησης, με υπολογιστικά κελιά μεγέθους από 10mm έως 50mm για το διαμέρισμα μικρής κλίμακας, και από 30mm έως 100mm για το διαμέρισμα μεγάλης κλίμακας. Επίσης διερευνήθηκε η επίδραση χρήσης αδιαβατικών έναντι θερμικά αγώγιμων τοιχωμάτων και ενός εύρους διαφορετικών ισχύων για την πηγή της φωτιάς. Οι ισχείς περιλαμβάνουν τιμές 15.5kW και 21.7kW για το διαμέρισμα μικρής κλίμακας, και 160kW και 320kW για το διαμέρισμα μεγάλης κλίμακας. Οι προσομοιώσεις που υιοθετούσαν αδιαβατικές οριακές συνθήκες στα τοιχώματα απεδείχθησαν υποδεέστερες εκείνων που χρησιμοποιούσαν θερμικά αγώγιμα τοιχώματα, για όλα τα φυσικά μεγέθη που εξετάστηκαν, για όλο το εύρος ισχύων φωτιάς. Οι συγκρίσεις μεταξύ των προλέξεων και των πειραματικών μετρήσεων αφορούν εν γένει κατανομές θερμοκρασιών και ταχυτήτων στο άνοιγμα των διαμερισμάτων.

Η διερεύνηση υπέδειξε ξεκάθαρα την υπεροχή των μοντέλων με πυκνό πλέγμα, για όλες τις περιπτώσεις που εξετάστηκαν. Τα υπολογιστικά πλέγματα διαστάσεων 10mm και 50mm για τα διαμερίσματα μικρής και μεγάλης κλίμακας αντίστοιχα, απεδείχθησαν επαρκώς πυκνά για την ικανοποιητική μοντελοποίηση των παραμέτρων του ροϊκού πεδίου.

Αλγεβρικές συσχετίσεις υπολογισμού του ρυθμού ροής μάζας με πολλαπλές αναφορές στη βιβλιογραφία, συγκεντρώθηκαν, τροποποιήθηκαν κατάλληλα και ομαδοποιήθηκαν. Κατόπιν απλοποίησης τους, οι εξισώσεις διαχωρίστηκαν σε δύο κατηγορίες: υπολογισμού ρυθμού εισροής μάζας αέρα και υπολογισμού ρυθμού εκροής μάζας καυσαερίων. Τα καλύτερα αριθμητικά αποτελέσματα επιδεικνύουν κατ' απόλυτες τιμές 9%-11% υπερεκτίμηση του ρυθμού εισροής αέρα και 4%-6% υπερεκτίμηση του ρυθμού εκροής καυσαρίων.

Οι προαναφερθέντες στατιστικοί μέσοι χρησιμοποιήθηκαν περαιτέρω σε μεταξύ τους συγκρίσεις, για τον καθορισμό του βέλτιστου ζεύγους τιμών συντελεστών παροχής, για τα πειράματα που μελετήθηκαν. Τα αποτελέσματα δείχνουν μια μικρή υπεροχή του ζεύγους τιμών που προτάθηκε από τους Prahl και Emmons (1975), συγκεκριμένα 0.68 και για τους δύο συντελεστές.

Τέλος, διερευνήθηκε η αλγεβρική σχέση του Rockett (1976) για τον υπολογισμό του ύψους της θερμικής ασυνέχειας στο εσωτερικό του διαμερίσματος. Τα αποτελέσματα έδειξαν τη σαφή υποτίμηση αυτού, με μέσο σχετικό σφάλμα -13.5%. Το αποτέλεσμα αυτό επήλθε μετά από τη σύγκριση $14^{ων}$ πειραματικών μετρήσεων των Steckler et al (1982) με τα αποτελέσματα της αλγεβρικής σχέσης του Rockett (1976), για πειράματα με χρήση πόρτας ως μοναδικό άνοιγμα στον περιβάλλοντα χώρο.

Abstract

The release of heat due to compartment fire causes the surrounding gases to move as a result of expansion and buoyancy. Flow fields encountered in enclosure fires are highly three-dimensional and span a large spatial extent. CFD simulations using the FDS code are presented, aiming to determine the best modelling approach to achieve optimum agreement between numerical and experimental data and the most accurate simulation of the flow field.

Two experimental configurations were simulated, ranging from a small scale to a large scale compartment. Details of the experiments can be found in the work of Suard et al. (2015) and Bryant (Bryant, 2009a, Bryant 2009b) for each configuration respectively. The simulations investigated the effects of grid cells' sizes from 10mm to 50mm for the small scale compartment and from 30mm to 100mm for the large scale compartment. Investigation has been made in the effects of setting both adiabatic or conductive wall boundary conditions and different heat release rates for the fire, including the four values of 15.5kW, 21.7kW for the small scale and 160kW and 320kW for the large scale compartment. The adiabatic simulations proved to perform poorly in almost all aspects for the examined quantities, at any heat release rate examined. The comparisons between experimental measurements and numerical simulation results, focused mainly on the temperature and velocity profiles at the opening of the enclosures.

The investigation showed clear superiority of the fine meshed models, for all the cases examined. A grid of 10mm for the small scale and 50mm for the large scale compartment were able to model the flow field parameters adequately.

Algebraic relations of the mass outflow and inflow rates of the burning compartment, dependent on various quantities, underwent careful manipulation in order to appear simplified and grouped since many of them appeared multiple times in the literature from different sources. The correlations were separated in two categories, estimating the mass flow rate of either the inflow or the outflow. The best performance in terms of mean absolute error was 9%-11% overestimation of the inflow and 4%-6% overestimation of the outflow.

The error values of the aforementioned comparisons were used to further compare the results with one another in order to determine which discharge coefficient is most suitable for the cases examined. The results were doubtful giving a small lead to the values proposed by Prahl and Emmons (1975), namely 0.68 for both the inflow and the outflow coefficients.

The average relative error of the correlation provided by Rockett's (1976) work was also examined giving an underestimation of the thermal discontinuity height by 13.5%. The results were acquired after careful comparison to 14 experimental results using a doorway as their only opening, provided by Steckler et al (1982).

Nomenclature

Main Variables

Symbol	Unit	Short Definition
A	m^2	area of opening
A_t	m^2	area of the enclosing boundaries subjected to heat transfer (wall area minus A)
b	m	width of opening
B_C	m	height of sill
C_d	-	discharge coefficient of the room
c_p	kJ/kg/K	specific heat of gases
D	m	hydraulic diameter of burner (4*area/perimeter)
D*	m	characteristic fire diameter
e	-	fraction of the convective heat loss in the gas outflow
g	m/s^2	acceleration of gravity
H_O	m	height of opening (lintel height) with the respect to the sill height
h_w	$kW/(m^2K^1)$	overall heat transfer coefficient to the ceiling and walls
$\dot{m}$	kg/s	mass flow rate
Pr	-	Prandtl number
p	$kg/(s^2m)$	pressure
Q	kW	fire heat release rate
Q_C	kW	fire convective heat release rate
r	-	density ratio ($=\rho_{out}/\rho_{amb}$)
Re	-	Reynolds number
Sc	-	Schmidt number
s	-	stoichiometric air/fuel ratio
T	K	temperature
v	m/s	flow velocity at the opening
W_C	m	compartment width
Z_D	m	height of thermal discontinuity in the room
Z_N	m	height of neutral plane from the floor

Greek Symbols

δt	s	time step
δx	mm	nominal size of a mesh cell
δ*	-	layer depth (ZD) correction
η	-	domain extension factor
μ	kg/(sm)	viscosity
ρ	kg/m3	fluid density
σ	kg/(s3K4)	Stefan-Boltzmann constant
τ	$kg/(s^2m)$	stress
ϕ	-	stoichiometric oxygen/fuel ratio

Subscripts

amb	ambient
bottom	of the upper lower cold layer of gases in the room
fuel	upper hot layer of gases in the room/fire gasses that are later entrained out of the room
in	coming into the room/of the inflow
out	vented out of the room/of the outflow
room	lower cold layer of gases in the room/incoming gases entrained by the inflow
t	turbulent
top	of the upper hot layer of gases in the room

Table of Contents

1. Introduction

Fire is the term assigned to the rapid oxidation of a material in the exothermic chemical process of combustion. The products of fire vary according to the flammable/combustible material and are spread in the surrounding space in the form of hot gases and particles of a variety of sizes. Heat and light are also released, whose amount in strongly dependent on the fresh air and fuel supply.

Building fires can be destructive for the entire building structure and (even worse) responsible for the losses of human lives. Fire safety is a set of practices and a necessity that is always under investigation and subject to improvements in order to prevent and/or minimize damage and destruction caused by fire. Fire safety measures include those that are planned during the construction of a building or implemented in structures that are already standing, and those that are taught to occupants of the building.

As stated by Markatos et al (1982), apart from experience gained from real fires, physical models of fire have been the main source of information guiding the development of fire legislation. Computers and computational methods have been used since the early 1970'-s to approach fire safety engineering problems in design and operations. The mathematical modelling of fire and smoke spread in enclosures is currently and has been an important research topic due to its significance on life safety of predicting them accurately.

Several research efforts have been performed in order to better and further understand the physics governing a post flashover fire in an enclosure. Research on enclosure fires may be a small step towards the study of full scale buildings, but are nevertheless of highest importance. Enclosure fires will be the field of research made for this study.

It is usually assumed that a hot layer temperature of 600^{o}C represents the transition from a growing fire to a full room-involvement fire, termed *flashover*. It is known that the time to flashover or whether it will occur, is determined by such factors as room size and shape, wall insulating properties and fuel location within the room. The primary factors, however, are the fuel heat release rate and the available air supply. These two factors are themselves related (Babrauskas, 1980). After flashover, all available surfaces will be ignited, creating more turbulence, and leading to a reasonably "well-mixed" environment inside the compartment. At this stage, the induced airflow becomes dependent on the temperature and resulting buoyancy inside the compartment, with the flow restricted by the size of the vent opening (Yii et al, 2007).

It is known that during a naturally ventilated compartment fire, outside air will be drawn into the compartment through vent openings, such as doors or windows (Figure 1.1). This vent flow is a direct result of buoyancy forces generated by the fire. The rate of airflow into the compartment affects the fuel mass loss rate and the heat release rate inside the compartment, and hence the resulting gas temperatures for the duration of the fire.

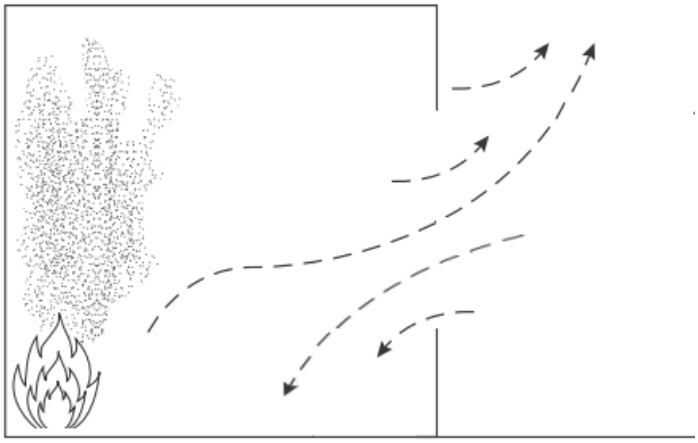

Figure 1.1: Flow through a vent in the enclosure

The amount of air flowing into the fire compartment varies at different stages of the fire. During the early stages, a small fire could be represented as an axisymmetric plume emanating from a single point source, rising toward the ceiling, forming a smoke layer underneath the ceiling level.

The amount of air being drawn into the compartment is largely dependent on the entrainment of the fire plume, where the outside air enters through the opening before being entrained into the rising plume. As the burning progresses, the hot upper layer deepens with increasing temperatures. The upper zone (smoke layer) will increase in size, filling the compartment as the fire grows and mixing occurs at vents. This stage of fire evolution is called pre-flashover.

A consideration of the flow dynamics can show the justification for a homogeneous model, at least to generalize trends, in compartment behavior. As a simplification, but without a loss in generality, the compartment gas is assumed to be homogeneous, as in post-flashover conditions. Since the gas is well stirred and does not have molecular weight variations, the density is uniform. In actuality, the gas properties are stratified, and a two-zone model as shown is Figure 1.2 is more correct (Quintiere, 2002).

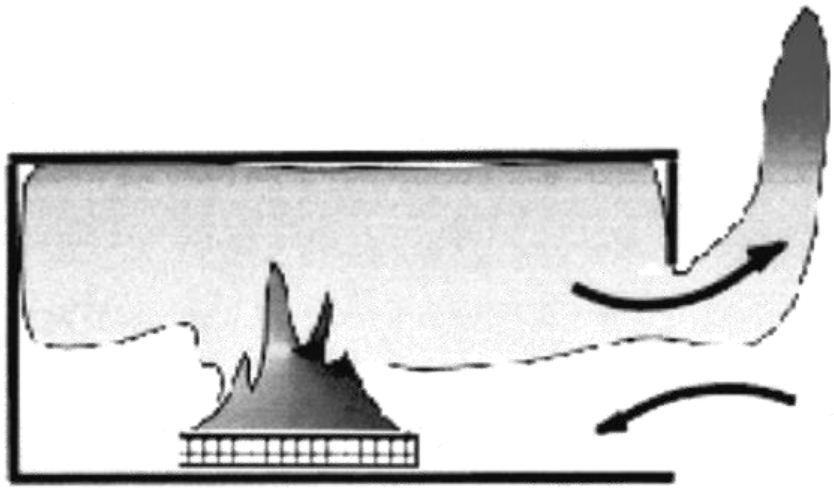

Figure 1.2: Graphic presentation of the stratified two-zone model

The prediction of flow through doors or windows due to compartment fires is important for two reasons. First, it bears on the accuracy of compartment fire growth models. Secondly, it is important in order to predict the effluent rate of combustion products and flames to the surroundings. Since most mathematical fire growth models are approximate, it is necessary to evaluate their accuracy and consistency with experimental data.

The main aim of this study is to simulate and seek for a deeper analysis of the flow phenomena through an opening of a burning enclosure.

Physical assumptions were made -in agreement with the existing bibliography- in an attempt to determine the best existing correlation between a few of the most popular describing the mass flow rates through a vent opening. The original correlations will be presented, modified as needed for the reader to easily understand the variables used in the equations by their respected authors.

A computational approach is also presented using the open source FDS code, which is a Computational Fluid Dynamics code, in order to simulate the respective phenomena. Predictions are validated using available experimental data. FDS is a CFD tool using the Large Eddy Simulation (LES) approach, which is used to predict/simulate the flow phenomena during a compartment fire. Special attention is paid on the opening's flow characteristics.

The parameters representing physical quantities (e.g. heat release rate, velocity, radiation factors) are averaged over each zone of interest. The equations used (e.g. mass, momentum, energy, chemical species concentrations), are solved with the highest practically possible special and temporary resolution, in order to yield distributions of the dependent flow variables, thus providing more detailed information on the flow structure. For this reason, CFD modelling is considered to be a more general and accurate method to deal with the problem of compartment fire (Stavrakakis and Markatos, 2009).

Considering that the computational results are valid within a tolerance limit (compared to the experimental data), the simulations' results are put into comparison in order to determine the most precise for each test case. Assessment of various quantities, over predefined locations, points out the simulations that represent the physics of the experiments the best.

The simulations examined the effects of several factors on the flow field, such as the thermal properties of the walls, the computational mesh resolution and the fire strength. The influence of those factors in the results of the simulations is obvious in the presented comparative graphs.

2. Opening Flow Characteristics in Compartment Fires

Fully developed fires in enclosure have been studied extensively for years but as a problem they are still considered to be open to a more accurate solution.

The physics of the development of the fire have been approached from two sides. Many scientists followed the single, so called well-mixed model which by generalizing assumes an almost uniform condition in the room. Others used the more modern approach of a two-zone model defining two almost separate layers of air in the enclosure. Since the experiments examined in this study concern pre-flashover conditions, the two-zone model is adopted for the analytical approach of the phenomena.

As it has already been mentioned, after flashover, the ignited surfaces will create such turbulence in the room, leading to a reasonably “well-mixed” environment inside the compartment. The vent flow that will be discussed is a direct result of buoyancy forces generated by the fire. This ‘well-mixed’ condition has been the underlying assumption made by Kawagoe (1958) during his pioneering work in vent flow modeling. Pressure in the compartment fire is essentially atmospheric, and flows occur at vents due to hydrostatic pressure differences. For this study, since flashover does not occur in any of the examined experiments, a two-zone model of uniform properties will be used. Mixing is allowed to occur into the lower layer due to plunging on the cold door jet through a portion of the upper layer. Utiskul (2006) developed a model for this mixing effect, based on experiments.

It is known that the fire product gas temperature is significantly higher than the surrounding, resulting in increasing the volume of the fire gases. That combined with the fact that the produced gasses’ mass is a constant, results in a lower density. It is this decreased density compared to the ambient density that results in buoyant forces to actually push these heated gases up, until they meet the room ceiling.

Buoyancy is an upward force exerted by the fluid (here; plume smoke) that opposes the weight of the immersed object (surrounding fresh air). The magnitude of the buoyancy forces is proportional to the pressure difference and as Archimedes principle explains, equivalent to the weight of the fluid that would otherwise occupy the volume of the plume smoke.

After meeting the ceiling, the low density gases tend to spread in all possible directions creating a flow called ceiling jet which is illustrated in Figure 2.1. This is a simple redirection of the plume underneath the ceiling on a mainly horizontal axis. Bernoulli's principle is applied here, deriving directly from Newton's 2nd law. Since a small volume of fluid is flowing horizontally from a region of high pressure to a region of low pressure, then there is higher pressure on the “tail” of the flow boosting it forward. This gives a net force on the volume, accelerating it along the streamline.

As the fire gases keep developing, the upper layer starts to form and become thicker and the volume of fresh air in the enclosure decreases. When there is an open vent in the compartment, hot gasses, after reaching the header of the lintel of the room (window/doorway), will tend to escape from enclosure. This is expected, due to the pressure differences that occur between the room and the ambient atmosphere since the gases have a steadily increasing volume. It is essential to consider that these phenomena evolve relatively quickly at the beginning of the fire, but soon, almost “steady state” conditions occur. This part will be explained later on in this study.

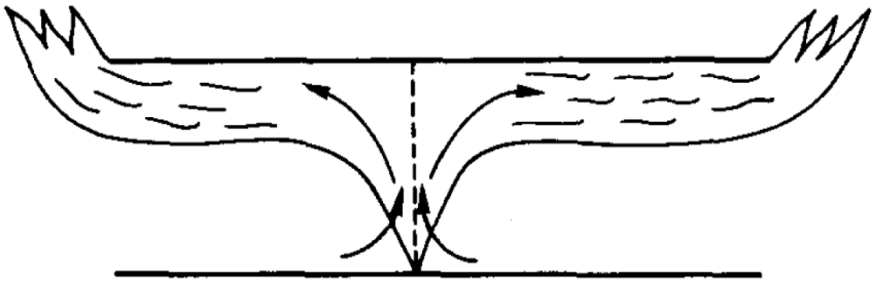

Figure 2.1: Graphic presentation of buoyant flow creating ceiling jet (Thomas, 1992)

Assuming that the ambient atmosphere's pressure is not constant, but follows a linear shape, it is presented by the purple line in Figure 2.2. The decrease in the fire product gas density described before, dictates that the line representing the pressure inside the compartment has a narrower angle. The angle is narrower due to the more intense reduction of pressure inside the compartment, than for the same height in the ambient conditions. The presentation of the pressure inside the compartment is made by the black dotted line. Both lines are straight because (since the density is uniform) the vertical pressure gradient must be linear. This is true but only in the case that the room is described as fully closed and secure or air leaks, which is not the case examined. This is still true in the "well-mixed" case used by Kawagoe but not in the two-zone model.

Having one single opening in the structure does not leave much unchanged. Pressure on the bottom (cold) layer of the room is evidently exactly the same as the ambient, although the top (hot) layer of the room is expected to have lower density as aforementioned. For that reason, the blue dotted line's top part is parallel to the black dotted line while the lower part is parallel to the ambient conditions' pressure line.

This creates a pressure and temperature discontinuity level in the room, depicted in Figure 2.2 by the angle of the blue dotted line.

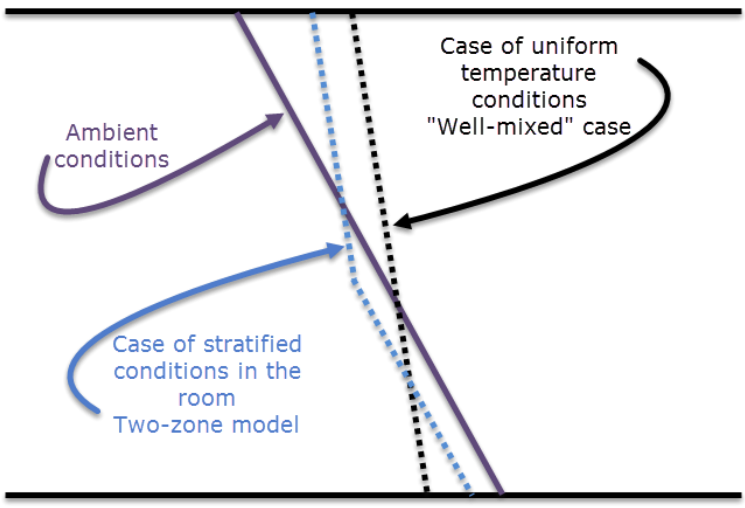

Figure 2.2: Inside pressure distributions for both cases of stratified two-zone and well-mixed models

As it has been described earlier, when the smoke layer reaches the header of the opening of the structure, the plume will start to escape the room. The given geometry's characteristics leave no other option but for the same vent occupied by the outflow to be occupied by the inflow. In this context, the conservation law and the continuity equation state that, in any steady state process, the rate at which mass enters a system is equal to the rate at which mass leaves the system.

That said, fresh (ambient) air will be subject to inflow (due to buoyancy-driven ventilation) occupying the lower portion of the wall opening, creating the two-zone model discussed earlier (Figure 2.3). After a relatively small time period, almost steady state conditions are expected to occur on the surface of the opening in terms of velocity, temperature and mass transfer rates. These "steady state" conditions are the main part of the physics that will be the focal point of the present study.

The pressure distributions presented earlier are also valid on the profile of the room's opening. This might be obvious, but the untrained eye can easily be led to the assumption that the height of the thermal/pressure discontinuity in the room is the same as at the opening. Unfortunately this is not the case in almost any geometry examined.

Experimental and computational velocity measurements have shown that the height of the discontinuity level at the opening is subject to many factors and is almost always expected to appear higher (from the floor) compared to that inside the room. This level of discontinuity (thermal/pressure/velocity etc.) on the opening will be now on referred to as the *neutral plane*.

Scientists have put effort into the exact calculation of the height of the neutral plane, but it still remains subject to improvement. It is among the intentions of this study to put some of the available relevant correlations in comparison with one another, keeping in mind that to have a practical representation of a compartment fire, details of distributions that can only be rendered by full-field model computations must be sacrificed. In that manner, measurements are averaged over certain time periods, giving representative values of the compared quantities.

The rate of the entrainment mass flow has also been extensively put into analysis, but it will not be the center of our investigation for the time being or put totally aside either. It will be taken into account in terms of turbulence created in the flow, both on the orifice and in the room. As Prétrel et al (2014) mentioned modeling of the air entrainment in the plume is necessary for the proper prediction of the stratification within the room, giving a slightly lower volume flow rate at the doorway than the well-mixed approach. Mass flow will be examined and calculated in terms of exiting/entering the room and generating (by the burning fuel) rate. Since most mathematical fire growth models are approximate, it is necessary to evaluate their accuracy and consistence with experimental data.

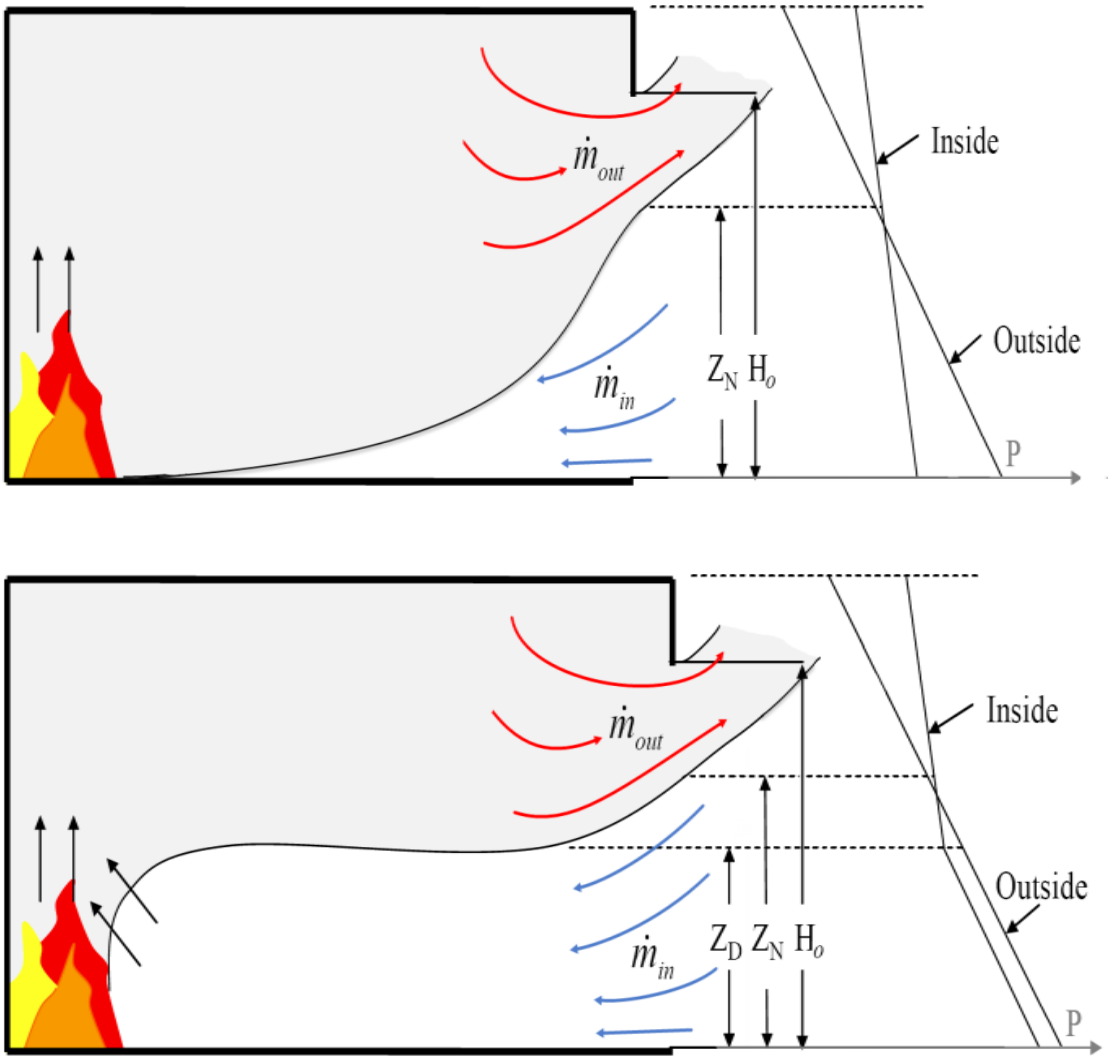

Figure 2.3: Pressure differences at the doorway for the well-mixed case (top) and the two-zone model (bottom).

2.1. Fire Induced Opening Flow

The development of a fire in an enclosure can be divided in four main stages regarding the pressure differences created at the door. As the fire grows, these pressure differences cause an increasing two-way flow through the opening. The initial stage shown in Figure 2.4 can be described as the time period before the upper gas layer reaches the horizontal orifice of the doorway. During this stage, the expansion of the gases in the compartment leads to a positive pressure as shown by the graphic illustration of pressure in the figure. This principle remains true for the second stage as well, when the gas starts to spill out of the doorway. That short period of time when the elevated pressure forces air out of the doorway is illustrated in Figure 2.5. The variables shown in the figures represent the total opening height, H, and the height of the thermal discontinuity inside the compartment, Z_D.

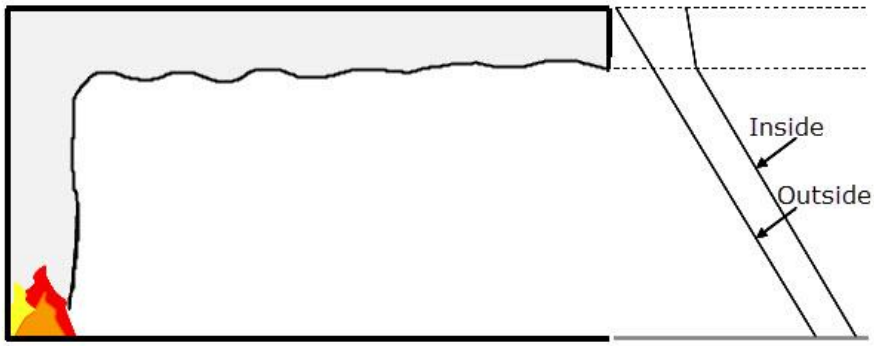

Figure 2.4: First stage of fire growth – pressure differences

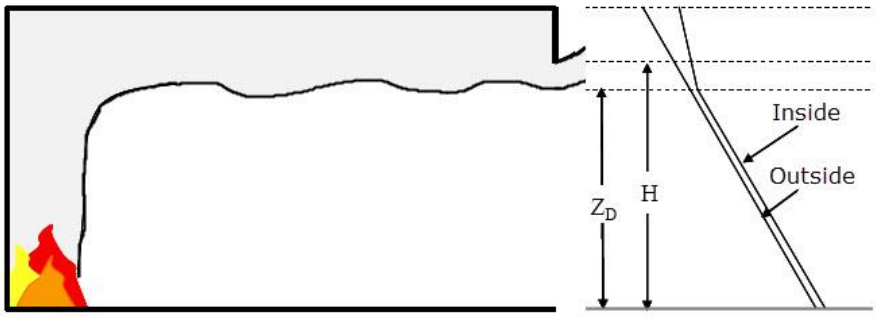

Figure 2.5: Second stage of fire growth – pressure differences

As the fire grows, a continuous flow of hot gases leaving the enclosure starts to form. When this flow descends below the top of the vent in a permanent manner, the third stage of fire growth -prior to the flashover- occurs. At that point hot fire gases leave and fresh air enters the compartment from the top and bottom of the opening accordingly. This stage is graphically illustrated in Figure 2.6 and will be explained thoroughly below. The thermal discontinuity height measured on the doorway, meaning the neutral plane height, is mentioned in the figures as Z_N.

The main assumptions made in the concept of this third stage concern the uniformity of the physical properties over and under Z_D inside the compartment. The first assumption describes the room as a completely stratified space, where no mixing occurs between the two layers of air, although this rule becomes inconsequent where the fire plume enters the upper layer; thus creating the two-zone model or stratified case. The second assumption is that each layer has uniform temperature, pressure and density throughout. Added to that, the lower layer conditions are equivalent to the ambient outside the room.

The final stage is referred to in the bibliography as the post-flashover state (Figure 2.7). During this stage the fire is fully grown and developed and the entire compartment is involved in the fire characteristics. This means that the hot upper gas layer has reached the floor making the system evolve into the well-mixed case.

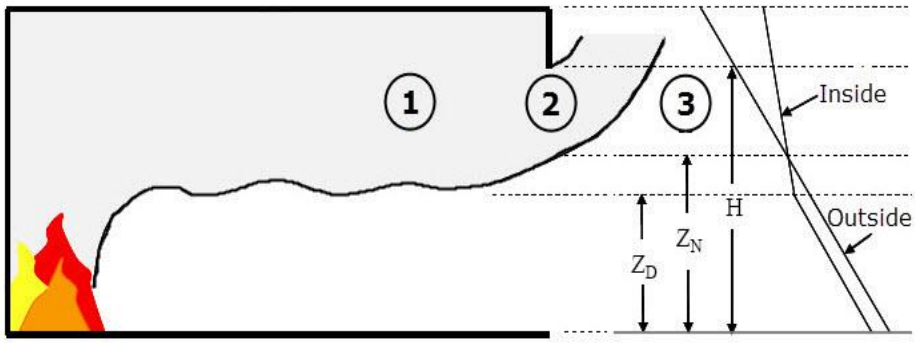

Figure 2.6: Third stage of fire growth – pressure differences – stratified case (pre-flashover fire)

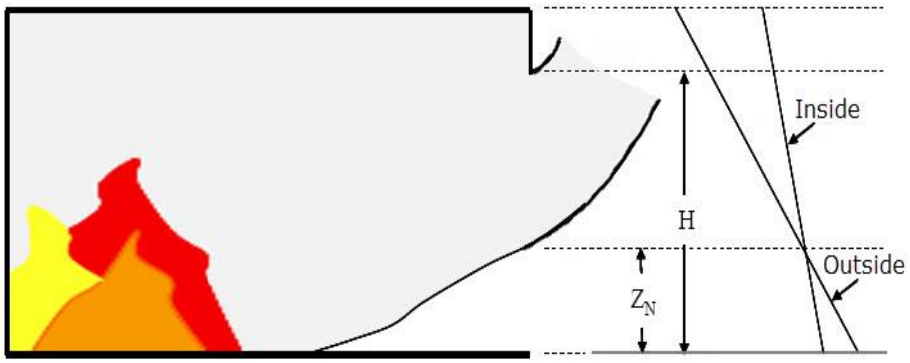

Figure 2.7: Fourth stage of fire growth – pressure differences – well-mixed case (post-flashover fire)

2.2. A General Analytical Model

The general characteristics of a fire-induced flow across an opening can be described by treating the flow as incompressible, inviscid, and driven by buoyancy. The buoyant fire plume acts as a source to push gas into the upper layer and out of the enclosure while simultaneously acting as a sink to draw gas into the doorway and into the lower layer of the enclosure. Prior research found in the literature has demonstrated that the details of the plume can be ignored when treating the flow at the doorway. Instead, a simple hydrostatic treatment based on the temperature difference between the interior of the room and the ambient is sufficient to describe the flow at the doorway. By treating the conditions created by the fire, the fire-induced flow through the doorway is analogous to and somewhat an extreme case of the natural convection flow that continuously occurs in buildings. Such natural convection flows can be described by dividing the interior of the room into two layers, a hot upper layer and a cold lower layer. The upper layer is buoyant and tends to escape the room across the top of the opening while the lower layer is continuously supplied with cool air from the ambient environment flowing across the bottom of the opening. Within the two layers gas temperature is vertically distributed with the temperature increasing as the distance from the floor increases. Gases will move from a hot room to a cooler room, so for a general description of the flow across the doorway it is practical to assume that the temperature and density field inside the room is independent of vertical position. The hydrostatic pressure difference across the doorway, Δp, is induced by the density difference, $\Delta \rho$, between the room interior and the ambient.

While on stage 3 of fire growth, the flow out of the compartment contacts the flow towards the inside, creating a location of zero flow. That location, described earlier as the neutral plane, is referred to as $\mathbf{Z_N}$ (N stands for "Neutral"). The corresponding location inside the room is referred to as $\mathbf{Z_D}$ (D originating from "Discontinuity" inside the room) describing the transition from the hot upper gas layer of the room, to the ambient lower layer of air. A graphic illustration of the variables can be found in Figure 2.6.

The flows at the opening are bidirectional with cool air inflow in the lower part and hot gas/smoke outflow in the upper part. The flow of mass entering/leaving the compartment through the vent can be calculated by multiplying the velocity of the air/gasses with the density and the area of the opening. This calculation can be seen in equation **(2.1)**. The velocity of the exiting gases can be easily derived from Bernoulli's principle and can be found in many of the references mentioned in this study (Bryant, 2009a; Suard et al, 2015; Steckler et al, 1982).

$$\dot{m} = Av\rho \tag{2.1}$$

The gasses leaving the compartment are a mixture of hot air and combustion products. As it will be later presented, the combustion products' mass can be neglected since they occupy just a very small portion of the gas. Having done this simplification it is possible to model the mass flow of the fluid leaving the compartment as if handling a simple air flow.

In order to apply Bernoulli's principle and calculate the mass flow rate out of the room it is necessary to commit to three locations of the geometry; here named Points 1, 2 and 3. The first point is located inside the room near the ceiling; the second is located on the doorway right below the lintel and the third is located outside the room, as shown in Figure 2.6.

Applying the Bernoulli equation on points 1 and 3, equation **(2.2)** is obtained as a relationship between velocity and pressure.

$$p_1 + \frac{1}{2}v_1^2\rho_1 + h_1\rho_1 g = p_3 + \frac{1}{2}v_3^2\rho_3 + h_3\rho_3 g \tag{2.2}$$

Considering that all points are on the same height then $h_1=h_3=z$ -where z is the distance from the neutral plane Z_N - and assuming that the velocities at both these locations are zero, the hydrostatic pressure difference can be calculated by equation **(2.3)**.

$$\Delta p = z(\rho_{amb} - \rho_{out})g \tag{2.3}$$

It is evident that pressure difference is a function of height from the neutral plane and that the greater the distance from Z_N, the higher the pressure difference will be. In that manner, at neutral plane height it will be equal to zero.

It is now time to link the hydrostatic pressure difference to the velocity of flow in the opening in order to be able to calculate mass flow rate through it. Considering Bernoulli's equation once again for points 1 and 2 (inside the room and on the doorway) equation **(2.2)** is transformed into equation **(2.4)**. Bearing in mind that v_1 is equal to zero, both points are on the same height, and that the density of the gas inside the enclosure is the same as that exiting through the vent, equation **(2.5)** is produced.

$$p_1 + \frac{1}{2}v_1^2\rho_1 + h_1\rho_1 g = p_2 + \frac{1}{2}v_2^2\rho_2 + h_2\rho_2 g \tag{2.4}$$

$$\Delta p = \frac{1}{2}v_{out}^2\rho_{out} \tag{2.5}$$

Solving equation **(2.5)** for v_{out} and substituting Δp from equation **(2.3)**, an expression for the hot upper gas layer velocity can be obtained, presented in equation **(2.6)**.

$$v_{out} = \sqrt{\frac{2z(\rho_{amb} - \rho_{out})g}{\rho_{out}}} \tag{2.6}$$

At this point the velocity has been expressed at a certain height z from the neutral plane. It is important to mention that since the same technique can be used in order to calculate the flow of air in the room as well, no matter the direction one moves away from Z_N, the sign of z must remain unchanged representing the direction in which the distance from Z_N is measured.

In vents where the pressure difference remains unchanged over the entire vent area, the velocity can be said to be constant as well. Examination close to the edges of the doorway would prove this assumption to be false, inserting a flow coefficient C_d in equation **(2.1)** to take that into account. Determining the value of the discharge coefficient has been the subject of many research studies. The values assigned to this variable will be discussed later in the study and a comparative analysis will be presented.

Since the mathematical model has so far been based on the outflow, it would be better to write the equation of the mass flow rate in terms of outflow variables, creating equation **(2.7)**. Note that in the same way, the mass flow rate entering the enclosure in the pre-flashover stage can be calculated as well.

$$\dot{m}_{out} = C_d A v_{out}\rho_{out} \tag{2.7}$$

The velocity of outflow gases will change over the height of the doorway (in this case from Z_N to H_O, where H_O is the net vent height). Given that the neutral plane is the zero flow point, integrating in terms of height (dz) from Z_N where z=0 to the top of the doorway (H_O) where z=H_O-Z_N will provide the total mass flow out of the enclosure. Substituting equation **(2.6)** in the integral produces equation **(2.8)** where the variable "b" stands for the vent width:

$$\dot{m}_{out} = \int_0^{H_O - Z_N} C_d b \sqrt{\frac{2z(\rho_{amb} - \rho_{out})g}{\rho_{out}}}\rho_{out} dz \tag{2.8}$$

Relocating the constants from inside the integral and performing some simplifications produces equation **(2.9)**,

$$\dot{m}_{out} = C_d b \rho_{out} \sqrt{\frac{2(\rho_{amb} - \rho_{out})}{\rho_{out}} g} \int_0^{H_O - Z_N} \sqrt{z}\, dz \tag{2.9}$$

Where by performing the integral over the limits Z_N and H_O and rewriting the equation with some variables' relocation produces equation (**2.10)**:

$$\dot{m}_{out} = \frac{2}{3} C_d b \rho_{out} \sqrt{2g \frac{(\rho_{amb} - \rho_{out})}{\rho_{out}} (H_O - Z_N)^3} \tag{2.10}$$

Through some simple calculations the mass flow rate into the enclosure can be calculated for the two zone model. It must already be clear that in stage 3 of fire growth in the compartment, there is a significant pressure change between the flow levels Z_N and Z_D, thus creating different flow conditions. That noted it is essential to divide the inflow in two separate flow rates, from the vent's sill (or in this case the floor) to Z_D and from Z_D to the neutral plane Z_N.

For 0 to Z_D:

Working in the same way as before, assuming that the pressure in this area is constant, the velocity of the gases entering the enclosure should therefore be constant. Since velocity in this case is not a function of height, integration is not necessary but rather a replacement of equation **(2.6)** in equation **(2.7)** at the height $z=H_N-H_D$. The height H_D standing below H_N can be therefore described to be $(H_N - H_D)$ high. This results in equation **(2.11)**.

$$\dot{m}_{in,low} = C_d b H_D \rho_{amb} \sqrt{\frac{2(H_N - H_D)(\rho_{amb} - \rho_{out})g}{\rho_{amb}}} \tag{2.11}$$

For Z_D to Z_N:

In this area the velocity of air is a function of height making it necessary to integrate in terms of dz. As before, the area the integration is measured from H_N, where z=0, to Z_D, where $z=H_N-H_D$. Integrating as in equation **(2.8)** the final equation for the inflow from Z_D to Z_N is produced as in equation **(2.12)**.

$$\dot{m}_{in,high} = \frac{2}{3} C_d b \rho_{amb} \sqrt{2g \frac{(\rho_{amb} - \rho_{out})}{\rho_{amb}} (H_N - H_D)^3} \tag{2.12}$$

Total mass inflow:

The total mass inflow is given by equation **(2.13)**, adding equation **(2.11)** and equation **(2.12)** into the sum of the two separate flow rates. After simplifying the equation the result produced is equation **(2.14)**.

$$\dot{m}_{in} = \dot{m}_{in,low} + \dot{m}_{in,high} \tag{2.13}$$

$$\dot{m}_{in} = \frac{2}{3} C_d b \rho_{amb} \sqrt{2g \frac{(\rho_{amb} - \rho_{out})}{\rho_{amb}} (H_N - H_D)} \left(H_N + \frac{1}{2} H_D \right) \tag{2.14}$$

It is true that the conservation laws demand that the inflow must equal the outflow in terms of mass. That is only true though if the mass produced in the compartment is neglected. A more precise

expression would describe the same principle as in equation **(2.15)**. Neglecting the fuel mass production is a common practice due to the minor significance of terms so small in mass flow calculations. It is therefore often assumed that the inflow rate instead of being lower than the outflow rate is equal to it.

$$\dot{m}_{out} = \dot{m}_{in} + \dot{m}_{fuel} \tag{2.15}$$

2.3. Literature Review on Analytical Models

Prahl and Emmons (1975) studied flows through a single window and single door opening with a reduced-scale kerosene/water analog experiment. Their work has been extensively revised, tested and praised by the majority of scientists in their field. Having no accurate prior experimental data to safely calculate mass flow rates through an opening, Prahl and Emmons (1975) designed and experimented on an one of a kind analog of two immiscible common fluids, kerosene and water. That way, inflow effects where for the first time included in the measured results, although based on other scientists' preliminary findings. Maximum possible buoyant flow through the opening was stated to occur when the corresponding flow depth becomes equal to the height of the opening.

Inflow and outflow orifice coefficients were determined and found to be significantly different at low Reynolds numbers (Re is based on flow height), but as the Reynolds number increased they tended to a common value of approximately 0.68. Nakaya et al (1986) came to the same results during their full-scale compartment tests using a big fire source (Temperatures up to 1000^{o}C). This number would be kept constant until this day except for some cases that would either improve it or reevaluate the existing calculations.

Steckler et al (1984) performed a full scale fire experiment to study flow coefficients through room openings. Their novelty approach to the orifice coefficients suggested that a linear fit to their data, yields a mean value of 0.73 for the outflow coefficient and of 0.68 for the inflow coefficient. These constants were used in another study by Steckler et al (1982) and Quintiere et al (1984), and referred to by others, as being a good approximation (Johansson and Van Hees, 2014).

Kawagoe (1958) was the first to empirically fit his data to get values of outflow coefficient C_d which he found to range between 0.5 and 1.0 in his experiments. Coefficient C_d equal to 0.7 was used in many studies as well. Most of these studies where partly work of Quintiere (Quintiere, 2002; Quintiere and Wang, 2009; Johansson and Van Hees, 2014; Karlsson and Quintiere, 1999). Values close to 0.7 for the flow coefficient were used by other researchers as well (Steckler et al, 1984; Rockett, 1976).

Kawagoe (1958) in his studies assumed a uniform temperature for fully developed fires and computed the vent flow based on stagnant hot and cold gas reservoirs on either side of the vent. Later, Rockett (1976) extended the theory of uniform temperature profiles in the compartment for fully developed fires, and computed the vent flow considering the gas in the room to be composed of a hot upper layer and a cold (ambient) lower layer. Cold air is entrained by the fire up to this thermal interface. Only the fire plume mass flux crosses this interface. It is this two-zone model that was used in this study and that is underlying all the following studies. Rockett's work provided correlations for both inflow and outflow rates, considering the orifice flow coefficients C_d to vary from 0.6 to 0.8, knowingly neglecting the term considering the pressure loss within the interior of the enclosure.

Babrauskas and Williamson (1978) researched post-flashover compartment fires, based on the well-mixed model analyzed earlier. Their results showed that in fires, flames normally fill the upper half to two-thirds of the window. In their experiments, flashover did not occur in any case where the average gas temperature near the ceiling failed to exceed 500^{o}C. Conversely, flashover was noted in all cases when the temperature surpassed 600^{o}C. In their calculations the compartment's state was assumed to be quasi-steady and the equations' terms concerning enthalpy, room volume and gasses density changes over time were very small and therefore dropped. In another paper, Babrauskas (1980) clearly stated that the time to flashover or whether it will occur is determined by such factors as room size and shape, wall insulating properties, and fuel location within the room. The primary factors, however, are the fuel heat release rate and the available air supply rate, which two factors are themselves related. His model is regarded to be valid as long as an appropriate fuel mass loss rate can be determined. That was expected to be true since (in the model and all the data) only a discrete, single fuel item burning was considered. In actual practice though, an occupied room will surely contain more than just one piece of fuel.

The work presented in these two publications was later confirmed by Chow (2013). In his work, Chow showed a relation between the pumping action of the fire plume and the discrepancy between the analytical and the experimental data on the heat release rate. In his conclusions he suggested that estimating heat release rate in post-flashover room fires should therefore consider the air pumping action. In his work Chow (2013) also presents an empirical expression used to calculate the mass inflow rate proposed by Awbi and Nemri (1990) and Awbi (1996), which was later justified by Jiang and Chen (2003) using CFD with different turbulence models including large eddy simulation.

The relations between primary and secondary factors, are present throughout the whole extent of the phenomena described, and will be further analyzed herein. As it was mentioned before, the fuel heat release rate and the air supply rate may be related but so strongly that are furthermore dependent on each other. Another example of such dependence derives from the composition of the fire gases; while calculating the gases' density the molecular weight of the mixture has to be taken into account. Not knowing the exact composition of that mixture, it must be assumed that the existing molecular weight will be close to but somewhat larger than that of air. It is therefore not surprising that one could neglect the effect of change of the molecular weight, leaving the density to be determined primarily by its temperature. Those assumptions and the dependence created by the incomplete knowledge of the exact variables of the phenomenon prevent high accuracy calculations. A more detailed and in-depth analysis and application of these can be found in the work of Emmons (2002).

Bearing in mind how large contribution a small factor can have, scientists have always tried to examine every aspect of a problem. Steckler et al (1982) examined several fire locations within the compartment, which in the process led to re-evaluation of the validity of the two-zone model. Attempting to measure the entrainment of the fire plume they were forced to estimate the position of the rapid temperature change between the lower and upper portions of the room (thermal discontinuity level $\mathbf{Z_D}$). The profile they found inevitably led them to the conclusion that diffusion and mixing often preclude a sharp designation for $\mathbf{Z_D}$. In fact the entrainment height could only be determined within ±8% to ±50% accuracy.

Concerning fire locations their multiple tests showed that the opening flow rates are highest for the room-center fire location, lower for the back wall center position and lowest for the corner position. In their words, opening flows are greatest with the fire just inside the doorway and decrease as the fire is moved back along the room centerline. The latter configuration was also used by Quintiere et al

(1984) with some contradicting results. Nevertheless, this order reflects the decreasing effect of the door jet and the role of nearby walls in restricting flow to the fire plume. At this point it has to be noted that in their experiments, window flows are considered in only 11 cases for fires in different floor locations, whereas over 30 cases were considered for doors.

Prétrel et al. researched the effects of on the vertical density stratification assumption used above, in terms of air entrainment (Prétrel et al., 2014). Their work pointed out how the initial buoyancy flux and the dimensions of the enclosure modify the influence of temperature/density stratification and flow through the doorway. A comparison between two numerical (but no experimental) approaches aided their study.

Tewarson (1984) investigated fully developed fires in enclosure, using wood cribs as the fire source. Among his findings he presented a stoichiometric mass fraction to be the rule for the cases that fire is controlled by fuel configuration rather than enclosure openings. Ventilation factors used in the majority of cases such as the neutral plane height Z_N or $A\sqrt{H_O}$ (with A being the area of the opening and H_O being the height of the opening with respect to the height of a possible bottom sill) were disregarded, defining the stoichiometric mass fraction he used, in terms of air entrainment and fuel vapor generation rates. This parameter ($A\sqrt{H_o}$) is generally known as the ventilation factor, or more appropriately, the geometrical vent parameter, describing the physical aspect of the vent opening.

In 1995, Dembsey et al (1995) using their own experimental configuration, confirmed Tewarson's (1984) calculations. Using the same quasi-steady state conditions as Quintiere et al (1984), they found that calculating the fraction of time averaged oxygen consumption over the time averaged potential heat release rate of the fuel gave them an average value of 0.99, justifying Tewarson's (1984) calculations. Since a single vent flow coefficient is used in all their equations, Emmons stated that the best available option would be to use C_d=0.68 and expect ±10% errors in their calculations. Later on in their study, after a careful examination of the flame heights in various configurations, a conclusion was made that the entrainment offset is a function of the fire's size; the heat release rate must be influential to the entrainment rate. This opinion was in contrast to others' stating that the only fire's characteristics of importance are the perimeter and the flame temperature.

In the final phase of their study, Dembsey at al. provided McCaffrey, Cetegen et al., Delichatsios and Heskestad's comprehensive models for the entrainment rates' calculation. They were used by Dembsey et al. in comparison to their experimental and analytical results and are presented below in this study.

The steady state assumption was not an uncommon practice throughout the bibliography. Quintiere et al (1981) confirmed the fact that over most of the tests they carried, 10 minute duration was enough for steady state conditions to prevail. In their work, they pointed out that results for entrainment from free fire plume studies may not be sufficient if disturbances due to room openings are significant. Their study showed that ""wind" effects could increase the rate of entrainment over free plumes by as great as two to three times".

In the same manner, Himoto et al (2009) considered ventilation behavior of a building in actual urban area to be affected by external wind, as would the window flame behavior, too, when the building is on fire. Most of the existing tests were carried out using compartments with a single vertical opening, where flame behavior would be governed by either the configuration of the room or the

characteristics of the combustibles within it. The effect of external wind (mechanism and result influence) was clearly mentioned and pointed out, but would not be taken into account in their study.

Quintiere's work has been much appreciated by the scientific community. In his work on Fire Behavior on Building Compartments (Quintiere, 2002) he strongly emphasizes the fact that (and the reasons why) fire safety regulations should follow the most modern predictive analyses. Utilizing the interaction of fuel properties, fuel configuration and the compartment effects through analytical formulations, Quintiere attempted to illustrate the behavior of compartment fire in buildings. In his words, although his data were consistent with the theoretical trends, "*much more needs to be done to develop the needed accuracy and confidence for predictions*". Leaving space for improvement, Quintiere embraced both theories concluding that the fuel properties' parameters are as important to the flammability criteria as the ventilation factors to compartment temperature and fuel mass supply establishment.

In his work, the compartment gas is assumed to be homogenous but without embracing the one-zone model (well-mixed case) completely. The main use of this theory was in generalizing trends in compartment behavior in favor of simpler calculations. The pressure was assumed to be essentially atmospheric and flow occurred due to hydrostatic pressure differences.

Thomas' (1992) study on earlier researchers' work showed that a certain value deriving from their correlations remained reasonably constant for temperatures over 400^{o}C. That value is equal to 0.11 in his correlation, and is claimed to vary with the pattern of the flow and with the temperature. That said, one can easily understand that his theory disregards the ventilation factors that are used by other researchers, and relies on the drive by buoyancy forces generated from the hydrostatic pressure differences for the vent flow.

As it has already been mentioned, several researchers found Kawagoe's vent flow model to be underestimating the actual vent flow rate for large openings, even up to 60% for some cases where openings occupied a full wall. At large openings, vent flows tend to become dominated by smaller pressure differences associated with entrainment. Thomas et al (1967) discussed the association between fuel mass loss rates and different ventilation openings. Yii et al (2007) added to this research based on the observation that fire behaviors resulting from induced airflow for a partial wall opening and for a full wall opening are different. Based on the assumption of the "well-mixed" case conditions' in the compartment, Yii et al. suggested that the airflow induced into the compartment is strongly dependent to the geometry of the vent opening, also characterizing it by the ventilation factor AvH_O. Temperature on the other hand, showed minor significance on the airflow measurements in their experiments (for temperatures higher than 500K). In their analysis the C_d coefficient was kept the same for both inflow and outflow measurements, equal to 0.68.

These findings of Yii et al. were further analyzed in 2009 by Quintiere and Wang (2009) showing the significance of both geometries for the compartment's vent. Doorway flows are obviously important and (for the time being) much more time has been spent on their research than on window flows since they are considered to be more complex due to the effect of sill height. Quintiere and Wang claimed in their study that their flow rate formula is "*covering a wide range of realistic floor fire conditions to within 15% accuracy*". The modeling frame work used in this case was the one established by Rockett (1976) for such flows that are motivated by turbulent entrainment, rather than pressure difference.

In another publication made by the same authors (Wang and Quintiere, 2009), Utiskul's model on mixing based experiments for a two-zone model was used. That way, analytical relationships can relate the mass and energy flows in terms of the layer properties. Using a single doorway opening of varying widths for geometric simplicity, they developed a new empirical expression for the mass flow rate. This expression involved the diameter of the fire and not the firepower explicitly. The vent flow was implicitly represented in terms of the vent geometry ($A\sqrt{H_O}$).

Another novelty approach was made by Tang et al (2012) investigating under-ventilated compartment fires at high altitude using a single window opening. This high altitude (3650m) resulted in reduced pressure atmosphere of 0.64 atm instead of 1 atm (at 50m from sea level) used so far. In this case it is expected that the buoyant plume vertical temperature profile should be different from that in a normal atmospheric pressure condition.

These effects of pressure differences have not only been taken into account in the existing bibliography, but have also been a field of disagreement for many researchers. In most cases, only a couple of different density measurements were used, representing these of the ambient and in-room conditions or, in the case examined, the inflow and outflow. Not all researchers share the same opinion though.

In many cases in the bibliography the reader will come across a more detailed division of the geometry. In those cases, a different measurement was used for the ambient and in-room conditions, and another two dividing each space into an upper and a lower part (Rockett, 1976; Steckler et al, 1982; Steckler et al, 1984; Quintiere, 2002; Quintiere and Wang, 2009; Wang and Quintiere, 2009; Karlsson and Quintiere, 1999). In some special cases, the dual-value model was used, adopting one more (third) value as a more accurate auxiliary variable, describing (e.g.) the fire gases' temperature (Yii et al, 2007; Walton and Thomas, 2002) or the plume's density (Chow, 2013; Babrauskas and Williamson, 1978; Tang, 2012). The values of the variables are still averaged over each zone. It can be seen that the same differentiations occur on all three variables, including temperature and pressure, which is expected concerning the fact that all three variables are related.

Lee et al (2012) experimented on the physics of outflow through an opening in facades, and re-examined existing correlations for the maximum temperature variation along the vertical axis, with origin at half the height of the window. The authors employed Yokoi's length scale r_o (equal to the radius of a circle having half the area of the opening) to correlate temperature data of the flow outside the enclosure. Their study provided another correlation that is presented here below, ignoring the mass pyrolysis rate of fuel, referring to under-ventilated fire conditions. Assuming the same conditions, the height of the neutral plane was described to be proportional to a function of ambient and hot layer air density.

It is clear that much effort has been spent on relating ventilation factors to mass flow rates. Karlsson and Quintiere (1999) experimented on a variety of geometries and positions of vents trying to describe the flows and pressure profiles; while Lucchesi et al (2011) stated that "*the opening width has a significant effect on flow behavior and the associated spill plume*". Their experiments showed that a reduction of the width of the opening plays a significant role in enhancing air entrainment and other effects such as plume shape, with the Reynolds number kept under 6400 for all experiments. Part of their experiments is depicted in Figure 2.4 for four vent widths. Their theory is based on a one dimensional description from the Bernoulli relation, giving the vertical velocity profile which is one

main factor modifying the flow. By vertical integration of this profile the total flow rate can be acquired. One or several neutral planes are expected with the change of the opening's width.

CFD tools can be used for such research but with caution and respect to the physics of the problem. Their efficiency in these problems depends mainly on their capacity to reproduce the turbulent flow properly, especially when looking at the mixing layer where inflow and ouflow "coexist".

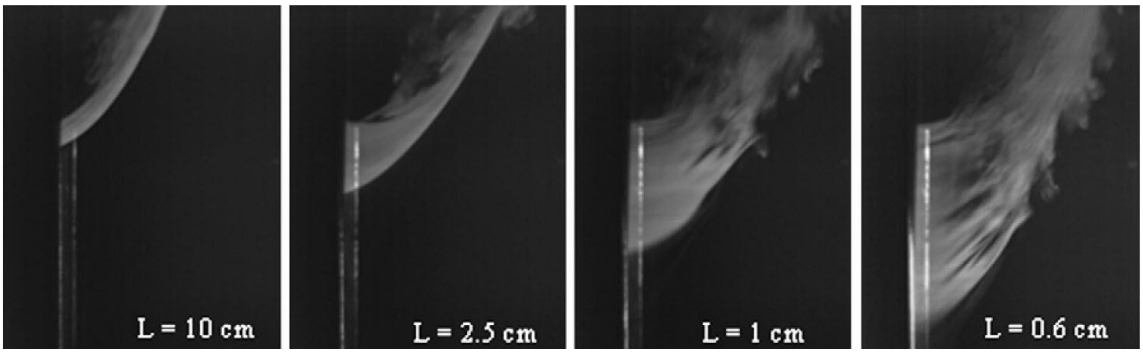

Figure 2.4: Spill plume for four opening widths (Lucchesi et al, 2011)

This mixing layer's height was used in many researchers' work, as a factor in the algebraic relations calculating the mass outflow and inflow rates of the burning compartment together with the neutral plane height. Following this line of thought, Nakaya et al (1986) experimented in a two-room geometry communicating through a single doorway. In the simplest case, Prahl and Emmons' and Steckler's assumptions were confirmed but in the case of larger openings with a steady fire heat release rate, the constants were further improved. Due to increased inflow, the average temperature inside the room decreased resulting in a lower temperature difference in the room that led to decreased flow velocities. For fires with a higher heat release rate, the vertical temperature profile inside the room suggests this approach to be more accurate.

Another product of their study was that the simple relationship between mass flow rate through the opening, and ventilation parameter AvH_O , holds even when the opening is in the wall between two rooms. Their results suggest that vigorous heat exchange must largely begin after gas flows through the opening. In their words; "*Consistent with Rockett's prediction* (Rockett, 1976)*, results show that the opening flow rate does not strongly depend on the burner intensity nor the temperature for temperatures above approximately 300°C*". Findings supporting these opinions are presented in many researches based on CFD approaches (Xiao, 2012).

It has been made obvious by now that post-flashover fires occupy the largest share of the field of study in enclosure fires. Similar simple models are lacking for the stratified pre-flashover case. In this context, Johansson and Van Hees' (2014) research provided an insight to the analytic and experimental aspects of pre-flashover fires. The produced equations are predominantly valid for temperatures higher than 200^{o}C. In their study, they attempt to give a better expression that would be used to get an estimate of the hot layer height (thermal discontinuity height) with the help of mass balance and existing plume models. Their work, utilizing expressions of Karlsson and Quintiere (Karlsson and Quintiere, 1999), showed that the hot layer would almost in all cases be situated at a height of between 0 and 60% of the opening height (above the sill) and the neutral plane would be

located above the hot layer height, as it was expected. Since the height of the neutral plane, the hot layer height and mass flow rates depend on each other, it is necessary to perform iterations of these variables using the proposed mass flow rates' expressions.

2.4. Mass Flow Rate Correlations

Correlations estimating the fire induced opening mass flow rates and heights are provided through the full extent of the bibliography. It is a purpose of this study to focus on the mass flow rates of air entering or leaving the compartment through the opening. Results and relative error calculations are determined by means of comparison with available experimental data. As shown in Table 2.1 and Table 2.2, several correlations were gathered and rewritten in terms of a uniform system of variables concerning the inflow and outflow respectively. All the correlations presented in this section concern pre-flashover conditions, adopting the two-zone model described in Section 2.1. The only exception is correlation IN6, accounting for post-flashover conditions.

2.4.1. Inflow Correlations

Prahl and Emmons (1975) did an outstanding work in optimizing the flow coefficients for both in flow and outflow and in calculating the mass flow rate through a single vent. Their correlations can be found in their publication numbered as equations (23) and (24) and are referred to as IN1 in the present study. The constant δ^* is set as equal to 0.023 since that is the proposed value when working with doorway vents, opposed to 0.05 when a window is used.

IN2 is the first most common equation used throughout the bibliography, even though it can be found with many differences mainly of aesthetic value. It can be found in Rockett's study (1976) as equation (2), neglecting the pressure loss inside the compartment, across the fuel bed and all other pressure losses due to flow within the enclosure, leading to f=1. Quintiere (2002) as well as Walton and Thomas (2002) mention the same correlation as equation (4) and Yii et al (2007) make an extensive analysis of the same correlation numbered in their study as equation (1). In their work, Wang and Quintiere (2009) gave a formula for predicting doorway flows (which was later scaled to a general formula for vent flows) giving IN2, presented in its original form by equation (4). Johansson and Van Hees (2014) provided the very same formula for predicting pre-flashover flow phenomena, which can be found in their study as equation (4).

Babrauskas and Williamson (1978) provided correlation IN3 which is one of the simplest forms expressed in terms of density differences. The original equation can be found in their study almost unchanged as equation (19).

After minor simplifications in the original equation (4) of Quintiere et al (1981), equation IN4 emerges. The factor 2.48 is not described in the text as to how it was computed, but assuming that it originated from the replacement of various constants' values, it was left unchanged.

Correlation IN5 originated from the study of Tewarson (1984) and is the one and only equation to utilize the mass flow rate of the burning fuel. Its original form can be found in text as equation (1).

Equation IN6 is the second most popular form expressing the mass flow rate of air entering the compartment and can be found in three different publications. Karlsson and Quintiere (1999) were

chronologically the first to use it in the form of their equation (5.23). Tang et al (2012) followed with the same expression in 2012 found as equation (2a) in their work, and Chow (2013) later in 2013 verified it in a different study originating from IN3, presenting it in its initial form as equation (1).

Correlation IN7 was the product of further study of Wang and Quintiere (2009) giving general forms of equations for vent flows. The original expression is found as equation (3) in their work.

One of the simplest correlations in Table 2.1 is IN8 given by Lee et al (2012), which can be traced in the source paper as (A.1). The factor 0.13 (just as with IN4) is not described in the text as to how it was computed. It was also left unchanged in the present study for the same reasons.

The final and simplest correlation in Table 2.1 is probably the most popular in the literature as well. IN9 proposes that the mass inflow rate is independent of any variable suggested by correlations IN1 to IN8 and directly proportional to the constant 0.5.

All the correlations considered in this study, used to estimate the fire induced air mass flow rate entering the compartment, are presented in Table 2.1.

Table 2.1: Correlations for estimation of air mass flow rate entering the compartment

Name	Correlation	Reference
IN1	$\dot{m}_{in} = C_{in}\rho_{amb}A\sqrt{H_o}\sqrt{2g}\begin{cases}\sqrt{\frac{\rho_{amb}-\rho_{out}}{\rho_{amb}}}\sqrt{\frac{Z_D-B_C}{H_o}-\delta^*}\left(\frac{Z_N-B_C}{H_o}-\frac{1}{3}\left(\frac{Z_D-B_C}{H_o}+2\delta^*\right)\right), Z_D \le Z_N \\ \frac{2}{3}\sqrt{\frac{\rho_{amb}-\rho_{out}}{\rho_{amb}}\left(\frac{Z_N-B_C}{H_o}-\delta^*\right)^3}, Z_D > Z_N\end{cases}$ $\delta^* = 0.05$ (window) $\quad \delta^* = 0.023$ (doorway)	Prahl and Emmons (1975)
IN2	$\dot{m}_{in} = \frac{1}{3}C_{in}\rho_{amb}b\sqrt{2g}\sqrt{\frac{T_{out}-T_{amb}}{T_{out}}}\sqrt{Z_N-Z_D}\left(2Z_N+Z_D\right)$	Rocket (1976); Quintiere (2002); Walton and Thomas (2002); Yii et al (2007); Wang and Quintiere (2009); Johansson and Van Hees (2014)
IN3	$\dot{m}_{in} = C_{in}\frac{2}{3}b\rho_{amb}\sqrt{2g\frac{\rho_{amb}-\rho_{out}}{\rho_{amb}}\left(Z_N-B_C\right)^3}$	Babrauskas and Williamson (1978)
IN4	$\dot{m}_{in} = 2.48b\sqrt{\frac{T_{amb}\left(T_{top}-T_{amb}\right)}{T_{top}^2}\left(H_o-Z_N\right)^3}$	Quintiere et al (1981)
IN5	$\dot{m}_{in} = \frac{2}{3}A\sqrt{H_o}C_{in}\rho_{amb}\sqrt{2g\left(\frac{\left(T_{out}-T_{amb}\right)T_{amb}}{{T_{out}}^2}\right)\left(\frac{H_o-Z_N}{H_o}\right)^3}-\dot{m}_{fuel}$	Tewarson (1984)
IN6	$\dot{m}_{in} = \frac{2}{3}A\sqrt{H_o}C_{in}\sqrt{2g}\rho_{amb}\sqrt{\frac{\rho_{out}\rho_{amb}\left(\rho_{amb}-\rho_{out}\right)}{\left(\rho_{out}^{1/3}+\rho_{amb}^{1/3}\right)^3}}$	Karlsson and Quintiere (2000); Tang et al (2012); Chow (2013)
IN7	$\dot{m}_{in} = 0.66\rho_{amb}A\sqrt{H_o}\sqrt{g}\left(\frac{Z_N-B_C}{H_o}+\frac{s'}{2}\right)\sqrt{\frac{T_{amb}\left(T_{out}-T_{amb}\right)}{{T_{out}}^2}\left(\frac{Z_N-B_C}{H_o}-s'\right)}$ $s' = \begin{cases}\frac{Z_D-B_C}{H_o}, \text{for } Z_D > H_o \\ 0, \text{for } Z_D \le H_o\end{cases}$	Quintiere and Wang (2009)
IN8	$\dot{m}_{in} = 0.13\rho_{amb}A\sqrt{H_o}\sqrt{g}$	Lee et al (2012)
IN9	$\dot{m}_{in} = 0.50A\sqrt{H_o}$	Thomas (1992); Babrauskas (1980); Walton and Thomas (2002); Quintiere (2002); Yii et al (2007); Karlsson and Quintiere (1999)

2.4.2. Outflow Correlations

Prahl and Emmons (1975) estimated the mass outflow rate to be expressed by their equation (22). After doing the necessary changes in the variables' names, the final form of the correlation is shown as OUT1. Again δ^* will be set as equal to 0.023 every time the equation is used in this study.

OUT2 was the most common correlation found in literature. Rockett was the first to express this in almost the same form (Rocket, 1976), found as the second part of equation (1). It can also be found expressing post flashover conditions in Babrauskas and Williamson's study (1978) numbered as equation (18). Steckler et al (1982) made an extensive study in compartment fires for many cases and combinations of fire sizes/locations and vent sizes giving the same correlation found in text as equation (5). Karlsson and Quintiere (1999) expressed it as an equation describing the well-mixed case, found as equation (5.19). The same correlation can also be seen in Johansson and Van Hees' (2014) work (mentioned as Reference No.1) as equation (3). Quintiere (2002) utilized Rocket's equation and expressed it in its most analytic form in his work described as equation (3) while Walton and Thomas (2008) came to the same conclusion found as equation (10). The most recent reference of this correlation was made by Wang and Quintiere in 2009 presented in its dimensional form in equation (3).

The third correlation, named OUT3, is the most complex one, appearing in the study of Yii et al in 2007. It is also the only correlation making use of the mass flow rate of both the inflow and the burning fuel gasses. The original form of this correlation can be found in their work as (10), demanding the calculation of both equations (4) and (8).

OUT4 is the simplest of all given correlations and is the same equation that was earlier described as IN8 (Lee et al, 2012). It was stated in the study that the mass inflow rate would be equal to that of the outflow, assuming the multiplication factor of 0.13 to be adequate to describe both the inflow and outflow and leaving the estimation of the mass flow rates dependent on the ventilation factor $AH^{1/2}$.

In a similar way Johansson and Van Hees (2014) described the mass outflow rate (OUT5) with their equation (8) giving a factor of 0.26. Using no variable for the flow coefficient, this constant was also left unchanged in the parametric analysis below.

All the correlations considered in this study, used to estimate the fire induced gas mass flow rate exiting the compartment, are presented in Table 2.2.

Table 2.2: Correlations for estimation of combustion product mass flow rate exiting the compartment

Name	Correlation	Reference
OUT1	$\dot{m}_{out} = C_{out}\rho_{amb}A\sqrt{H_o}\sqrt{2g}\frac{2}{3}\sqrt{\frac{\rho_{out}(\rho_{amb}-\rho_{out})}{\rho_{amb}^{\ 2}}}\left(\left(\frac{Z_N - B_C}{H_o}+\delta^*\right)^{3/2}-\delta^{*3/2}\right)$ $\delta^* = 0.05(\text{for windows})\ \ \delta^* = 0.023(\text{for doorways})$	Prahl and Emmons (1975)
OUT2	$\dot{m}_{out} = \frac{2}{3}C_{out}b\rho_{out}\sqrt{2g}\sqrt{\frac{T_{out}-T_{amb}}{T_{amb}}}\sqrt{(H_o - Z_N + B_C)^3}$	Rockett (1976); Babrauskas and Williamson (1978); Steckler et al (1982); Karlsson and Quintiere (1999); Quintiere (2002); Walton and Thomas (2008); Wang and Quintiere (2009); Johansson and Van Hees (2014)
OUT3	$\dot{m}_{out} = b(1+s)^{2/3}\rho_{amb}\,C_{out}^{\ 2/3}(2e)^{1/3}\left(\frac{gQ(Z_N - Z_D)}{c_p\rho_{amb}T_{out}b}\right)^{1/3}\left(\frac{2Z_N + Z_D - 3B_c}{3}\right)^{2/3}$ where $e = \left(1+\frac{h_w A_t + A\sigma T_{out}^3}{(1+s)\dot{m}_{in}c_p 10^3}\right)^{-1}$ and $s = \frac{\dot{m}_{fuel}}{\dot{m}_{in}}$	Yii et al (2007)
OUT4	$\dot{m}_{out} = 0.13\rho_{amb}A\sqrt{H_o}\sqrt{g}$	Lee et al (2012)
OUT5	$\dot{m}_{out} = 0.26b\sqrt{H_o^{\ 3}}C_{out}\rho_{amb}\sqrt{g}\left(1-\frac{Z_D}{H_o}\right)$	Johansson and Van Hees (2014)

3. Numerical Simulation of Compartment Fires

3.1. CFD Studies

Computational Fluid Dynamics (CFD) is a tool providing a look in the details of flow fields in general and a hand in the optimization of the design of systems in order to achieve better performance levels. Focusing on the phenomena taking place in a compartment fire, CFD can aid by making the analysis possible even at the conceptual stage. The effective comparison of alternative models is feasible providing deep insight into the flow field.

A CFD model is preferable in configurations where the presence of two discrete layers is not completely observed despite the long computing time. The validation process of such models is not an easy task. As Suard et al (2015) wrote, several validation studies have considered the experiments done by Steckler et al (Steckler et al, 1982; Steckler et al, 1984; Nakaya et al, 1986) as a suitable test case for CFD model validation. Even though these fire experiments were well documented, recent research works have shown that velocity measurements using bi-directional probes, as in Steckler's experiments may be overestimated in comparison with non-intrusive laser techniques as particle image velocimetry (PIV). In the field of fire science, there were some attempts to use this approach but not many formal comparisons with numerical results have been performed.

The literature on gas burner fire inducing flows through a doorway is abundant but surprisingly, only few CFD simulations, including the comprehensive modeling of an enclosure fire and a complete validation with measurements inside and outside the compartment, have been performed. A part of these numerical studies deals with the combustion process using a turbulent formulation of Navier–Stokes equations and a simplified global one-step reactive scheme. The most relevant and recent contributions of these studies, which present a validation of their results with experimental measurements, are given in Table 3.1.

For some experimental configurations with large openings, allowing a great part of heat to be convected out of enclosure, the adiabatic condition for walls gives satisfying results. In contrast, fire scenarios with a high volumetric firepower or without insulated walls, require solving the conductive heat transfer through the walls with an appropriate convective flux modeling. In this case, the convective coefficient should not be fixed, a priori, to a constant value but should take into account accurately the near-wall flows. Unfortunately, only little information concerning its calculation has been reported in the literature.

The thermal properties assigned to the walls for each study are described in the 4th column of Table 3.1 while the last column of Table 3.1 presents a relation between the fire diameter and the mesh resolution. This parameter is of great importance in simulations involving buoyancy-driven flows and will be discussed in Section 3.2.

Table 1.1: Previous CFD studies where predictions are validated against experimental data

Reference	CFD model	Experimental Data	Thermal Wall BC	HRR/vol (kW/m^3)	Mesh δx (cm)	D*/δx
Suard et al (2015)	ISIS	Suard et al (2015)	Conduction	10.6-21.7	2	7.8-10.4
Lapuerta et al (2012)	ISIS	Prétrel et al (2004)	Conduction	-	8	-
Xiao (2012)	FDS	Crocker (2008)	Adiabatic	1	10	9.6 - 17.5
Wang et al (2011)	FDS	Steckler et al (1982)	Conduction	<10	5	9.44
Stavrakakis, Markatos (2009)	SIMPLEST	Steckler et al (1982)	Adiabatic	3.7	≈0.65	4.9
Wang, Quintiere (2009)	FDS	Steckler et al (1982)	Conduction	-	6	-
Melis (2008)	SYLVIA	Prétrel et al (2004)	Conduction	1300	-	-
Merci and Van Maele (2008)	FDS	Merci and Vandevelde (2007)	Conduction	13-22	5	12.3 - 13.8 - 15.1
Pierce and Moss (2007)	SOFIE	Pierce and Moss (2007)	Conduction	11.5-27	2	16.55-11.75
Wang (2006)	JASMINE	Steckler et al (1982)	Conduction	1.9 - 9.5	5	4.88 - 9.26
Ma (2003)	FDS	McCaffrey (1995)	-	7.37-737	0.69-4.25	19.5 - 20
Yeoh et al (2003)	FIRE 3D	Steckler et al (1982)	Adiabatic	14	5	18.2
Yeoh et al (2002)	FIRE 3D	Steckler et al (1982)	Adiabatic	3.7	5	6.36
Hostikka (2002)	FDS	Pool fire	-	11.2-301.5	0.5-5	10-25.7
Hasib et al (2002)	CFX	Kumar (2004)	Adiabatic	1.3-5.1	5-15	0.6-3
Xue et al (2001)	FLUENT	Steckler et al (1982)	Adiabatic	3.7	5	6.36
Wang (2001)	SMARTFIRE	VTT (1983)	Conduction	30	20.7-30.8	8.12-12.1
Wen (2000)	CFX	NFRL (1996)	Conduction	97	10	27-42
Madrzykowski and Vettori (1999)	FDS	3146 Cherry Road, WDC (2000)	Conduction	277.8	15.9	35.7
Jia et al (1998)	CFX	FRDG*	Conduction	14	5	-
Lacour et al (1998)	-	Heselden (1971)	Conduction	5	15	-
Lewis et al (1997)	SOFIE	Steckler et al (1982)	Adiabatic	3.7	6-16	5.3-2
Chow (1996)	SIMPLE	Steckler et al (1982)	-	3.7	12	2.65

*: Fire Research and Development Group, Home Office Fire Experimental Unit.

3.2. Mesh Resolution

Since the computational domain usually encompasses a volume within a building, or the entire building itself, the most obvious and simplest numerical grid is structured rectilinear. The simplest algorithms concerning such meshes' generation directly compute nodal placement from some given function. These algorithms are referred to as algebraic algorithms. Many of the algorithms for the generation of structured meshes are descendants of "numerical grid generation" algorithms, in which a differential equation is solved to determine the nodal placement of the grid. In many cases, the system solved is an elliptic system, so these methods are often referred to as elliptic methods.

The mesh resolution is often chosen in a compromise between what it should be and what one can afford computationally. Commonly, grid sensitivity studies are performed, meaning that a computer run is repeated on a sequence of consistently refined grids until the results at all points in space do not change, or change within an acceptable margin. The grids required vary according to the case. In the bulk flow, one should aim to capture on order of magnitude of the turbulent energy cascade in order to ensure that the large scales are captured accurately. Further, one shall be careful with the choice of sub-grid scale model since a too dissipative model might lead to unwanted effects, since it could drain kinetic energy where it shouldn't. In the present study, the goal of the mesh sensitivity study is to determine a mesh resolution capable of adequately describing the flow field and the complex phenomena taking place in the experimental setup.

In most cases, multiple meshes can be processed in parallel using Message Passing Interface (MPI) libraries. In a staggered grid, scalar quantities are assigned to the center of each grid cell; vector components are assigned at the appropriate cell faces. Its main purpose is to avoid "checker-boarding" in pressure-velocity coupling by naturally representing the pressure cell velocity divergence, a very important thermodynamic quantity in the model. The disadvantage of using staggered grids is that different variable are stored at different places and this makes it more difficult to handle different control volumes for different variables and to keep track of the metrics.

3.2.1. Fire Diameter Criteria

In general, the user should start the grid sensitivity study by trying to use a relatively coarse mesh, and then gradually refine the mesh until they do not see appreciable differences in the results. Careful monitoring of the computational cost is mandatory.

For simulations involving buoyant plumes, a measure of how well the flow field is resolved is given by the non-dimensional expression $D^*/\delta x$ where D^* is a characteristic fire diameter calculated by equation (**3.1)** and δx is the proposed size of a mesh cell in all directions:

$$D^* = \left(\frac{\dot{Q}}{\rho_\infty c_p T_\infty \sqrt{g}} \right)^{2/5} \tag{3.1}$$

The quantity $\dot{Q}$ is the total heat release rate of the fire. If it changes over time, a corresponding change in resolution should be considered, adopting a mesh resolution suitable for the maximum used $\dot{Q}$. The quantity $D^*/\delta x$ can be thought of as the number of computational cells spanning the characteristic (not necessarily the physical but rather a means of estimating an appropriate grid size) diameter of the fire. The more cells spanning the fire, the better it is for the resolution of the calculation. It is better to

assess the quality of the mesh in terms of this non-dimensional parameter, rather than an absolute mesh cell size. For example, a cell size of 100mm may be "adequate," in some sense, for evaluating the spread of smoke and heat through a building from a sizable fire, but may not be appropriate to study a very small, smoldering source.

It is suggested by the literature (Mc Grattan et al, 2015) that a cell size of 10% of the plume characteristic length D^* provides adequate resolution (equation **(3.2)**), based on careful comparisons with plume correlations. Based on this criterion the required cell size for the HRR values that are used in this study are shown in Table 3.2. All D^* values were obtained using equation (**3.1)** with the values of ambient air density ρ_∞=1.204kg/m^3, specific heat c_p=1.005kJ/kgK and ambient temperature of T_∞=293K.

$$\frac{D^*}{\delta x} \geq 10 \tag{3.2}$$

The $D^*/\delta x$ for previous CFD studies has been calculated and is presented in the last column of Table 3.1. As seen in this part of some recent studies available in the literature, there seems to be a time when the limit of 10 for $D^*/\delta x$ became feasible in terms of computational cost. Depending on the implemented CFD code, the more recent the study is, the more likely the criterion is fulfilled. More recent CFD simulations (Lin et al, 2009; Ferng and Lin, 2010) re-evaluated this criterion by investigating the effects of grid sizes on the thermal radiative characteristics involved in the pool fires. After adopting even finer meshes than suggested, Lin et al (2009) found the limit of 10 for $D^*/\delta x$ to be marginally adequate and the optima grid resolution for simulating the flame height to be at $D^*/\delta x$ =13.

Table 3.2: Suggested cell sizes according to the fire diameter criterion.

Source	Suard et al (2015)	Suard et al (2015)	Bryant (2011)	Bryant (2011)
HRR	15.5 kW	21.7 kW	160 kW	320 kW
D^*	0.181	0.207	0.461	0.608
Cell Size	18 mm	20 mm	46 mm	60 mm

3.2.2. Opening Dimensions Criteria

Two alternative methods for the a priori definition of the cell size for a compartment fire simulation have been proposed by Zhao et al (2015).

The first method considers the ratio of the ventilation factor to the grid cell size as shown in equation (**3.3)**:

$$l_1^* = \frac{l_1}{\delta x} = \frac{\left(A\sqrt{H_O}\right)^{2/5}}{\delta x} \tag{3.3}$$

The second method considers the ratio of the hydraulic diameter of the opening the grid cell size as shown in equation (**3.4)**:

$$l_2^* = \frac{D_{door}}{\delta x} = \frac{\left(2b \cdot H_O \Big/ \left(b + H_O \right) \right)}{\delta x} \tag{3.4}$$

The variables in the equations stand for: *A*, opening area (m^2); *b*, opening width (m); H_O, opening height (m).

Similar to equation **(3.2)** Zhao et al (2015) proposed the criterion for l_1^* and l_2^* to be equal to 10. Such an approach can be used to estimate uncertainties associated with the grid size in the prediction of flows through the opening. Only the cases with $l_1^* \geq 10$ and $l_2^* \geq 10$ were used for the analyses made by Zhao et al (2015), expecting the mass balance deviation between the experimental and computational values to be below 4%. Based on these criteria, the cell sizes required for the experimental test cases examined in this study are shown in Table 3.3, where the overall suggested size for each case is presented in bold (minimum of each column).

Table 3.3: Suggested cell sizes according to the opening dimensions criteria.

Source	**Suard et al (2015)**	**Bryant (2011)**
$\mathbf{l_1}$	0.45054 $m^{3/5}$	1.36271 $m^{3/5}$
Suggested Cell Size	45mm	130mm
$\mathbf{D_{door}}$	0.37143 m	1.12611 m
Suggested Cell Size	37mm	113mm

3.3. Extension of Computational Domain to the Ambient

The CFD simulations performed in the present study involve compartment fires with an opening to the ambient environment. CFD simulations conducted in the study of He et al (2008) demonstrate that varying the domain extension outside an opening of a fire in enclosure has an impact on the results inside the enclosure for both fuel and ventilation controlled fires. There is therefore a need to extend computational domains in order to obtain better simulation results of room fires accounting for interactions between the flow field external to a doorway and the interior flow field.

Domain extension in different coordinate directions gave a different extent of impact on the simulation results. After an analysis made by Zhang et al (2010) on the extension of the mesh in the vertical axis, the simulation results appeared to be less sensitive to domain extension along the z-coordinate, provided that the computation domain in x-direction (direction perpendicular to the vertical vent) has been extended adequately. Mesh extension on the remaining axis (y-direction) revealed that the quantities' contours on the central plane are almost independent of the domain extension in y-direction, regardless of the extensions in the other two coordinates. In one sentence, the domain extension is more efficacious in the direction perpendicular to the vertical vent, while the effect of domain extension in the other two directions is limited.

The question arises as to how far the domain should be extended. Therefore, similar to a grid dependence study, a domain dependence study was conducted by Zhang et al (2010) to determine the appropriate computational domain for various conditions.

Modeling some external space is good practice, but exactly how much external space is required to obtain reasonable results inside the room is still not fully determined. He et al (2008) conducted a parametric study and suggested a correlation (equation **(3.5))** between the hydraulic diameter D_H of the vent opening and the effective domain extension factor, **η**:

$$\text{Effective\_Extension} = \eta D_H \ , \ \text{where } \eta = \begin{cases} 0.5 \text{ for fuel controlled fire} \\ 1 \text{ for ventilation controlled fire} \end{cases} \qquad (3.5)$$

The computational domain should be extended appropriately beyond the physically bounded walls when there are vertical openings in the walls as in the cases examined in this study, so as to ensure computational accuracy without unduly sacrificing computational efficiency. Generally, the extended domain takes into account the interaction of entrainment flows in the near door region properly and is a more appropriate approach to room fire simulations than using the unexpanded.

For fire engineering design and assessment purposes, the effective domain extension can be correlated with the heat release rate of the fire and the hydraulic diameter of the vertical vent opening. This exact correlation was examined in the research of He et al (2008). In their remarks it is recommended that the computational domain for a fuel controlled compartment fire simulation should be extended beyond vertical openings of the compartment by ½ the hydraulic diameter of the largest opening in order to maintain the validity and minimize the inaccuracy of the simulation results. For ventilation-controlled fire simulations the recommended extension is one hydraulic diameter.

As also shown by Zhang et al (2010), generally, it is sufficient to extend the computational domain beyond the vertical vent opening by one hydraulic diameter of the vent. During simulations with less extension than suggested above, the fire plume had a lesser tilt towards the back of the room. In comparison, the '*Coanda effect*', or the tilt of the plume axis was more pronounced in the result with the extended computational domain.

3.4. The FDS code

The FDS code has been used to perform numerical simulations in this study. FDS is an open source Computational Fluid Dynamics code, product of an international collaborative effort led by the National Institute of Standards and Technology (NIST) and VTT Technical Research Centre of Finland. In FDS (version 6.3.2) the Navier–Stokes equations are solved using a second order finite difference numerical scheme with a low-Mach number formulation. The turbulence model is based on Large Eddy Simulation (LES). Four models can be chosen for the subgrid-scale turbulent viscosity, with the 'modified Deardorff' as default model. FDS uses a combustion model based on the mixing-limited, infinitely fast reaction of lumped species. Lumped species are reacting scalar quantities that represent a mixture of species. A simple flame extinction model is implemented in FDS, which is based on a critical flame temperature value (T_{LFL}). In cells where the temperature drops below this T_{LFL} value, combustion does not continue since the released energy cannot raise the temperature above the value for combustion to occur. The Radiative Transfer Equation (RTE) is solved using the finite volume method (FVM). According to the fuel used, a radiation fraction is prescribed as a lower bound in order

to limit the uncertainties in the radiation calculation induced by uncertainties in the temperature field. Heat losses to the walls are calculated by solving the 1-D Fourier's equation for conduction. In the present study, the default models and constants in FDS are applied.

The Large Eddy Simulation term (LES), refers to the description of turbulent mixing of the gaseous fuel and combustion products with the local atmosphere surrounding the fire. This process, which determines the burning rate in most fires and controls the spread of smoke and hot gases, is extremely difficult to predict accurately. This is true not only in fire research but in almost all phenomena involving turbulent fluid motion. The basic idea behind the LES technique is that the eddies that account for most of the mixing are large enough to be calculated with reasonable accuracy from the equations of fluid dynamics. The goal (which must ultimately be justified by comparison to experiments) is that small-scale eddy motion can either be crudely accounted for or ignored.

The equations describing the transport of mass, momentum, and energy by the fire-induced flows must be simplified so that they can be efficiently solved for the fire scenarios of interest. The general equations of fluid dynamics describe a rich variety of physical processes, many of which have nothing to do with fires. Retaining this generality would lead to an enormously complex computational task that would shed very little additional insight on fire dynamics. The simplified equations have been widely adopted by the larger combustion research community, where they are referred to as the "low Mach number" combustion equations. They describe the low speed motion of a gas driven by chemical heat release and buoyancy forces.

The low Mach number equations are solved numerically by dividing the physical space where the fire is to be simulated into a large number of rectangular cells. Within each cell the gas velocity, temperature, etc., are assumed to be uniform; changing only with time. The accuracy with which the fire dynamics can be simulated depends on the number of cells that can be incorporated into the simulation. This number is ultimately limited by the computing power available.

The algorithm was designed to study buoyant plumes in the Boussinesq limit; that is, the fluid was assumed incompressible but included a source term for buoyancy. This approach was based on a long tradition in fire research of modeling smoke movement using dyed salt water introduced into a tank filled with fresh water. Eventually, this approach proved to be too limiting, but some of the major features of the algorithm, like the low Mach number approximation, were retained.

Numerical techniques used to solve the governing equations within a model can be a source of error in the predicted results. The hydrodynamic model within FDS is second-order accurate in space and time. This means that the error terms associated with the approximation of the spatial partial derivatives by finite differences is of the order of the square of the grid cell size, and likewise the error in the approximation of the temporal derivatives is of the order of the square of the time step. As the numerical grid is refined, the "discretization error" decreases, and a more faithful rendering of the flow field emerges. The issue of grid sensitivity is extremely important to the proper use of the model.

FDS employs total variation diminishing (TVD) schemes for scalar transport. The default for LES is Superbee, so chosen because this scheme does the best job preserving the scalar variance in highly turbulent flows with coarse grid resolution. A few other schemes (including CHARM, Godunov and central differencing) are included for completeness.

Currently, the default behavior in FDS is to revert to first-order upwinding at interpolated boundaries (mesh interfaces) for scalar transport. The reason for this is that no information is passed via Message

Passing Interface (MPI) for flow obstructions and therefore we cannot make the assumption that two upwind scalar values will be available to compute a second-order limiter. If there is no mesh refinement at mesh interfaces and the user has avoided placing obstructions within two cells of the interface, then a conservative second-order flux limiter may be invoked.

3.4.1. LES and Numerical Grid Resolution

The equations for large-eddy simulation (LES) are derived by applying a low-pass filter, parameterized by a width Δ, to the transport equations for mass, momentum and energy. For the purpose of deeper analysis, it is sufficient to think of the filtered fields in the LES equations as cell means. For example, in 1D the filtered density for a cell of width Δ calculated by equation **(3.6)**:

$$\bar{\rho}(x,t)=\frac{1}{\Delta}\int_{x-\Delta/2}^{x+\Delta/2}\rho(r,t)dr \tag{3.6}$$

The goal of the LES is to evolve the cell mean values of mass, momentum, and energy explicitly, while accounting for the effects that subgrid transport and chemistry have on the mean fields. To this end, we apply the box filter to the DNS equations to obtain the filtered equations.

Equation **(3.7)** is what is typically referred to as the LES momentum equation (analogous to the Cauchy equation—constitutive models have not been applied). All variables are primitive or computable once a suitable closure for the subgrid scale stress, τ_{ij}^{sgs} , is found.

$$\frac{\partial\bar{\rho}\tilde{u}_i}{\partial t}+\frac{\partial}{\partial x_j}\left(\bar{\rho}\tilde{u}_i\tilde{u}_j\right)=-\frac{\partial\bar{p}}{\partial x_i}-\frac{\partial\bar{\tau}_{ij}}{\partial x_j}-\frac{\partial\tau_{ij}^{sgs}}{\partial x_j}+\bar{\rho}g_i+\bar{f}_{d,i}+\overline{\dot{m}_b'''}\tilde{u}_{b,i} \tag{3.7}$$

3.4.2. Radiation

Radiative heat transfer is modelled in FDS via the solution of the radiation transport equation for a non-scattering grey gas, and in some limited cases using a wide band model. There are several limitations of the model. First, the absorption coefficient for the smoke-laden gas is a complex function of its composition, wavelength, and temperature. Because of the simplified combustion model, the chemical composition of the smoke-gases, especially the soot content, can affect both the absorption and emission of thermal radiation. Second, the radiation transport is discretized via approximately 100 solid angles. For targets far away from a localized source of radiation, like a growing fire, the discretization can lead to a non-uniform distribution of the radiant energy. The problem can be lessened by the inclusion of more solid angles. The finite volume solver requires about 20% of the total CPU time of a calculation, a modest cost given the complexity of radiation heat transfer. Some of the more interesting findings of the examination of the sensitivity of the radiation solver performed by Hostikka (2008) were:

- Changing the soot yield from 1% to 2% increased the radiative flux from a simulated methane burner about 15%.
- Lowering the soot yield to zero decreased the radiative flux about 20%.
- Increasing the number of control angles by a factor of 3 was necessary to ensure the accuracy of the model at the discrete measurement locations.
- Changing the number of spectral bands from 6 to 10 did not have a strong effect on the results.
- Errors of 100 % in heat flux were caused by errors of 20 % in absolute temperature.

3.4.3. Solution Procedure

In a given grid cell at the *n*th time step, the density, ρ^n, lumped species mass fractions, Z_α^n, velocity vector, u^n, and the Bernoulli integral, H^n, are found. In addition, for each compartment in the computational domain a background pressure, $\bar{p}^n$, exists. The temperature is found from the equation of state. These variables are advanced in time using an explicit second-order predictor/corrector scheme. The basic procedure is:

Predictor

1. Estimate ρ, Z_α and $\bar{p}$ at the next time step with an explicit Euler step. Only transport is updated at this point; the source term is time-split.
2. Compute the density from $\rho^* = \sum_\alpha (\rho Z_\alpha)^*$ and mass fractions from $Z_\alpha^* = (\rho Z)_\alpha^* / \rho^*$.
3. Compute the temperature, T^*, from the equation of state.
4. Compute the divergence $(\nabla \cdot u)^*$, using the estimated thermodynamic quantities. Note that we use the parentheses to emphasize that an estimate of the velocity field *u* at the next time step has not been computed yet, only its divergence.
5. Solve the Poisson equation for the pressure term.
6. Estimate the velocity at the next time step. This procedure guarantees that the divergence of the estimated velocity field $\nabla \cdot u^*$, is identically equal to the divergence that is derived from the estimated thermodynamic quantities $(\nabla \cdot u)^*$, in Step 4.
7. Check that the time step, δt, satisfies the stability condition. If the time step is too large, it is reduced so that it satisfies the stability constraint and the procedure returns to the beginning of the time step. If the stability criterion is satisfied, the procedure continues to the corrector step.

Corrector

1. Correct the transported species mass densities at the next time step. The background pressure is corrected similarly. A value that has been corrected for transport, has not yet been updated from chemistry or bulk mass source terms.
2. Compute the density $\rho^{**} = \sum_\alpha (\rho Z_\alpha)^{**}$ and mass fractions $Z_\alpha^{**} = (\rho Z_\alpha)^{**} / \rho^{**}$.
3. Compute the temperature, T^{**}, from the equation of state.
4. Time splitting for mass source terms. After the corrector step for the transport scheme, source terms are applied to the scalars (for both chemical reactions and Lagrangian particles). The source terms are evaluated using the results from the corrected scalar transport scheme.
5. With the updated density and composition, compute the final temperature, T^{n+1}, the equation of state.
6. Compute the divergence, $(\nabla \cdot u)^{n+1}$, from the corrected thermodynamic quantities.
7. Compute the pressure using the estimated quantities.
8. Correct the velocity at the next time step. The divergence of the corrected velocity field is identically is again equal to the divergence that was computed in Step 6.

3.4.4. Numerical Stability Parameters

FDS uses an explicit time advancement scheme; thus, the time step plays an important role in maintaining numerical stability and accuracy. The time step is dynamically adjusted at the end of the

first part of the explicit predictor-corrector time update. The constraints on the time step necessary for stability in the presence of advection, diffusion, and expansion of the velocity and scalar fields are examined in the FDS Technical Reference Guide. In addition, there are constraints that ensure accuracy of various algorithms.

The Courant-Friedrich-Lewy (CFL) Constraint:

The well-known CFL constraint given by equation **(3.8)** places a restriction on the time step due to the advection velocity. Physically, the constraint says that a fluid element should not traverse more than one cell within a time step. For LES, this constraint has the added advantage of keeping the implicit temporal and spatial filters consistent with each other. In other words, in order to resolve an eddy of size δx, the time step needs to obey the CFL constraint.

$$\mathrm{CFL} = \delta t \frac{\|u\|}{\delta x} < 1 \tag{3.8}$$

The Von Neumann Constraint:

The Von Neumann constraint is given by equation **(3.9)**:

$$\mathrm{VN} \equiv \delta t \max\left[\frac{\mu}{\rho}, D_\alpha\right]\left(\frac{1}{\delta x^2}+\frac{1}{\delta y^2}+\frac{1}{\delta z^2}\right) < \frac{1}{2} \tag{3.9}$$

This constraint can be understood in a couple of different ways. The reader should consider the model for the diffusion velocity of species α in direction i, $V_{\alpha,i} Y_\alpha = -D_\alpha \partial Y_\alpha / \partial x_i$ and would then see that VN is simply a CFL constraint due to diffusive transport. One might also think of VN in terms of a total variation diminishing (TVD) constraint. That is, if variations (curvatures) occur in the scalar field, the user would not want to create spurious oscillations that can lead to instability by overshooting the smoothing step.

Realizable Mass Density Constraint:

In an explicit Euler update of the continuity equation, if the time increment is too large the computational cell may be totally drained of mass, which, of course, is not physical. The constraint $\rho^{n+1}>0$ therefore leads to the following restriction on the time step shown in equation **(3.10)**:

$$\delta t < \rho \Big/ \left(\bar{u}_i\left(\frac{\rho}{\delta x_i}\right)+\rho\nabla\cdot u\right) = \left[\frac{\bar{u}_i}{\delta x_i}+\nabla\cdot u\right]^{-1} \tag{3.10}$$

Equation **(3.10)** basically adds the effect of thermal expansion to the CFL constraint and provides a reason to prefer CFL_VELOCITY_NORM=1 as the basis for the time step restriction. The CFL constraint is now given by equation **(3.11)**.

$$\mathrm{CFL} = \delta t\left(\frac{\|u\|}{\delta x}+|\nabla\cdot u|\right) \tag{3.11}$$

Adjusting the Time Step:

At the end of the first part of the explicit predictor-corrector time update, the time step is checked to ensure that it is within the appropriate stability bounds. If it is not, it is adjusted up or down by 10% (or until it is within limits) and the predictor part of the time step is re-run. Resetting the stability parameters can lead to simulations failing due to numerical instabilities.

3.4.6. Mass and Species Transport

The species transport equations are solved using a predictor-corrector scheme. Advection terms are written in flux divergence (conservative) form.

In the predictor step, the mass density in cell ijk at time level n+1 is estimated based on information at the *n*-th level. In DNS mode, the molecular diffusivity is based on mixture-averaged binary Fickian diffusion. In LES mode (default) the diffusivity is taken from the molecular and turbulent viscosities divided by the turbulent Schmidt number. The turbulent Schmidt number is constant with default value Sc_t=0.5. Optionally, in LES mode, the molecular and turbulent transport coefficients are treated separately, at added cost. The same applies for the thermal diffusivity.

In the corrector step, mass source terms due to chemistry, evaporation, or pyrolysis are time split and applied after the corrector step.

3.4.7. Turbulent Viscosity Model

In LES, the "turbulence model" refers to the closure for SGS flux terms. In FDS, gradient diffusion is the turbulence model used to close both the SGS momentum and scalar flux terms. A model is then required, for the turbulent transport coefficient. The turbulent diffusivity is obtained using a constant Schmidt number (for mass diffusivity) or Prandtl number (for thermal diffusivity), and so the most important transport coefficient is the turbulent viscosity μ_t. There are several different options available; the default being Deardorff's model.

- **Deardorff's Model:** By default, FDS uses a variation of Deardorff's model, where $\bar{u}$ is the average value of *u* at the grid cell center, and $\hat{\bar{u}}$ is the average of $\bar{u}$ over the adjacent cells. The model constant is set C_V=0.1.
- **The Constant Coefficient Smagorinsky Model**: modeling the eddy viscosity in the manner of Smagorinsky's analysis, this model was used in FDS versions from 1 through 5.
- **The Dynamic Smagorinsky Model**, where the coefficient C_S used in the Constant Smagorinsky Model is no longer taken as constant but rather computed based on local flow conditions.
- **Vreman's Model**: the basic idea behind this model was to expand the velocity field in a Taylor series and to test filter this field analytically, thus avoiding the expensive explicit test filtering operations necessary in the dynamic model. Therefore, this model is inexpensive. Unlike constant coefficient Smagorinsky, however, Vreman's model is convergent, making it applicable to highly resolved LES calculations.
- **The Renormalization Group Model (RNG)**, which may be used to derive an effective eddy viscosity. Unlike constant coefficient Smagorinsky, the RNG turns itself off in regions of low turbulence.
- **Thermal Conduction and Gas species Diffusion**, where the other diffusive parameters, the thermal conductivity and mass diffusivity, are related to the turbulent viscosity, while the

turbulent Prandtl number Pr_t and the turbulent Schmidt number Sc_t are assumed to be constant for a given scenario. The default value is 0.5 for both.

- **Numerical Implementation**. In the discretized form of the momentum equation, the modeled viscosity is defined at cell centers. Here C_S is 0.20, Pr_t and Sc_t are 0.5.
- **Transport Coefficients for Direct Numerical Simulation (DNS)**. There are some flow scenarios where it is possible to use the molecular properties directly. Usually, this means that the numerical grid cells are on the order of 1 mm or less, and the simulation is regarded as a Direct Numerical Simulation (DNS). For a DNS, the viscosity, thermal conductivity and material diffusivity are approximated from kinetic theory because the temperature dependence of each is important in combustion scenarios. The default value of the Prandtl number Pr_t is 0.7, although this is an input property that can be set by the user. It is assumed that nitrogen is the dominant species in any combustion scenario considered here, thus the diffusion coefficient in the species mass conservation equations is that of the given species diffusing into nitrogen.

A more detailed description of all the models can be found in the FDS Technical Reference Guide.

4. Experimental Studies

4.1. Fire in a Small Scale Compartment

The first part of the simulations deals with a configuration proposed by Suard (Suard et al, 2015; Koched et al, 2014; Koched et al, 2013). Investigation of physical quantities was made by comparison of numerical data to the corresponding experimental values. The experimental measurements were obtained through various mechanisms explained in this section, and can be found in the literature. The data used in this study were obtained from the work of Suard et al (2015). Graphs showing the profiles of doorway/room temperature, the doorway velocity's component V and the three velocity components' profiles at different heights on the doorway are presented later in this study.

4.1.1. Experimental Configuration

The experimental facility was composed of an intermediate scale enclosure, a gas burner, the stereoscopic particle image velocimetry (SPIV) acquisition system and thermocouples. The dimensions of this enclosure were 1.3m×1m×0.8m (L×W×H) with doorway dimensions of H×W=0.65m×0.26m. It was assembled with Monalite-M1 plates (i.e. calcium silicate) with a density of ρ=970kg/m^3 , conductivity of λ=0.26W/m/K (at 600^{o}C) and specific heat of c_p=1100 J/kg/K. Outside the enclosure a 70cm wide stair step was added, protruding 46cm outside the front wall. A system of glass panels with a thickness of 10 mm was placed at the jamb of the doorway whereby a laser sheet illuminated the doorway plane for the SPIV measurements. The glass panels extended 10mm from the outside wall as presented in Figure 4.1.

The thickness of the floor and the ceiling plates was 50mm and 38mm for the walls. The plates were fixed together using silicone seal and the whole enclosure was mounted on a metal chassis located 30cm above the ground. All length measurements were made with a tolerance of ±1mm.

Two modes of ventilation were considered, with four flow rates for the two ventilation modes, none of which are taken into account in the present study: blowing mode and extraction mode. The natural convection scenario results are used instead.

The maximum of the temperature inside the enclosure was 316°C for HRR= 21.7kW. The inflow (fresh air flow) rate was determined properly from the measured inflow velocity fields. **T**he theoretical mass flow rates were calculated by integrating equation **(2.7)** using the experimental temperature profiles from both sides of the opening. The vertical temperature profiles inside the enclosure were obtained by averaging the profiles obtained with trees of thermocouples placed inside the enclosure. The temperature outside the enclosure, far from the doorway, was assumed constant and equal to ambient temperature (i.e. $T_\infty = 25^o C$).

The calculated effective mass flow rates of the inflow of fresh air for the given HRR were: **0.0491kg/s** for the 21.7kW and **0.0416kg/s** for the 15.5kW fire power level(Koched et al, 2014)

4.1.2. Fire Source

The gas burner was supplied with a mixture composed 65% of pure propane and 35% of ethylene providing an effective heat of combustion of about ΔH_c=46.25MJ/kg. The burner was filled with sand

to better diffuse the gas to the top surface of the burner and its final dimensions were 200m×200m with a height of 10cm placed in the center of the compartment.

Several fire scenarios corresponding to different heat release rates (HRR) (e.g. of 7.8, 10.6, 15.5 and 21.7kW) were performed, two of which are in the center of attention of the present study. The cases examined here involve two different fire strengths equal to 15.5kW and 21.7kW. The square burner is located in the center of the room.

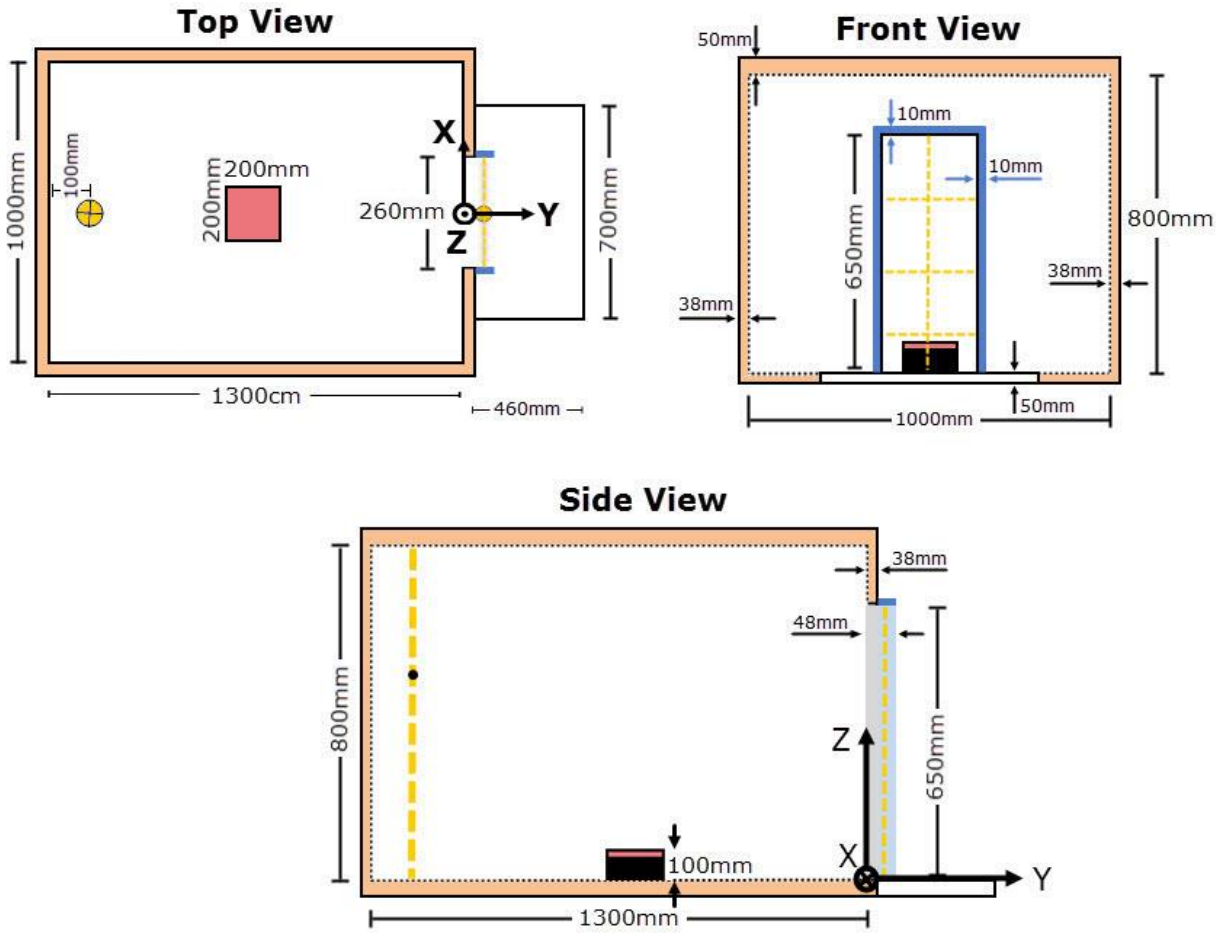

Figure 4.1: Schematic illustration of the enclosure fire experiment

4.1.3. Sensors and Data Acquisition

Velocity measurements at the open doorway were performed using a stereoscopic particle image velocimetry (SPIV) technique, allowing a full comparison with computational fluid dynamics (CFD) results, based on the measurement of the displacement of illuminated tracer particles. Nebulized silicon oil, with an average particle diameter between approximately 5μm and 10μm was used to seed the inflow fresh air, while soot particles produced by combustion were considered as natural seeding for the hot outflow gases in the hot upper layer at the doorway.

The SPIV acquisition system is composed of a pulsed Nd-YAG laser with a 200 mJ/pulse at 532 nm and two 12-bit CCD sensors double frame video cameras with a resolution of 11 million pixels (4008×2672

pixels^2). They were equipped with 50 mm focal length lenses and placed in front of the doorway. Band-pass filters were fixed on the lenses to block wavelengths beyond 532nm±10nm. The cameras were fixed in front of the measurement plane and calibrated towards the same direction using a two-tier calibration plate. An angle of 50° was used to separate the two optical axes of the cameras. Each of them was fixed on a Sheimpflug mount to correct the orientation of the plane of focus relative to the image plane. The measurements were realized at the doorway plane by illuminating with the laser sheet, perpendicular to the flow moving through the doorway.

The velocities were determined through the evaluation of the displacement of tracer particles in the plane of measurement and in the depth of the laser sheet (i.e. ~2mm), according to the principle of the SPIV method. The measurement field size was calculated by the intersection of the respective measurement fields from each camera. The full size of the resulting measurement field was 762mm×482mm. The total field of view captured by the camera was processed using a cross-correlation algorithm, based on the comparison of the intensity variation inside a square spots of 32×32 pixels^2, between frames of a same pair of images captured instantaneously by the cameras. Thus, the finest spatial resolution obtained was 5mm×5mm for these experiments. The acquisition frequency was fixed to 2Hz (i.e. two instantaneous velocity fields measured per second) which is the maximum recording frequency of the cameras. To perform the SPIV measurements at the doorway plane, it is necessary to illuminate it with a laser sheet. To this, the system of glass panels at the jamb of the doorway was employed.

Temperature measurements were made locally inside the enclosure and at the doorway using K-type thermocouples with a diameter of 0.25mm. Trees of tinfoil protected thermocouples were placed inside the enclosure at 10 cm from the walls.

4.1.4. Indicative Experimental Data

The recorded real-time temperature signals on each thermocouple showed a quasi-steady state reached after 15 min of the heating process. To take into account the test repeatability, all fire scenarios have been conducted five times and experimental temperature measurements were averaged over all the tests. The vertical temperature profiles were obtained by time averaging the measured temperature signals on the quasi-steady state. From these values, an estimate of the error bars were calculated from the standard deviation of the repeatability tests which include therefore both measurement uncertainties and physical fluctuation due to repetition of the tests. The SPIV velocity measurements were performed once the quasi-steady state was achieved and for time duration of 400s, corresponding to 800 instantaneous velocity fields which is the minimum required to reach the statistical convergence of the mean velocity components at different positions in the flow.

Temperature profiles at the center of the doorway are presented in Figure 4.2. The experimental measurements exhibit two distinct zones: a first one, from the floor to the mid-height of the doorway, which is a constant temperature zone, and a second one, from the mid-height to the top of the doorway, which is a nearly constant temperature gradient zone.

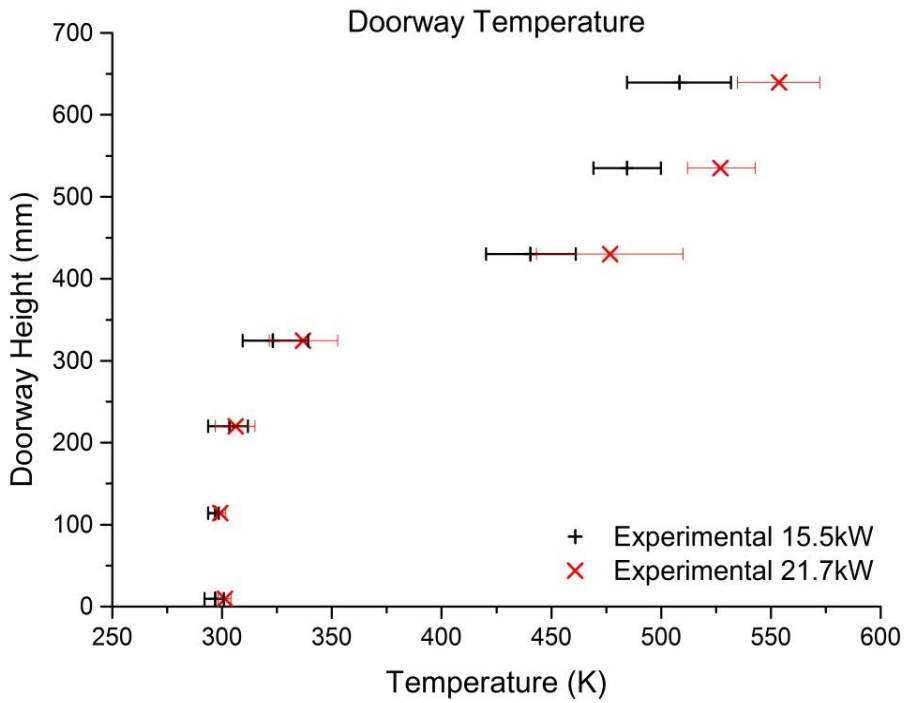

Figure 4.2: Temperature profile on the doorway of the enclosure (Suard et al, 2015)

Comparisons of the measured values of the gas temperature inside the enclosure are shown in Figure 4.3. A series of tinfoil protected thermocouples was placed inside the enclosure at 10cm from the back wall, in the center of the room.

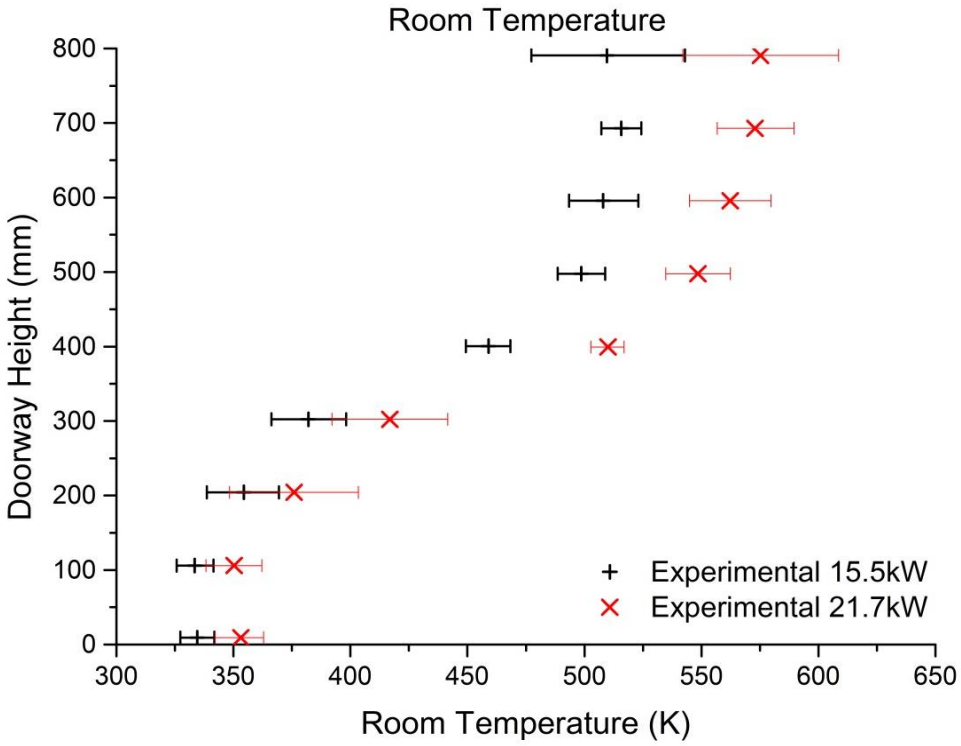

Figure 4.3: Temperature profile inside the enclosure (Suard et al, 2015)

Experimental results of the horizontal velocity component (V), in a vertical plane through the center of the doorway, are given in Figure 4.4, for the two heat release rates. The SPIV measurement method does not allow a full description of the flow at the doorway due to technical limitations for controlling the density of tracers (i.e. soot) and opacity of the spilling plume. Consequently, it is not possible to measure velocities above z/H=0.8, H being the doorway height.

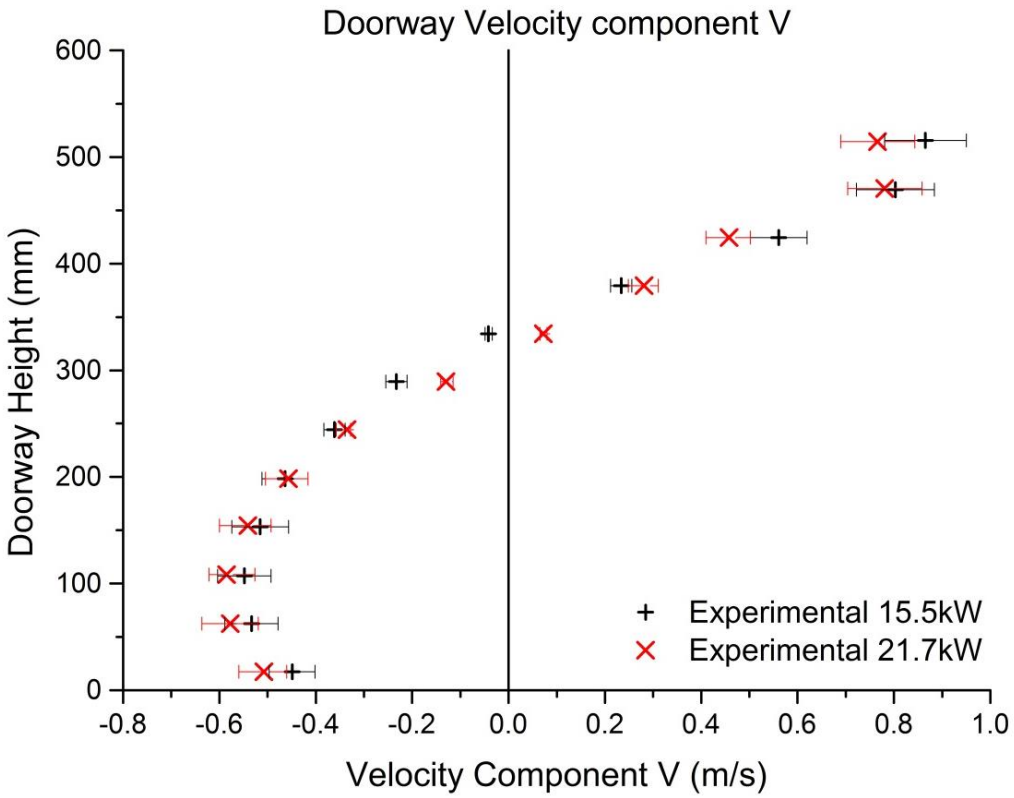

Figure 4.4: Velocity component V profile on the doorway of the enclosure (Suard et al, 2015)

It must be noted that the flow at the doorway may not be totally symmetric regarding the central axis of the doorway. In that case the maximum of velocity can be slightly shifted regarding the axis of the doorway. This can be confirmed by the analysis of the lateral velocity components profiles at the top of the doorway Figure 4.5.

Horizontal profiles across the doorway of the velocity components U, V and W are reported in Figure 4.5 for both heat release rates. The profiles of the y-component (V) of the velocity field have been measured at height z=0.15H, 0.45H and 0.75H, whereas profiles of the x-component (U) and z-component (W) of the velocity are only compared at height z=0.15H and 0.75H for improved legibility.

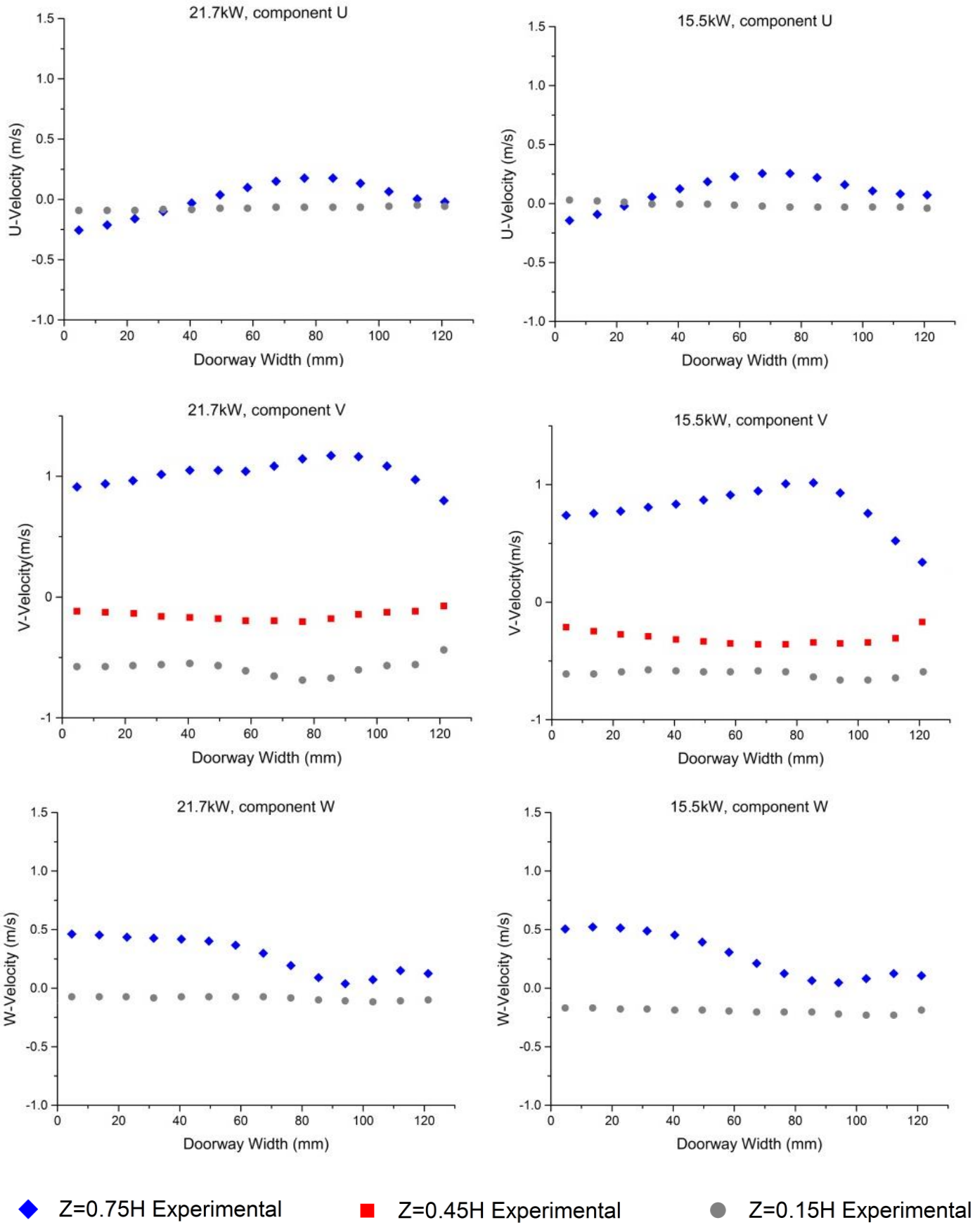

Figure 4.5: Horizontal profiles of the velocity components U, V and W across the doorway at height z=0.15H, z=0.45H and z=0.75H at a fire power of 21.7kW (left) and 15.5kW (right) (Suard et al, 2015)

The calculation of the mass flow rate is performed by discretizing the experimental vertical profile of temperature over a hundred of points in order to determine accurately the neutral plan Z_N and the integration term by a summation of a large number of contributions. The experimental mass flow rate is finally determined by integration of the velocity field measured by the SPIV technique weighted by the gas density.

Since the given mass flow rate values cover only the inflow of fresh air for the given levels of fire HRR, it is necessary that the same process is repeated for the mass flow rate out of the room. In order to achieve that, the height over and under the given neutral plane was discretized over four parts covering the whole doorway area, respectively. Using the temperature and velocity values reported by Suard et al (2015) it was possible to calculate the air density and the resulting mass flow rate of each area. The height of the neutral plane was determined by fitting a linear equation between the single two (for each HRR case) succeeding values of the experimentally measured velocity, the multiplication of which resulted in a negative value. The change of the values' sign expresses the sharp change of velocity's direction depicting a wider area of the neutral plane's location. The obtained results are displayed in Table 4.1 followed by the average temperatures calculated for each experiment.

After summing the four values concerning the mass inflow rate for both 21.7kW and 15.5kW cases, the resulting error of the procedure in comparison to the experimental values was **-1.80%** for the 21.7kW case and **-0.36%** for the 15.5kW case. Since both values stand lower than 2% it is considered safe to say that this method is proved to be secure. The resulting average temperature of the inflow area is 309.3K and 305.5K for each case respectively.

In the same manner the mass outflow rate can be calculated, expecting a tolerable deviation from the experimental values. After repeating the process over the higher area of the doorway for both cases, the mass outflow rates appear to be 0.04959kg/s for the 21.7kW case and 0.05393kg/s for the 15.5kW case. The corresponding average temperature values are 482.2K and 447.5K.

Table 4.1: Mass flow rate analytical estimation for the two heat release rates.

HRR	Mass Inflow Rate (kg/s)	Error	Average Inflow Temperature (K)	Mass Outflow Rate (kg/s)	Average Outflow Temperature (K)	Neutral Plane Height (m)
21.7kW	0.0499	-1.08%	309	0.0496	482	0.318
15.5kW	0.0418	-0.36%	306	0.0539	447	0.341

4.2. Fire in a Large Scale Compartment

The second part of the simulations focuses on the configuration proposed by Bryant (Bryant, 2011; Bryant, 2009a; Bryant, 2009b). As with the small scale compartment, comparison of data obtained from the simulations with the corresponding experimental values aid the investigation of certain physical quantities. The experimental measurements were obtained through various mechanisms explained in this section, and can be found in the literature. Graphs showing the profiles of the doorway temperature (Bryant, 2011), the doorway velocity (Bryant, 2009a) and the velocity components' profiles at different heights on the doorway (Bryant, 2009b) are presented later in this section.

4.2.1. Experimental Configuration

The fire experiments were performed using the ISO9705 room, 0.29 ± 0.01m above the laboratory floor. This is a full-scale room used to evaluate wall surface products for their contribution to fire growth. Fabrication of the room followed the specifications stated in the standard. The interior dimensions of the room were determined to be 3.60m×2.40m×2.40m (L×W×H). The interior walls of the enclosure were lined with both drywall/gypsum (lower half of the vertical walls and the floor) and calcium silicate panels (upper half of the vertical walls and the ceiling). Both materials were applied as two sheets and the resulting wall thickness was 2.5cm. The estimated standard uncertainty of the interior dimensions is ±0.04m.

A doorway served as the only vent for the enclosure. It was located on the center of one of the 2.40m×2.40m walls, and had internal dimensions of 0.79m×1.96m (W×H). The depth of the doorway was larger than usual due to the requirement of a window mounted on one side of the doorway to pass the laser sheet across the doorway for additional PIV measurements. The depth of the doorway or jamb depth, D, was 0.30m, similar to that of a standard interior doorway, resulting in a door jamb that extended beyond the exterior framework of the enclosure. The estimated standard uncertainty of the doorway dimensions is ±0.01m. A schematic of the setup is shown in Figure 4.6. In this configuration, the limits of integration for a direct computation of volume flow rate are defined by the intersection of the laser sheet and the solid boundaries of the door frame.

4.2.2. Fire Source

Natural gas fires were generated from a square burner (0.31m×0.31m) placed in the center of the enclosure. The top of the burner stood 0.30 m above the enclosure floor. The natural gas flow was held constant during the experiments and measured to compute the ideal heat release rate. Resulting heat release rates ranged from 34 kW to 511 kW with a relative expanded uncertainty of ±0.02%. This range of fires simulated the developing stage of a fire for the dimensions of the enclosure and the opening.

A complete experiment started with achieving quasi-steady- state conditions inside the room for the minimum fire size, acquiring measurements, increasing the natural gas flow to reach the next fire size, and repeating the process until the final fire size was attained. Six experiments were conducted to repeat the conditions of the enclosure fire with the exception of the maximum fire size, 511kW, for which only two repeat experiments were conducted, one for each technique.

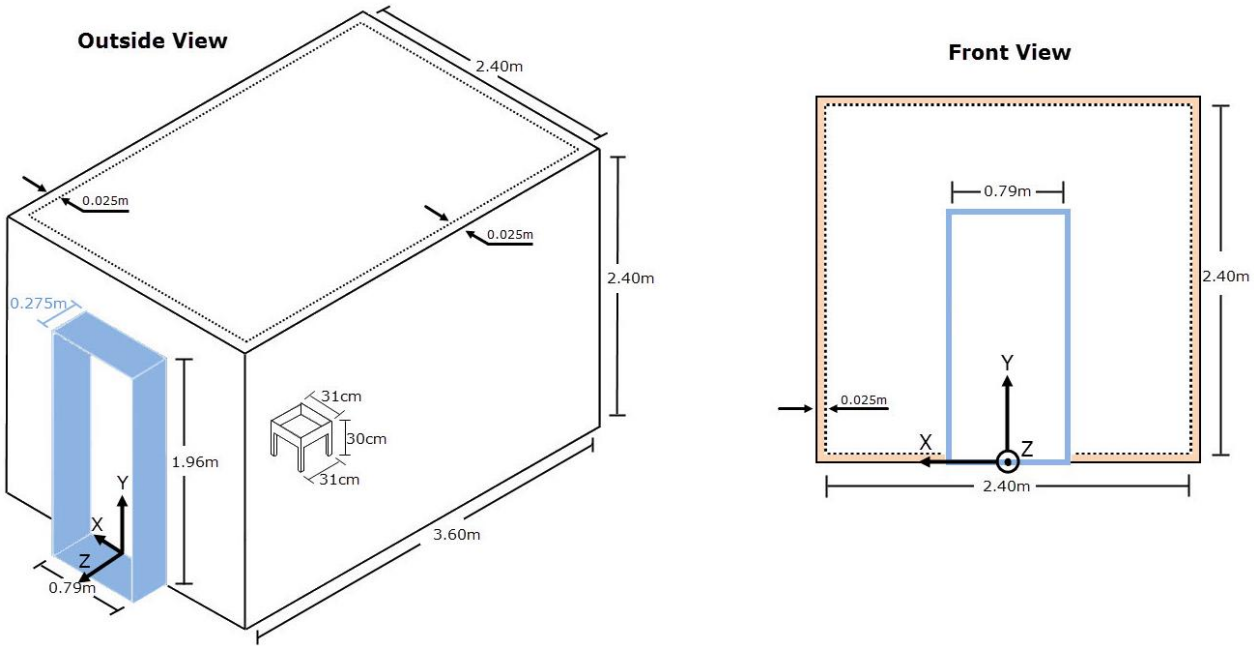

Figure 4.6: Schematic illustration of the enclosure fire experiment and the CFD devices' position

4.2.3. Sensors and Data Acquisition

SPIV measurements were conducted at each set point after quasi steady-state conditions inside the enclosure were achieved, that is after the effect of the initial transient had abated. The condition of quasi-steady-state inside the enclosure was determined by monitoring a thermocouple for relatively constant temperature. The thermocouple was located in the upper corner of the room.

Measurements of differential pressure through the doorway were acquired with a vertical array of 14 bi-directional probes placed on the centerline of the doorway. Each probe had a dedicated differential capacitance manometer; each with a measurement range of 0-133 Pa and relative standard uncertainty of ±0.0007. The vertical spacing between each probe was 14cm, with the exception of a spacing of 12.5cm between the topmost probe and its adjacent probe.

Temperature measurements from bare-bead thermocouples were used to estimate the vertical profile of gas temperature in the doorway. The thermocouples were Type K and were placed adjacent to each bi-directional probe to provide an estimate of the local gas temperature. Thermocouples located at elevations of 1.4m and below were constructed with 0.255mm diameter wire (30 gauge) and had an average bead diameter of 0.6mm ±0.1mm. Thermocouples located above an elevation of 1.4m (the 4 topmost thermocouples) were anticipated to be exposed to the high temperature gas flowing out of the room and were constructed of 0.511mm diameter wire (24 gauge). The average bead diameter for these thermocouples was 1.0mm ±0.1mm.

Measured thermocouple temperatures were not corrected for radiation but were applied directly as estimates of gas temperature. For the flow into the room, the measured temperatures were typically less than 306K. The exception was the case of the largest fire, 511kW, where the maximum temperature below the flow interface was 324K. The air flowing into the room should be at the same temperature as the ambient air, so the difference in the thermocouple temperature and the temperature of the local ambient air is the most conservative estimate of the uncertainty of the gas temperature for the flow into the room. This standard relative uncertainty was typically below ±0.03,

with the exception of the largest fire where it ranged from ±0.04 to ±0.09. The thermocouples above the flow interface were exposed to the hot gases flowing out of the room. Again the measurements estimate the gas temperature and the difference in the measurement and the gas temperature is applied as the uncertainty of the gas temperature measurement.

Stereoscopic PIV was applied to measure the velocity field due to the air flowing into the ISO room. The SPIV system consisted of a double pulsed Nd:YAG laser, two double-framed CCD cameras, and a desktop computer for image acquisition, time synchronization, and vector processing. The laser delivered two beams with average pulse energy of 200mJ/pulse at 532nm. A sheet forming optics assembly expanded the beams to a height of approximately 1.8m at the doorway and a sheet thickness of approximately 1.2cm. Positioning of the laser sheet at the doorway was performed by a 90° mirror attached to a translation stage. The double-framed CCD cameras had sensors of 2048×2048 pixels with pixel dimensions of 7.4µm on a side. Image frame rates achieved during the experiments were on the order of 1 frame per second due to the data transfer limits of the desktop computer. Wide angle 20mm focal length lenses were used in order to keep the cameras close to the doorway and capture as much of the doorway as possible in the images. Since the physical probe measurements and the SPIV measurements could not occur simultaneously at the same locations, the bi-directional probes had to be removed during the SPIV measurements.

The seed particles were gas filled hollow plastic spheres, commonly referred to as microspheres. The particles had a weight averaged diameter ranging from 100 to 140µm and a density of 30 kg/m^3. A paint sprayer was used to inject a fine cloud of seed particles into the area outside of the ISO room.

The bi-directional probe and thermocouple measurements were conducted with a simple vertical array located in the geometric center of the doorway. Stereoscopic PIV measurements were conducted on a vertical plane intersecting the line of probes at the center of the doorway. The laser sheet propagated through the doorway into the ISO room and was perpendicular to the front wall of the ISO room. In this configuration, the bulk flow of the fluid was parallel to the plane of the laser sheet; therefore, the evolution of the flow as it moved from outside the doorway to inside the room was characterized. There is a linear relationship between the results of the three techniques. SPIV provides the most comprehensive measurement of the gas velocity field in the doorway of the three techniques applied. The other estimates rely on the simplifying assumptions that the flow is invariant in the horizontal direction and that the flow speed estimates the normal velocity component.

Quasi-steady-state was defined by a relatively constant temperature reading from an aspirated thermocouple located in the upper layer inside the room. Upon reaching this steady-state, tracer particles were injected into the flow and SPIV measurements were taken. At least 200 SPIV measurements were recorded at a rate of 1 Hz for each fire size. Temperature and differential pressure measurements at the bi-directional probe array were performed continuously, and the readings were recorded at a rate of 1 Hz.

4.2.4 Indicative Experimental Data

The SPIV measurements provide a complete mapping of the velocity field, the velocity component normal to the doorway cross section, and an accurate determination of the cross sectional area for the flow into the room. Coupled with an almost constant air temperature flowing into the room, SPIV meets all of the requirements to provide the best estimate of mass flow rate of air into the enclosure.

In the range of 160-511kW there is a slower rate of increase in air mass flow rate than in the other cases that were examined (34-160kW).

Vertical profiles of gas velocity and gas density in the doorway were computed using measurements from the vertical array of bi-directional probes and bare bead thermocouples located on the doorway centerline. The bi-directional probes integrate the local gas pressure over the space of their openings. The openings are large to reduce clogging and sensitivity to flow angle, therefore the measurement is more representative of the flow speed. Negative flow speed represents air flowing into the enclosure while the flow above the interface is positive and flows out of the enclosure.

The SPIV results demonstrated that the velocity field was not invariant in the horizontal direction. However, it has long been practical to assume a vertically distributed flow only. Once again, the gas density distribution in the doorway was computed from the doorway temperature distribution for the 160kW case, Figure 4.7.

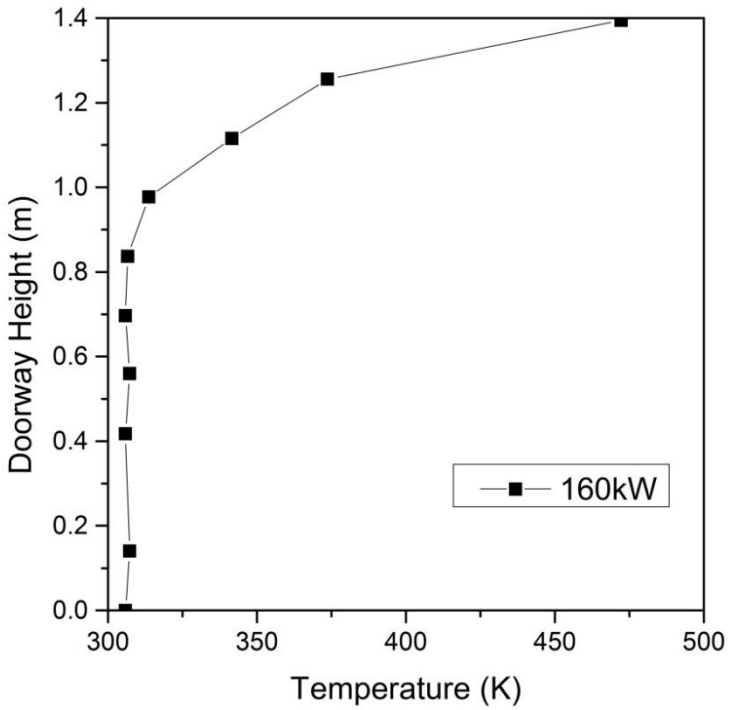

Figure 4.7: Temperature profile on the doorway of the compartment (Bryant, 2011)

The difference in gas density between the enclosure and the space outside the enclosure induces a static pressure difference across the doorway. This static pressure distribution can be computed from measurements of the vertical temperature distribution inside and outside the enclosure. Uncertainty estimates (expanded) for the temperature measurements inside the enclosure and outside the enclosure were ±20K and ±2K, respectively. The vertical velocity distribution was computed from the static pressure distribution by applying Bernoulli's equation along horizontal streamlines, assuming the flow started from rest far from the doorway. The temperature measurements in the doorway were once again used to compute the gas density distribution in the doorway, while the flow interface height that was determined from the bi-directional probe measurements was used for the vertical integration limit.

Horizontal profiles of the velocity components are plotted in Figure 4.8 for selected elevations. Profiles measured for the conditions of the 160 kW fire are displayed and are representative of the general characteristics of the profiles. The profiles demonstrate the significant variation in each component of velocity with respect to position in the doorway. The profiles also demonstrate that the flow is nearly symmetric about the vertical axis. For the $\mathbf{V_X}$ profiles the symmetric features for the flow into the room are opposite to those features for the flow out of the room. The measurement plane is closer to the room exterior therefore capturing the flow convergence from the ambient toward the doorway and the flow divergence from inside the room to the ambient.

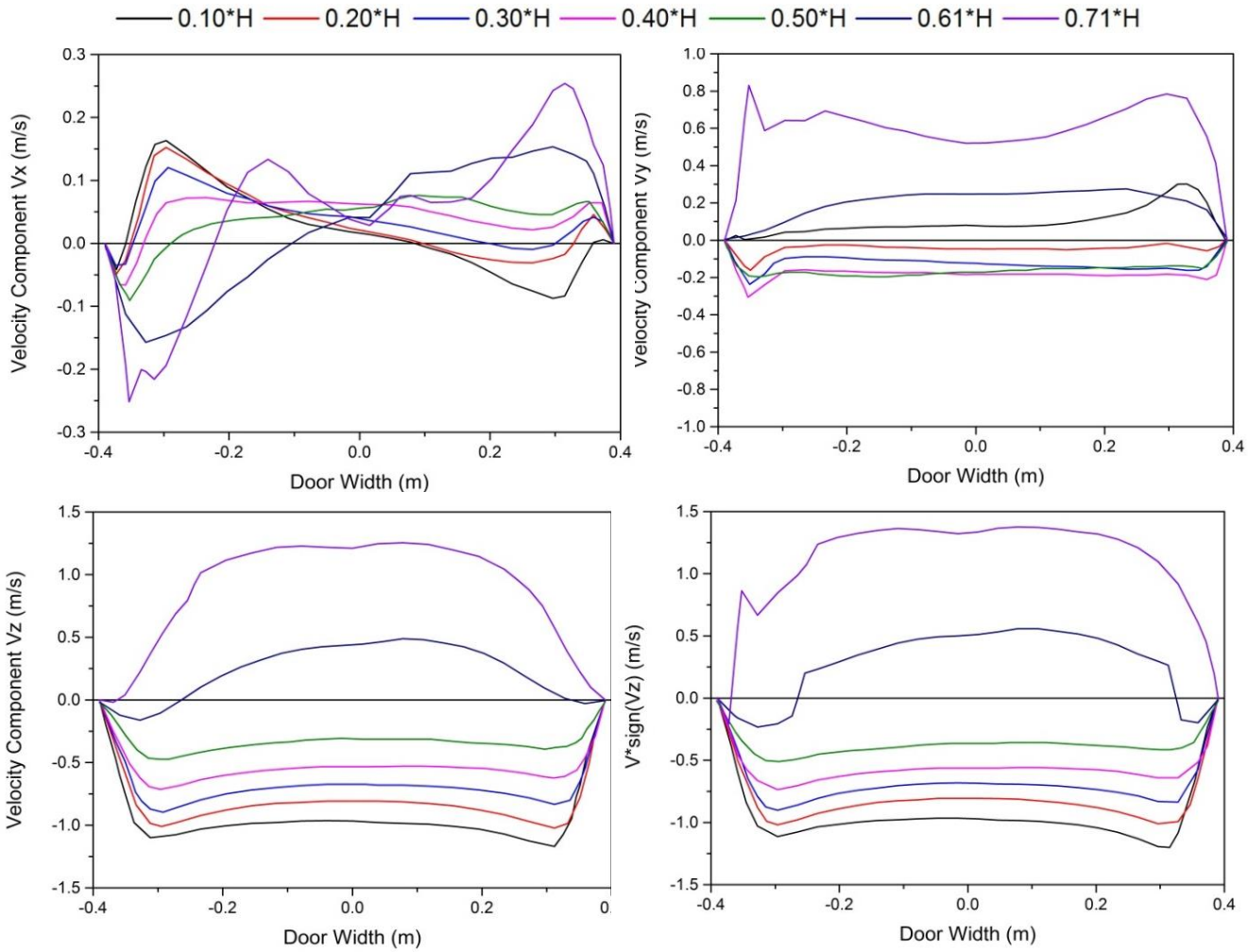

Figure 4.8: Horizontal profiles of velocity components and velocity magnitude for the 160 kW fire. Sign(V_Z)=1 when V_Z>0 and Sign(V_Z)=-1 when V_Z<0.

The $\mathbf{V_Y}$ component of velocity is positive for the flow out of the room due to the buoyancy of the plume issuing from the doorway. Negative $\mathbf{V_Y}$ is observed for the flow into the room except near the bottom of the doorway. The room stands above the laboratory floor and the flow must step up into the room. Much of the upward momentum of the flow remains at this measurement location.

For the flow into the room, negative $\mathbf{V_z}$, the magnitude of $\mathbf{V_z}$ is the greatest near the solid boundaries of the doorway and goes through a minimum near the centerline. These profiles are characteristic of the flow across an orifice that originated as an ideal flow at rest. The profiles for velocity magnitude are almost identical to $\mathbf{V_z}$ profiles for the flow into the room, where $\mathbf{V_z}$ dominates the contribution to the velocity magnitude. However, the profiles are flatter for the flow out of the room due to a significant contribution from the $\mathbf{V_Y}$ component.

The available data for the vertical profiles of the velocity measurements from the bi-directional probes and SPIV, at x=0.0 and z= 0.0, are plotted in Figure 4.9. Profiles for two of the seven fire sizes are shown for clarity. The velocity results for the bi-directional probe measurements were computed assuming the molecular weight of the gas to be equal to that of air. It is estimated that the relative discrepancy between the molecular weight of the gas flowing out of the room and the molecular weight of air will be less than 0.01.

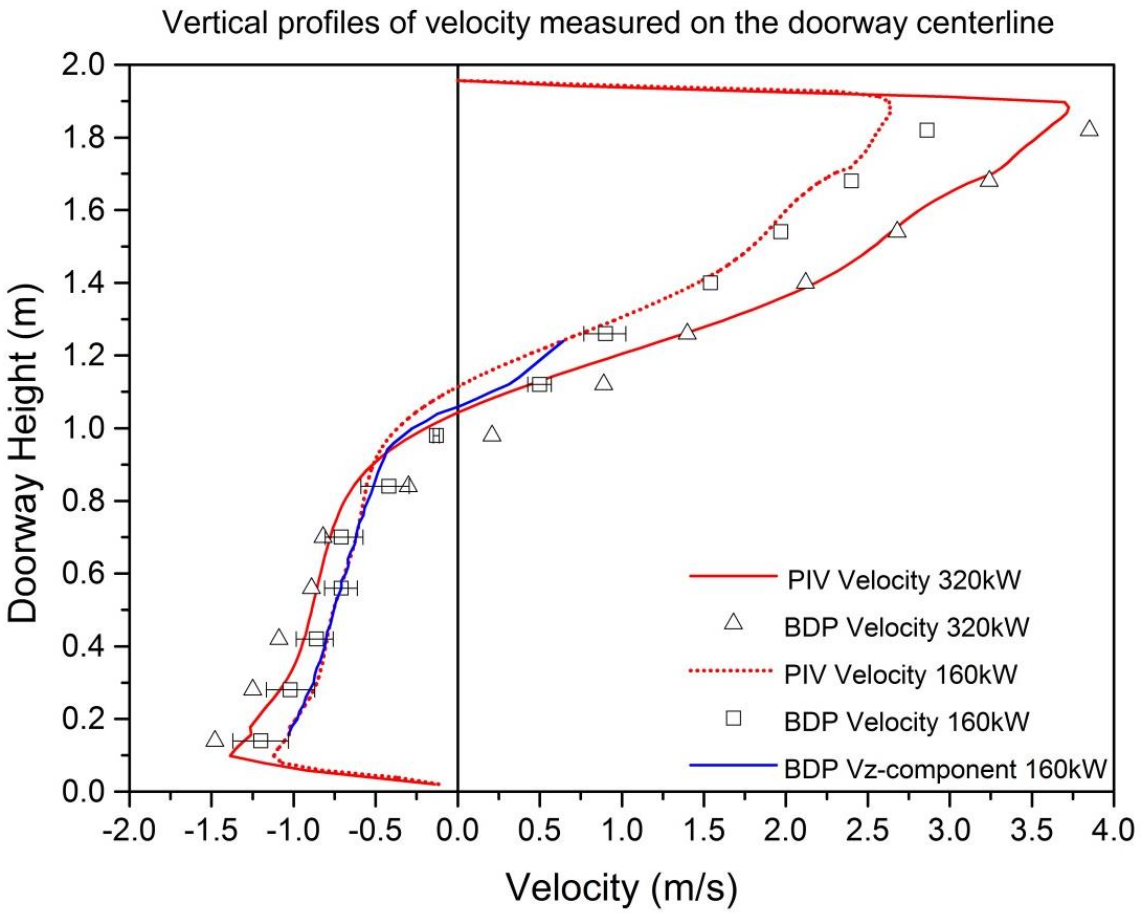

Figure 4.9: Mean velocity profile on the doorway of the enclosure

Error bars in Figure 4.9 represent the estimated expanded (coverage factor of 2 for an estimated 95% confidence interval) uncertainty of the gas velocity measurement using the bi directional probe and using SPIV. The relative expanded uncertainty of the bi-directional probe measurements ranged from 70.14 to 70.22. The uncertainty of the bi-directional probe measurements is much larger than the SPIV measurements due to the large relative standard uncertainty in the empirical probe constant, C, estimated at 70.07 for the study. When the fire size increases above 320kW the uncertainty due to the gas temperature measurement also begins to contribute more to the combined uncertainty. Figure 4.9 shows that there is a discrepancy between the velocities measured with the two techniques.

However the error bars for the bi-directional probe measurements are larger than the discrepancy for most of the measurements below the flow interface. This suggests good agreement within the bounds of uncertainty between the two techniques but the discrepancy deserves further study because within a specific region of the flow a consistent trend was observed for the different fire conditions.

The discrepancy between $\mathbf{V_z}$ and **V** profiles of Figure 4.9 demonstrate that the flow through the door way is not entirely horizontal, especially in the flow out of the room where the discrepancy between $\mathbf{V_z}$ and flow speed is the greatest. Near the flow interface, where $\mathbf{V_z}$ and **V** approach zero, the discrepancy between the bi-directional probe and SPIV results was large. In this region the probe results were consistently lower than the SPIV results.

The experimental mass flow rate can finally be determined by integrating the velocity field measured by the SPIV technique weighted by the gas density, with the equation **(2.7)**. In order to achieve that, the height over the given neutral plane was discretized over seven parts covering the whole area of the outflow. The same procedure was repeated for the area occupied by the inflow respectively. Using the temperature (Bryant, 2011) and velocity (Bryant, 2009a) values reported by Bryant it was possible to calculate the air density and the resulting mass flow rate of each area. Again, the height of the neutral plane was determined by fitting a linear equation between the single two (for each HRR case) succeeding values of the experimentally measured velocity, the multiplication of which resulted in a negative value. After summing the seven values concerning the mass flow rate for the 160kW and 320kW cases, the final values are used to evaluate the data of the CFD study that follows.

The mass flow rate is again calculated expecting a tolerable deviation from the experimental values since the same technique was used in the Small Scale Compartment section of this study. After repeating the process over the higher and lower area for the two cases, the mass outflow rates and average zone temperatures appear to be as shown in **Table 4.2**.

Table 4.2: Mass flow rate analytical estimation for the two heat release rates. The height of the neutral plane is shown for each experiment.

HRR	Mass Inflow Rate (kg/s)	Average Inflow Temperature (K)	Mass Outflow Rate (kg/s)	Average Outflow Temperature (K)	Neutral Plane Height (m)
160kW	0.703	307	0.835	472	1.009
320 kW	0.817	311	0.962	576	0.922

It is necessary to note the temperature data used for the integration of the mass inflow rate has been averaged over the entire zone below the neutral plane, for both cases. For the zone above the neutral plane, the provided temperature data covered up to 1.4m of the total 1.96m of the doorway height. For that reason the maximum temperature value (corresponding to 1.4m of the doorway height) was employed as an estimation of the average outflow zone temperature.

5. Computational Simulation of Fire in a Small Scale Compartment

The simulation of the small scale compartment was made in FDS using the last available version to that date, 6.3.2. Several changes and modifications were made in the input parameters during the assemble of the final input files, the most vital of which will be described below. The simulations that follow are based on the experiments initially made by Koched et al (2014) and Suard et al (2015). The data acquisition was made possible by utilizing the sensors' position and other configuration characteristics as described by Suard et al (2015).

The geometry had to follow both the guidelines of the given literature and the restrictions of the code resulting in three different mesh resolutions, which will be presented later in the parametric study. The range of many other variables, constants and selection of configurations was examined as well, resulting in the best set of assumptions and decisions needed to limit the discrepancy between computational and experimental results within an acceptable interval.

5.1. Parametric Study

The parametric study that was made contained both alternative computational models and assumptions.

The heat release rate (HRR) is an important factor which if altered, can lead to great variations in the results. This effect is not unexpected since the mechanism of a fire-induced flow through a vent is entirely dependent on the hydrostatic phenomena caused by the fire source. For the case of the small scale compartment, two different values of heat release rates were examined: 15.5kW and 21.7kW.

FDS has several approaches for describing the pyrolysis of solids and liquids all of which require that the user explicitly defines the gas phase reaction. The experiment standards lead to the use of a gas burner with a specified heat release rate which has no need of material properties' specification. This is essentially a burner, with a specified Heat Release Rate per Unit Area, HRRPUA, in units of kW/m^2. In that way, considering the burner to be a square surface of a 20cm side, 15.5kW HRR case corresponds to an HRRPUA value of $15.5/(0.2)^2=387.5$ kW/m^2 and the 21.7kW HRR case to a HRRPUA value of $21.7/(0.2)^2=542.5$ kW/m^2. In terms of the numerical simulation, the soot yield factor was set equal to 0.01 and the CO factor equal to 0.02.

The computational grid resolution is another factor of major significance in the results' precision. It is stated in the FDS User Guide that it is best if the grid cells resemble cubes and that was the first guideline that was followed throughout the whole geometry. The size of the cubes was kept constant on the whole space as well.

The cases that were examined and will be presented in this section are compared to experimental values obtained from the literature. Six different cases were examined for the 21.7kW experiment, and three for the 15.5kW experiment, the names of which reflect the computational cell size and the thermal properties that were assigned on the walls. The names and basic characteristics of each case are presented in Table 5.1.

Table 5.2: Names, mesh cell sizes and walls' thermal properties of the examined cases.

Case Name	HRR simulated (kW)	Mesh Cell Size (mm)	D*/δ	Wall Thermal Boundary Conditions
Coarse_Ad	21.7	50	4.2	Adiabatic
Medium_Ad	21.7	13	15.9	Adiabatic
Fine_Ad	21.7	10	20.7	Adiabatic
Coarse_NoAd	21.7	50	4.2	Conductive
Medium_NoAd	21.7	13	15.9	Conductive
Fine_NoAd	21.7	10	20.7	Conductive
Coarse_NoAd	15.5	50	3.6	Conductive
Medium_NoAd	15.5	13	13.9	Conductive
Fine_NoAd	15.5	10	18.1	Conductive

The size of the meshes' cells that were examined was of 10mm (fine mesh), 13mm (medium mesh) and 50mm (coarse mesh). The effects of the alternatives that were used will be displayed through analytical comparative graphs in another section. It is clear that the cells' size cannot be chosen arbitrarily but rather based on certain criteria. In Table 5.2 the values of the computational grid criteria, presented in section 3.2 are displayed in comparison to their minimum limits. It is easy to see that the two cases using the medium (13mm) and fine (10mm) cell sizes are in a safe zone away from the limits that are suggested in the literature for the given dimensions/fire sizes, while the case using the coarse mesh (50mm) fails to meet any of the criteria shown (values marked in grey).

Table 5.2: Comparison between calculated values of the three criteria and their suggested limits

Source	**Suard et al (2015)**				**Suard et al (2015)**			
HRR	*15.5 kW*				*21.7 kW*			
Cell Size	10mm	13mm	50mm	Limit	10mm	13mm	50mm	Limit
$D^*/\delta x$	**18.1**	**13.9**	**3.6**		**20.7**	**15.9**	**4.2**	
l_1^*	**45**	**34.7**	**9**	≥ 10	**45**	**34.7**	**9**	≥ 10
l_2^*	**37.1**	**28.6**	**7.4**		**37.1**	**28.6**	**7.4**	

The arithmetic difference between the values shown in Table 5.2 and their supposed limits that were provided in the literature does not automatically ensure the accuracy of the computational results. This is an important realization that is made clear after the results are properly handled and put in comparison with the experimental values. This comparison will be presented subsequently.

Another aspect that was examined concerned the wall thermal boundary conditions. The analysis was limited in the application of both conductive and adiabatic boundary conditions on the surfaces of the compartment. The latter resulted in having no heat transfer (radiative and convective) from the gas to the solid surfaces of the room. The result is that FDS computed a wall temperature so that the sum of

the net convective and radiative heat flux is zero. Specifying a surface as ADIABATIC will result in FDS defining NET_HEAT_FLUX=0 and EMISSIVITY=1. Since no solid surface is truly adiabatic, this step was performed in order to witness the effect it would create on the results of the experiment.

5.2. Initial Values and Boundary Conditions

The default ambient temperature of the code (meaning the temperature of everything at the start of the calculation) is 20^{o}C. In the given experiment though, that is not the case. A *MISC* line was added setting the ambient temperature at **25^{o}C** as shown in graphs provided by the literature.

A simple observation of various data value development (through time) shows that the quasi-steady state conditions occur after the first 300 seconds of the simulation time. For that reason a time limit for all further simulations was determined, being 1000 seconds. All data presented in the following sections represent time-averaged quantities of the last 500 seconds of the simulations. That is from the 500 second mark, to the 1000 second mark. Such long simulations require great computational power in order not to be considered as time-wise prohibitive. For that reason a TIME_SHRINK_FACTOR was employed for the "conductive" test cases, equal to 10, dividing the expected simulation time by ten. When this option is used, the specific heats of the various materials are reduced by a factor of 10, speeding up the heating of these materials roughly by 10.

As it is explained in the FDS User Guide, an example of an application where this parameter is handy is a validation experiment where a steady heat source warms up a compartment to a nearly equilibrium state at which point time-averaged flow quantities are measured. It is obvious that this description fits the given experiment perfectly.

The description of the original experiment mentioned the fuel to be a mixture of 65% propane and 35% ethylene. In terms of the simulation that part was simplified by declaring propane to be the only fuel present, preserving the given effective heat of combustion of 46.25MJ/kg. The SOOT_YIELD and CO_YIELD values were declared but with their default values: 0.01 and 0.02 respectively.

5.3. Simulation Details

An attempt was made throughout the whole code building process to remain as close to the original proportions of the geometry as possible. The physical properties of the walls, the floor and the ceiling such as conductivity, specific heat, density and thickness were maintained as described in the literature.

Since all walls are assumed to always back up to the ambient, the attribute BACKING='VOID' was set for all of them with zero thickness. That way a significant number of computational cells of no importance was evaded saving computational time, while enabling the code to solve for the heat transfer through the wall into the space behind the wall. Since the wall is an external boundary of the domain, the heat is obviously lost to an ambient temperature void. The front wall's thickness was set equal from 2 to 4 computational cells depending on their size, reaching a total thickness of ~4cm or 5cm. For the simulations using adiabatic boundary conditions, the wall properties were removed from the input file, thus allowing for a completely different solution procedure.

All sides of the gas burner were set as INERT, except for the upper side which was assumed to be an inlet for the gas.

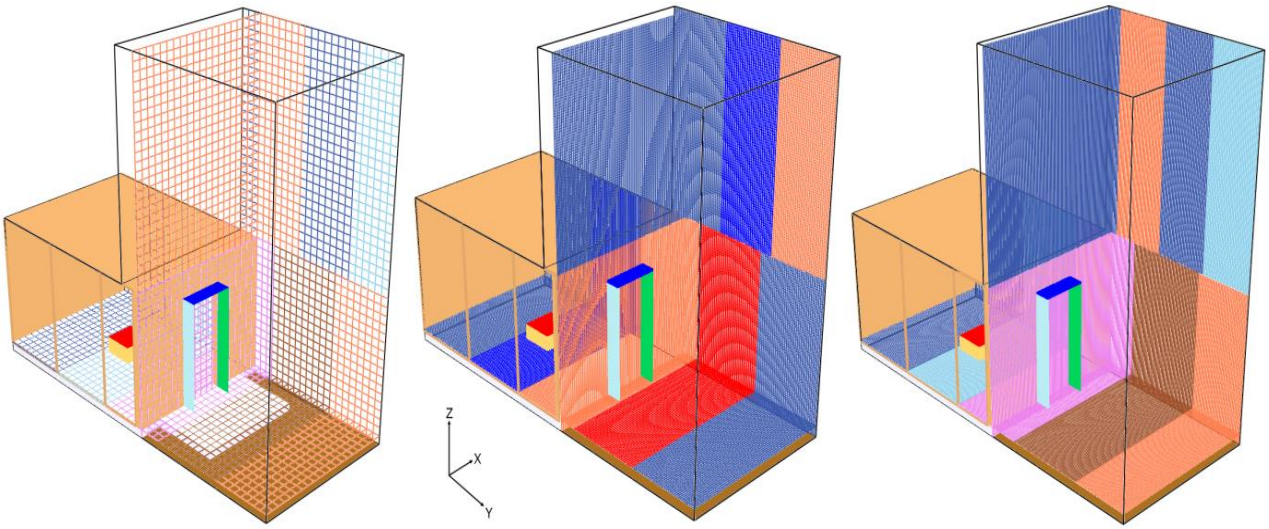

Figure 5.1: Graphic view of the three examined configurations, using 50mm (left), 13mm (middle) and 10mm (right) grid

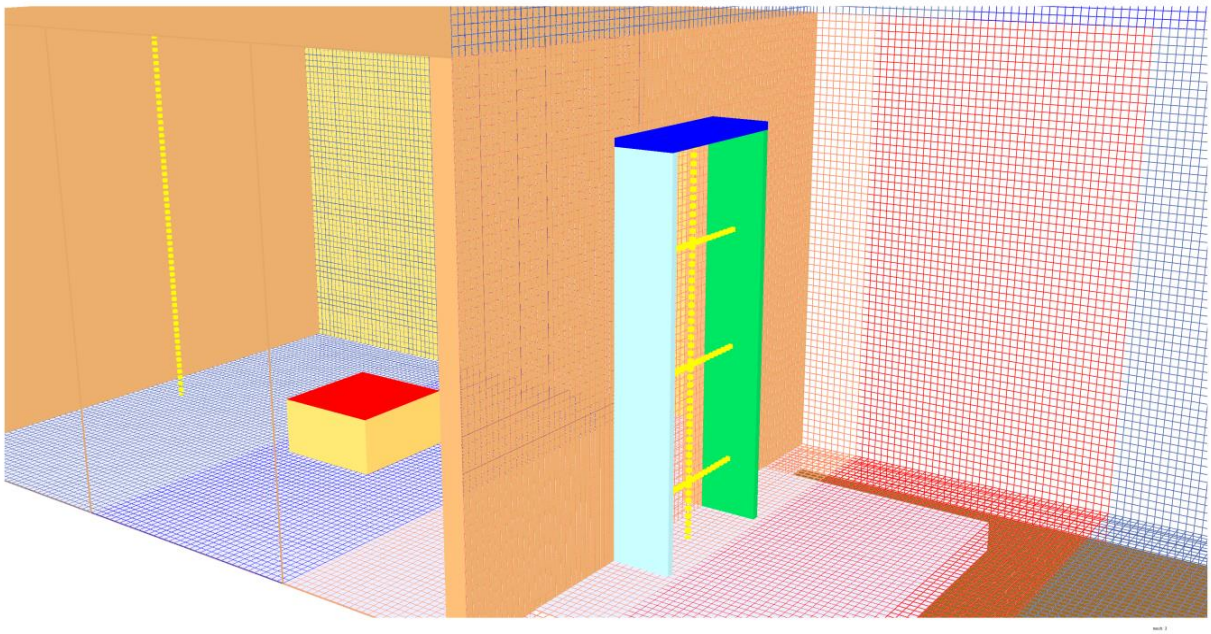

Figure 5.2: Detail of the computation mesh structure

The glass panels used for the SPIV measurements in front of the doorway are poorly described in the literature, since various conflicting dimensions are mentioned. The dimensions that were used in the simulation set the panels to be 10mm/13mm/0mm thick outside the door's bounds, protruding 100mm/103mm/100mm from the outside wall respectively for each cell size case.

The ambient environment was discretized using cells of the same size as for the compartment. The extension of the mesh in the space outside the experimental facility was made following the suggestions provided by the literature (Section 3.3). The final ambient area dimensions extend 1.07m/1.066m/1.1m away from the front wall in the x-axis, 1m/1.014m/1m wide in the y-axis and 2.07m/1.95m/2.05m high in the z-axis respectively for each cell size case. The three configurations described here are presented in Figure 5.1. A detail of the meshing that was used can be seen in Figure 5.2.

It must be noted that the suggested mesh extension (Zhang et al, 2010) in the perpendicular to the vent opening plane (here: x-y plane) is approximately 0.4m.

All the surfaces created by the extension of the mesh in the ambient environment were declared as VENT. In FDS the VENT group is used to prescribe planes adjacent to obstructions or external walls.

5.4. Data Recording

Various slices were defined in the code after constructing the geometry. A "slice" refers to a subset of the whole domain allowing the recording of various gas phase quantities at more than a single point. Gas temperatures are computed at cell centers, but they are linearly interpolated to cell corners and output to a file that is read by *Smokeview*.

The position of the temperature and velocity measuring devices was determined by the existing literature. That is in the back center of the room, 100mm away from the back wall and the center of the glass panels for the doorway devices. Horizontal arrays of devices were also set on three different heights of the doorway, again exactly as dictated by the existing literature.

The vertical arrays of devices consisted of virtual measuring devices placed from Z=0.0mm to Z=0.800m, having 0.013m distance between them. The horizontal arrays were placed at the heights of Z=0.0975m, Z=0.2925m and Z=0.4875m spanning from X=-0.130m to X=0.130m with 0.013m intervals. A graphic presentation of the said measuring arrangements can be seen in Figure 5.3.

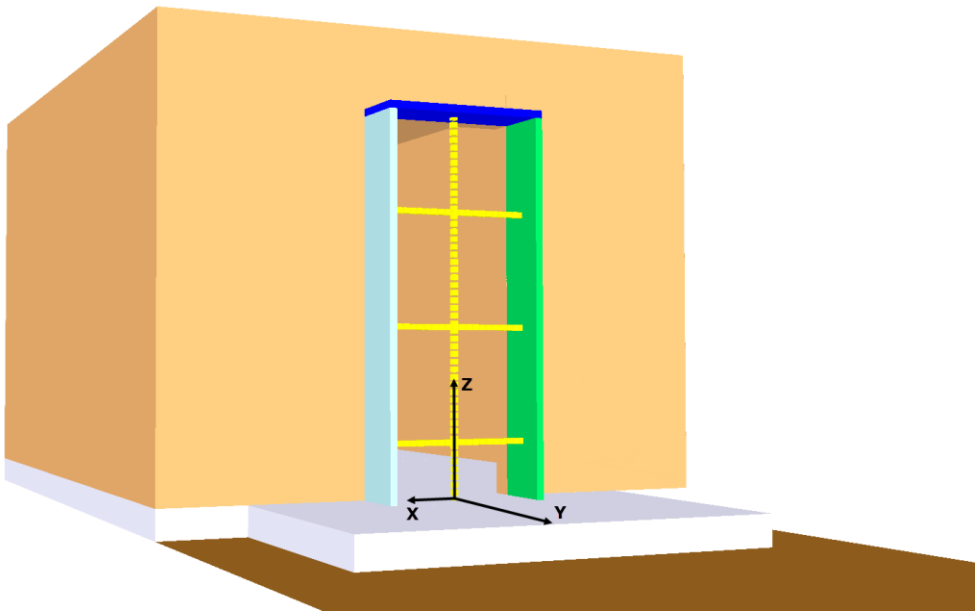

Figure 5.3: Graphic presentation of the doorway's devices' position used in the three configurations

5.5. Validation of Computational Results

5.5.1. Validation of the 21.7kW case

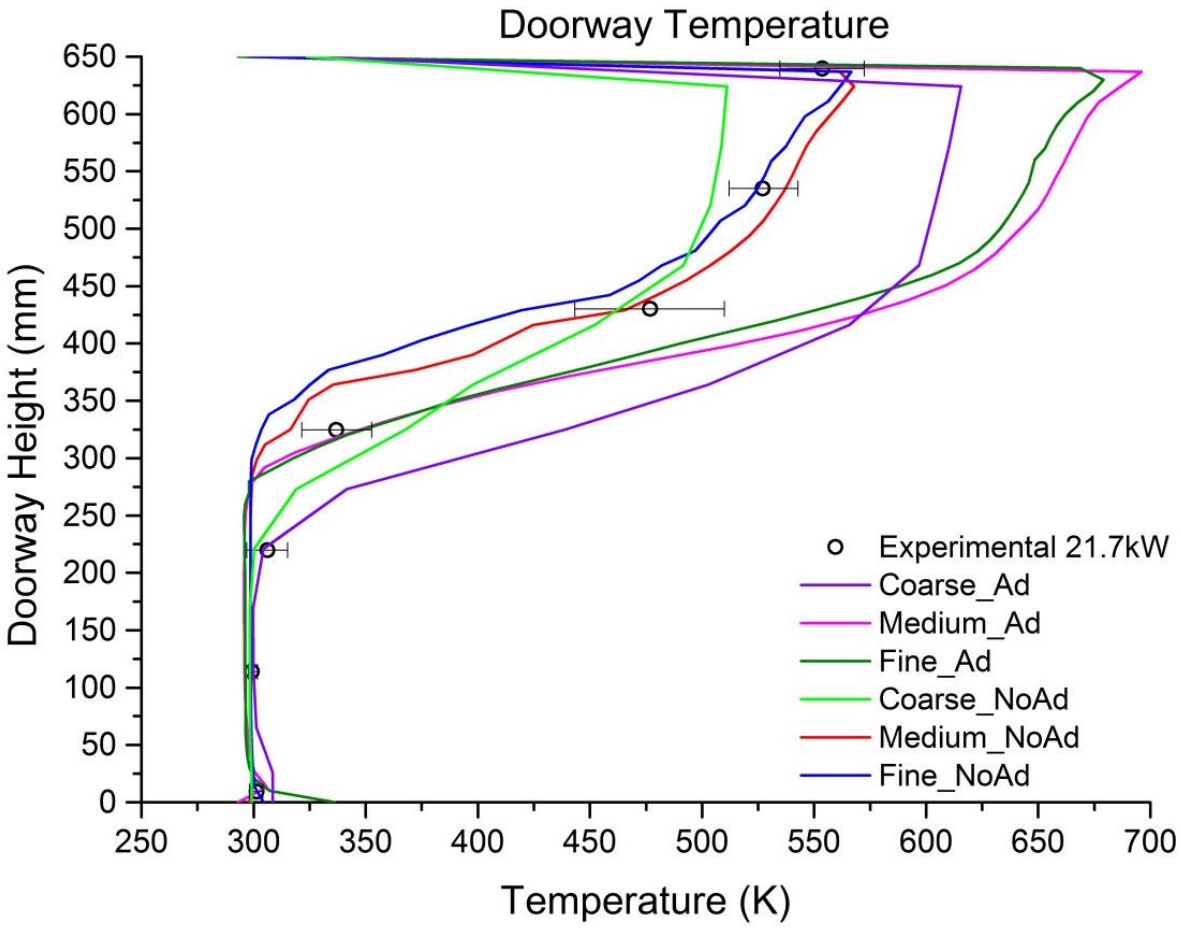

Figure 5.4: Temperature profile at the door of the small scale compartment

As shown in Figure 5.4 the temperature profiles of the adiabatic cases examined show a clear trend to completely miss the experimental values from the very beginning. That is in one way expected to happen since no heat is absorbed by the compartment's walls resulting in a higher gas temperature that will lead to a hotter gas flow through the doorway. This graph also shows a major difference between the coarse and the medium/fine non-adiabatic cases. The latter two models follow the trend of the experimental data well for almost 75% of the doorway's height but the coarse simulation clearly failed to estimate the temperature values of the higher portion of the door accurately. The medium and fine mesh simulations show a similar pattern without any major differences and the averaged relative difference estimations shown in Table 5.3 are too small for a certain mesh resolution to show evident superiority compared to the rest.

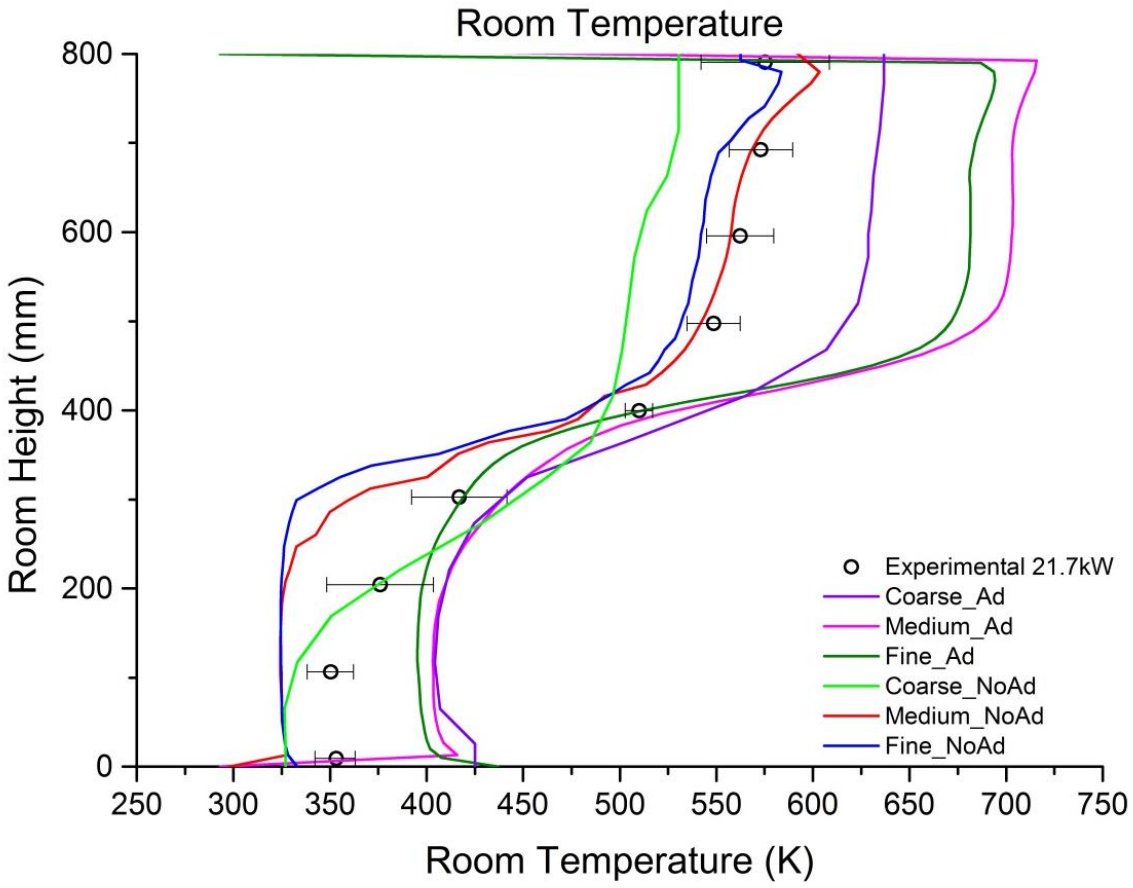

Figure 5.5: Temperature profile at the back center of the small scale compartment

The temperature profile inside the compartment (shown in Figure 5.5) shows a trend similar to that of Figure 5.4 concerning the non-adiabatic simulations. The same results as before show up in the upper half of the temperature profile of the room. Even though the error estimated between the non-adiabatic cases (Medium and Fine) and the experimental values only varies about 1.8% between the two simulations, the bottom half of the room shows a completely different behavior. At the lower half of the room a variation occurs whose possible cause might hide in the simulation time. It is possible that a simulation using the same input file but with a double as long simulation time might correct that part by increasing the radiation coming from the lower and colder part of the walls. The coarse-conductive simulation shows the same behavior as in Figure 5.4, not following the other two conductive simulations' trend but a rather less steep curve of temperature values. The values of the room temperature taken from the Coarse_NoAd simulation appear to have a smaller range, as a result of worse temperature estimation due to the mesh resolution that was used.

For all the adiabatic simulations, within the first 50mm away from the compartment floor, the temperature suddenly rises almost 125K reflecting the adiabatic wall properties. The results still follow the main trend of the experimental data meeting them only twice, close to the neutral plane's height. That can be coincidental due to the stratification that occurs in the compartment, leading to a temperature value pattern that qualitatively resembles the experimental.

Figure 5.6 presents the V velocity component on the doorway of all six cases. The mean velocity profile keeps the same shape as the V-component since the other components' contribution through

the doorway plane is minor. The test cases examined in this study are all buoyancy driven, so the velocity profiles are generally expected to develop in a way reflecting the temperature's profile. In that manner, the velocity profile reflects the stratification that occurs in the room presenting a flow pattern similar to the experimental.

The adiabatic test cases show greater absolute values in both the lower and the upper part of the doorway. That is explained by the overall higher temperatures that were reached inside the compartment leading to a stronger outflow of hot gasses and consequently stronger inflow of fresh air in the room. The sign on the velocity values reveals the direction of the flow, the positive being the flow out of the room and the negative being the flow of fresh air in the room.

The neutral plane of the flow is exactly on the vertical line set on the zero point of the velocity axis. The fine and medium adiabatic tests' results seem to reproduce the height perfectly but that might be symptomatic as well. Both the fine and medium conductive tests miss that height for about 30mm.

The non-adiabatic cases follow the experimental values perfectly on the bottom half of the door, missing the higher portion, where the non-adiabatic tests are still relatively closer to the experimental values than the adiabatic ones.

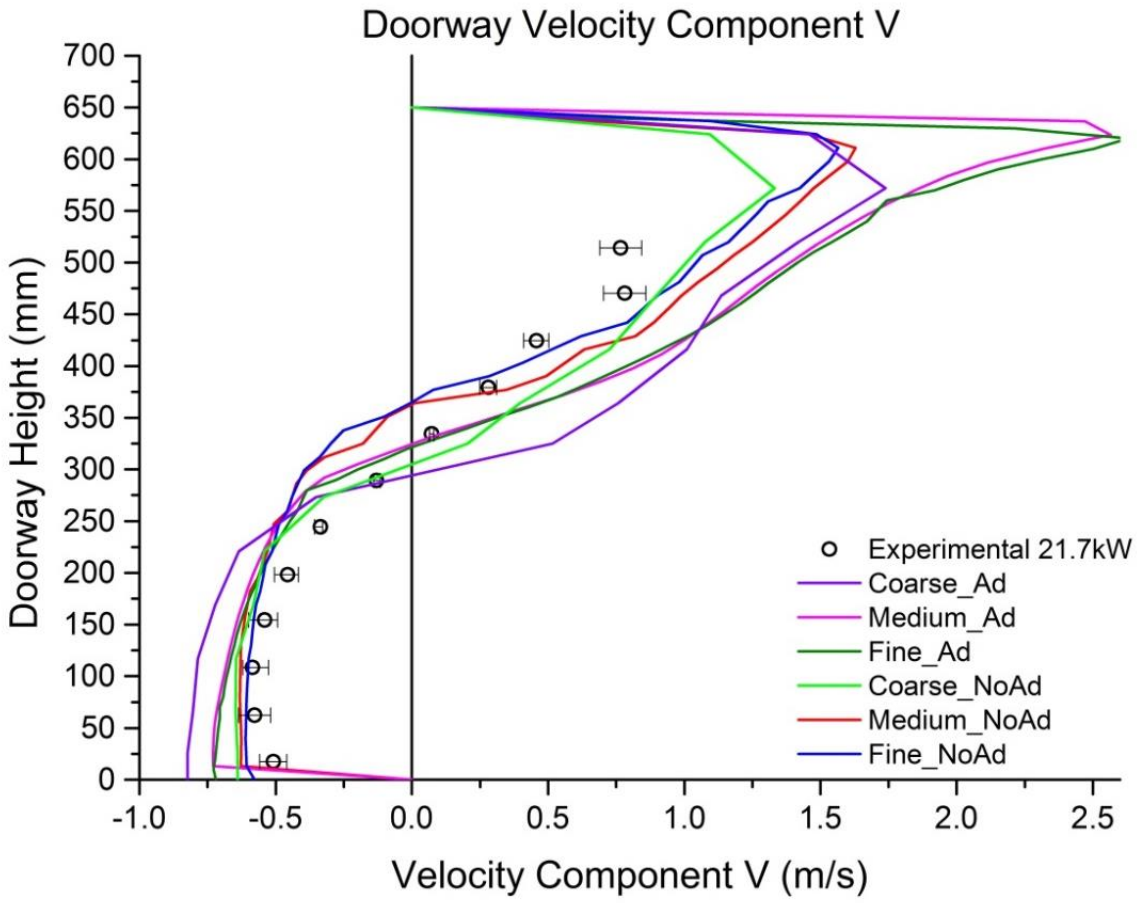

Figure 5.6: Velocity component V on the small scale compartment's doorway

Velocity measurements can be found in the literature for different door heights as well. The values that were obtained from the experiments represent the velocity component V measured at two certain heights (15% and 75% of the doorway height) using the SPIV technique. The lower measurements shown in Figure 5.7 are representative of the horizontal profile of the fresh air's velocity while the higher ones are representative of the horizontal profile the hot gases' velocity on the doorway.

Experimental measurements were provided in the literature for half the doorway's width. These values are shown here in Figure 5.7 presented by the black symbols. All experimental values are shown in the left side of the figure (negative x-axis values in the graph) while the center of the doorway is respectively positioned at the zero value of the width-axis (x-axis in the graph).

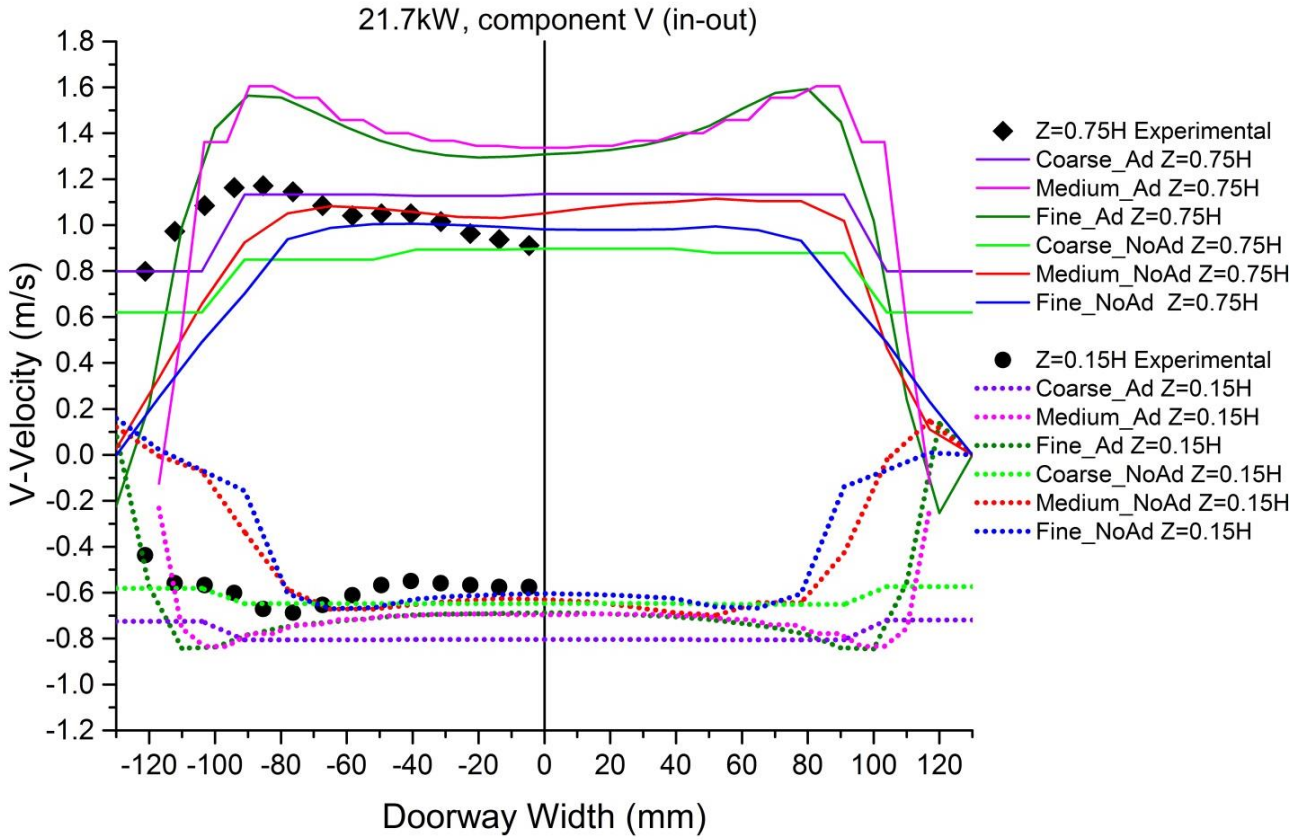

Figure 5.7: Velocity component V on the small scale compartment's doorway. Measurements are presented for two horizontal lines at the height of 97.5mm ($z=0.15H_O$) and 487.5mm ($z=0.75H_O$) .

Table 5.3 presents the estimated errors between the predictions and the available experimental data. The absolute error average (statistical mean) has been computed as the average value of the velocities' error estimates appearing above it in Table 5.3. For this calculation the error estimates have been replaced by their absolute values. Equation **(5.1)** shows an example of this calculation for *n* given velocity error values x_i. The results of the equation are used in order to decide which of the examined configurations performed better "in average".

$$\text{Absolute Average} = \bar{x} = \frac{|x_1| + |x_2| + |x_3| + \ldots}{n} \tag{5.1}$$

The Standard Deviation for the same set of n values of xi is computed using equation **(5.2)**. Standard Deviation is a statistical measure that is closely linked to Variance. Both measures are commonly used across a set of values, to identify the amount that the values differ (or deviate) from the average value providing an insight to how concentrated the data are around the mean.

$$\text{Standard Deviation} = \sqrt{\sum \frac{(x_i - \bar{x})^2}{n-1}} \tag{5.2}$$

The final equation used in the handling of the data shown in Table 5.3 is the Relative Standard Deviation, also known as Coefficient of Variation. This is defined as the ratio of the standard deviation to the absolute value of the statistical mean. The coefficient of variation is useful because the standard deviation of data must always be taken into account in the context of the mean of the data. In contrast, the actual value of the CV is independent of the unit in which the measurement has been taken, so it is a dimensionless standardized measure of dispersion and precision.

As it has been shown, the adiabatic simulations resulted in data of significantly lower overall accuracy. For that reason it is safe to say that a simulation using conductive wall properties is the safest way to a more accurate approach of the case examined here. The preferred resolution of the grid is yet to be chosen. The value of the mean relative error used here for the models' verification and grid sensitivity study has been mentioned and endorsed in the literature by many scientists and researchers (Ierardi and Barnett, 2003; Audouin et al, 2011). The calculation of the relative error values is based on equation **(5.3)** using the values obtained by simulation (Comp) and experiment (Exp).

$$\text{Relative Error} = \frac{(\text{Comp} - \text{Exp}) * 100}{\text{Exp}} \% \tag{5.3}$$

Even though Figure 5.5 shows the superiority of the non-adiabatic cases, the error calculation (meaning relative difference from certain available values) does not take the standard deviation of the data into account. Having three times higher standard deviation than the adiabatic error estimates (calculation process and results are not shown for easier readability), the "conductive" simulations' error estimates for the V-velocity component at Z=0.15H cannot be considered reliable.

Things are different for the V-velocity component at Z=0.75H. At this height the standard deviation between the error estimates, remain relatively on the same values for both the adiabatic and the non-adiabatic simulations.

Table 5.3: Calculation of the relative error for all cases examined for the 21.7kW fire in a small scale compartment.

Small Scale Compartment - 21.7 kW						
Case	**Coarse_Ad**	**Medium_Ad**	**Fine_Ad**	**Coarse_NoAd**	**Medium_NoAd**	**Fine_NoAd**
Doorway Temperature (K)	11.10%	10.80%	9.50%	4.20%	2.10%	4%
Room Temperature (K)	11.20%	16.50%	13%	7.90%	5.60%	7.40%
Doorway V-Velocity (m/s)	73.70%	36.80%	39%	41.00%	32.20%	27.50%
V-velocity at Z=0.15H (m/s)	34.30%	25%	27%	13.10%	32%	35%
V-velocity at Z=0.75H (m/s)	11.10%	36%	34%	26.90%	14%	21%
Velocity Absolute Error Average	39.70%	30.50%	33.30%	27.00%	26.10%	**27.80%**
Velocity Standard Deviation	0.3167	0.0778	0.0603	0.1394	0.1045	**0.0701**
Relative Standard Deviation	0.80	0.26	0.18	0.52	0.40	**0.25**

The optimum grid resolution for the 21.7kW experiment can be based on another critical factor, namely the mass flow rate error. As seen in a chapter 4, the integration of the experimental data measured on the compartment's doorway yielded an accurate estimation of the mass flow rate through the doorway for both the inflow and the outflow. Those values were compared to the numerical values estimated by the 6 simulations that were made leading to the results presented in Table 5.4.

The simulation giving the best results in each table (from a statistical point of view) is marked in grey.

Table 5.4: Calculation of the mass flow rate error for all cases examined for the 21.7kW fire in a small scale compartment.

Small Scale Compartment - 21.7 kW						
Case	**Coarse_Ad**	**Medium_Ad**	**Fine_Ad**	**Coarse_NoAd**	**Medium_NoAd**	**Fine_NoAd**
Mass Inflow Error	-42.10%	-13.80%	-14%	-25.50%	**5.50%**	8.20%
Mass Outflow Error	-58.40%	-15.70%	-15.70%	-39.70%	**2.80%**	-2.80%

From the values presented in Table 5.4 the superiority of the Medium and Fine conductive simulations is made clear. That combined with the results of Table 5.3 shows that the **Fine_NoAd** simulation presents the best overall error percentages and characteristics of the flow, meaning the pattern and values of the quantities shown in the graphs.

5.5.2. Validation of the 15.5kW case

The second and last experiment that will be examined concerning the small scale compartment involves the 15.5kW case. In the same way as before, computational data are compared to experimental values provided by the literature. Since the results of the 21.7kW case showed a clear superiority of the conductive simulations, only the conductive simulations' results will be presented for the 15.5kW case, for easier readability.

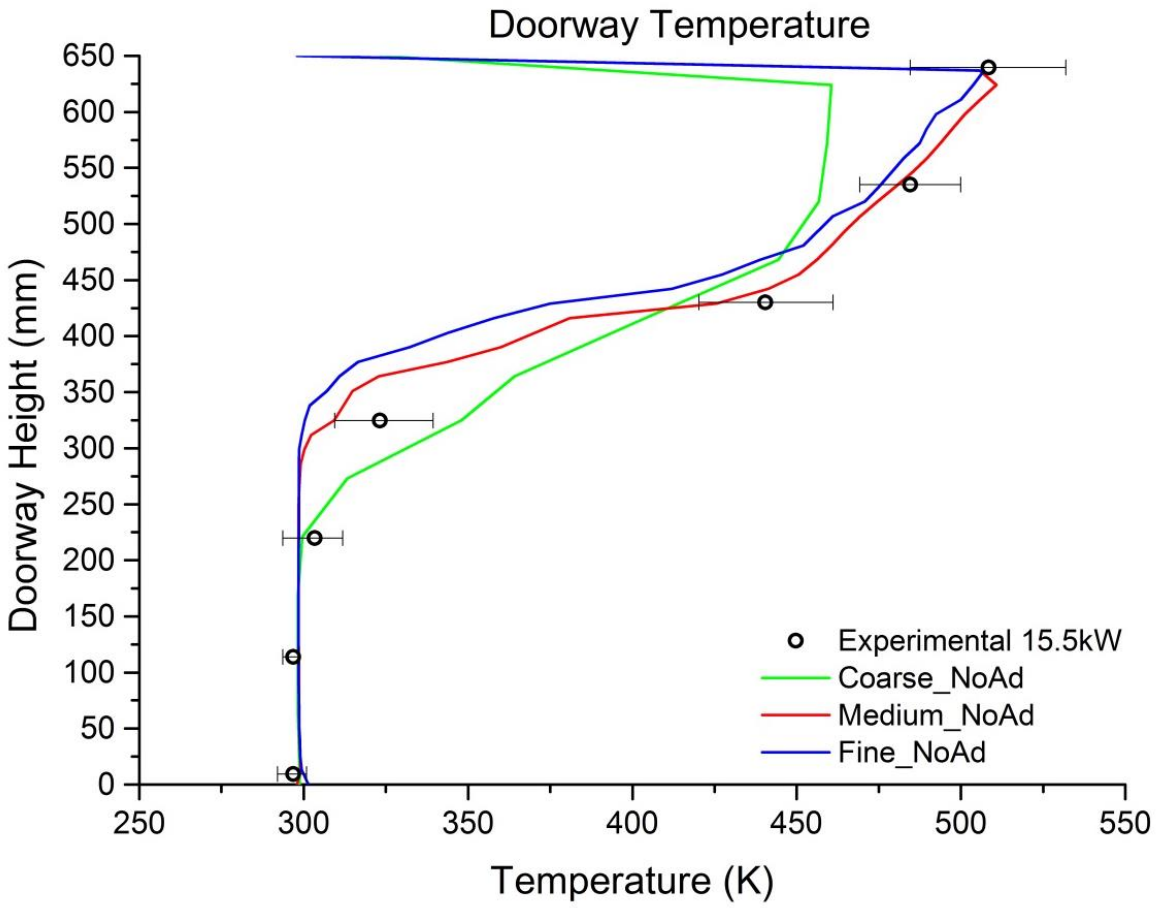

Figure 5.8: Temperature profile at the door of the small scale compartment

Figure 5.8 shows the temperature profiles appearing on the doorway of the compartment. Similar to the 21.7kW simulations, the coarse mesh failed to predict the temperature values accurately while the rest performed similarly.

The lines standing for the medium and fine mesh resolutions show a difference of 2.2% between them in terms of error between experimental and computational values. This is a small number but the general trend of the phenomena taking place in such buoyancy driven flows, is reflected in the vent's temperature profile. For that reason, the most precise mesh resolution is already expected to be found between the medium and fine resolutions.

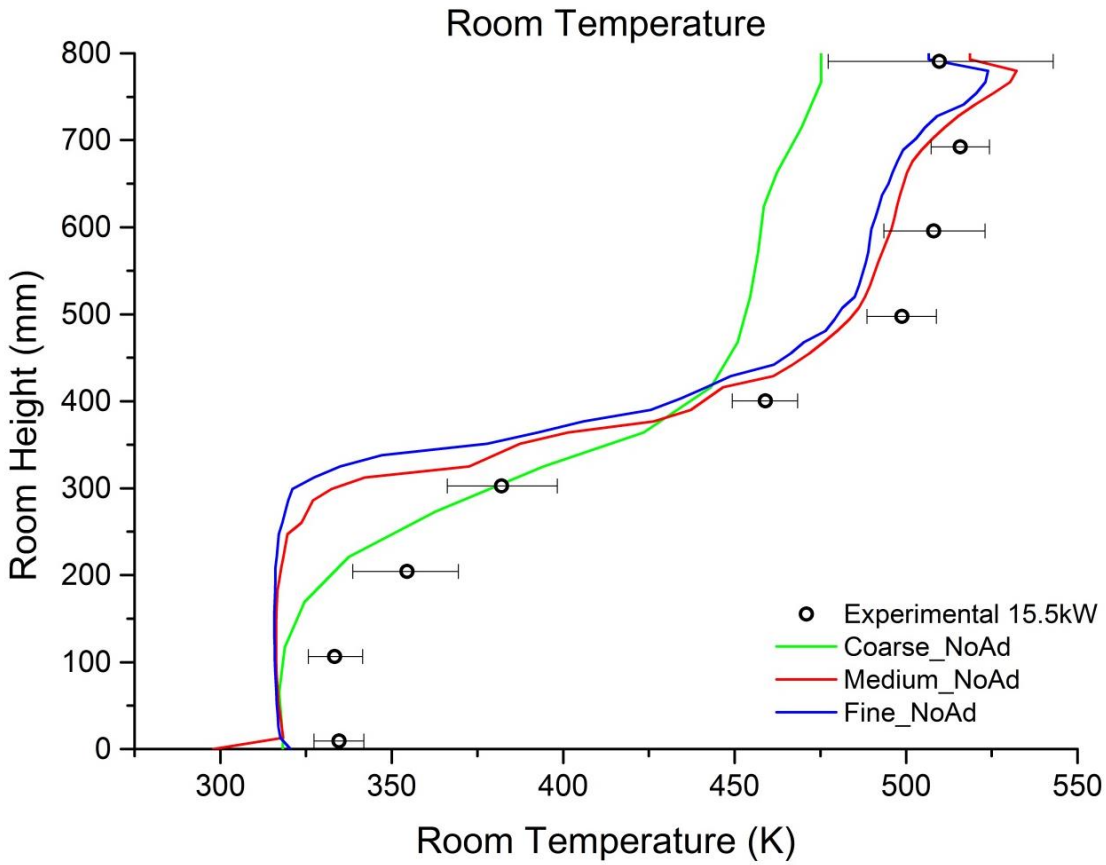

Figure 5.9: Temperature profile at the back center of the small scale compartment

The temperature profiles measured in the back center of the room are presented in Figure 5.9. In the same manner with the doorway temperature profiles, the coarse mesh failed to predict the experimental profile on the whole height of the room. The estimation of temperature on the bottom half of the door appears to be better for the coarse mesh, which is most probably coincidental; Again, the curve shows significantly lower range than the other two, most probably due to the coarse grid's failure to accurately simulate the phenomena taking place in the compartment.

The Medium and Fine cases show a similar pattern with small differences between them. It is clear that the two cases show somewhat "parallel" evolution with just a 1.8% difference of estimated error separating them.

The velocity profiles of the V-velocity component are presented in Figure 5.10. As expected the trend of the temperature profiles is reflected on those results.

The fine mesh resolution case shows a very accurate description of the flow field especially for the lower portion of the doorway. All cases missed the neutral plane's height, with the fine and the coarse grids missing it the closest from either side. Even though the medium mesh misses the neutral plane the worst, its' overall profile shows very similar behavior to the fine mesh's profile. In most cases where the fine grid estimated the velocity value perfectly, the medium mesh's prediction is within the error tolerance.

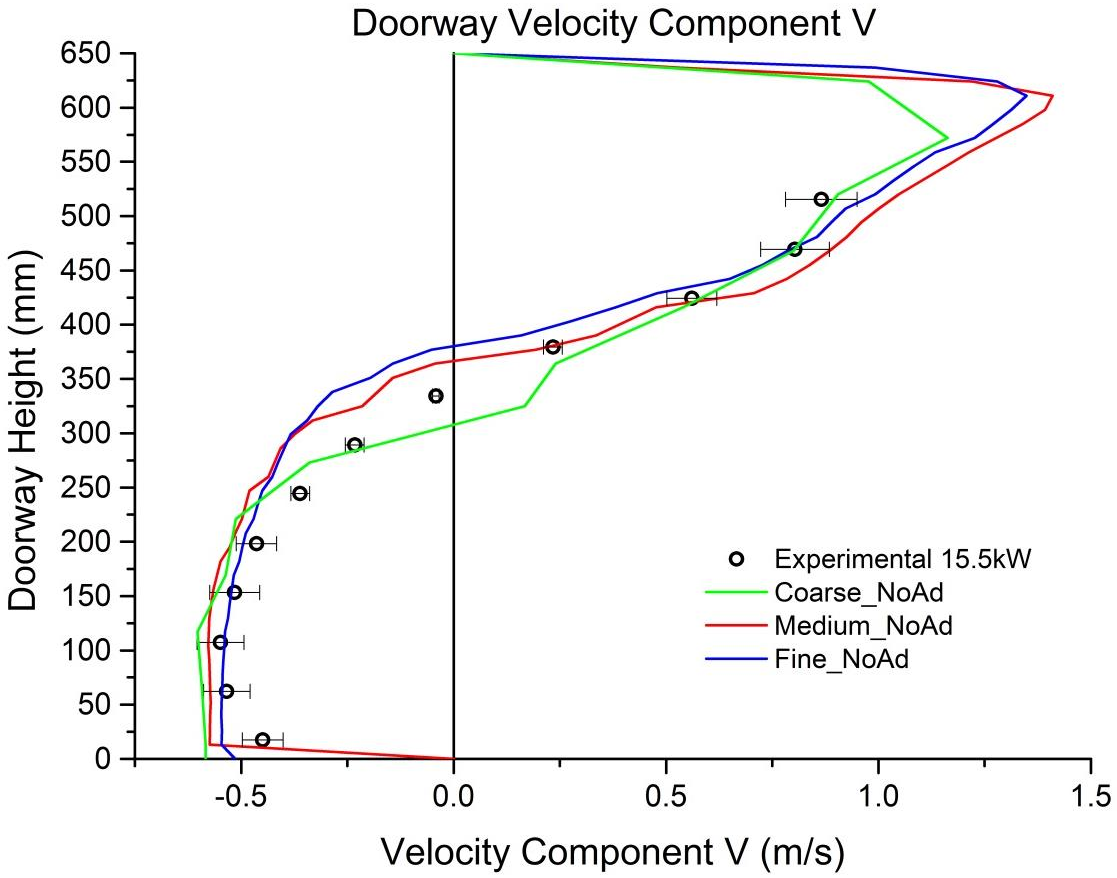

Figure 5.10: Velocity component V on the small scale compartment's doorway

The coarse grid seems to have overestimated the inflow velocity while underestimating the outflow. A probable cause for this can be the failure of the grid to satisfy the *fire diameter criterion* (Equation (3.2)) as a sufficiently fine grid would, lacking the necessary resolution. None of the remaining criteria mentioned in this study concerning the mesh resolution is fulfilled while using the coarse grid, either. Since the remaining two criteria take the vent's dimensions into account rather than the fire power, the phenomena taking place on the vent were actually expected to have not been described accurately.

In Figure 5.11 the profiles of the V-velocity component at two certain heights are compared to the experimental values appearing in the literature. The measurements were again made at 15% and 75% of the total doorway height and the experimental values are depicted with black symbols.

The results obtained from the simulations gave an unexpected outcome where the coarse the grid gave the most accurate results. That might be symptomatic since the flow on the doorway is not symmetric and it is obvious that the results show minor differences compared to the resolution change between the simulations. The error estimation shown in Table 5.5 between experimental and computational values shows that the coarse grid is the most accurate and the fine grid is the least accurate for these measurements.

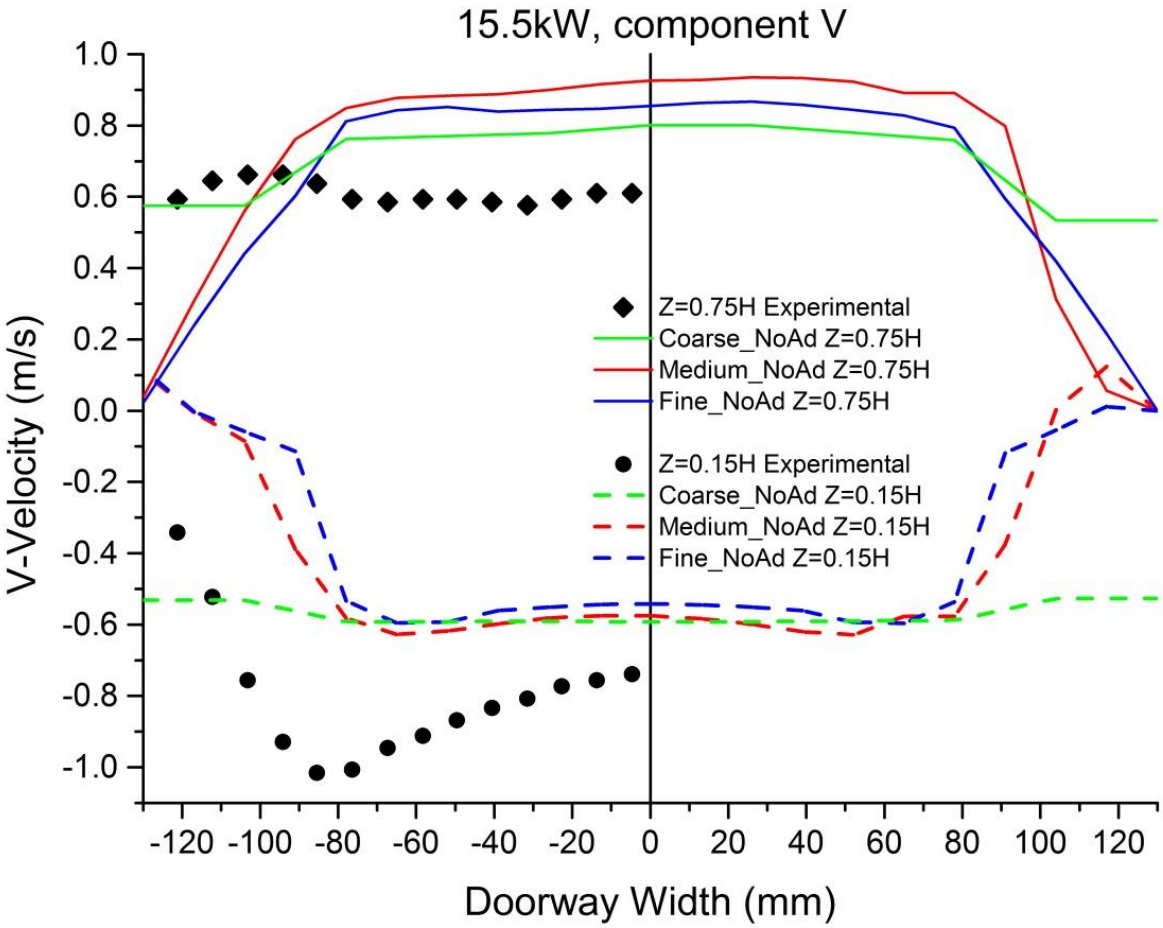

Figure 5.11: Velocity component V on the small scale compartment's doorway. Measurements are presented for two horizontal lines at a height of 97.5mm ($z=0.15H_O$) and 487.5mm ($z=0.75H_O$).

Table 5.5 shows the average error calculated for each quantity described and presented in the graphs above, with lines 8 and 9 showing the average of the velocity error values calculated, and the standard deviation of these values. The standard deviation's values help distinguish which simulation is considered the most trustworthy by calculating the coefficient of variation, presented in the last line of the table. In that way the coarse mesh is the one that has the most consistent results while the fine grid has the least precise results. Since these statistical values are calculated in terms of velocity measurements and only, they neglect the results of the temperature measurements. In that field, the medium mesh gave the most precise results leaving the other two with similar outcomes. The error averages in terms of velocity show a clear dominance of the Fine_NoAd case again, but with triple divergence between its values compared to those of the coarse simulation. The mass flow rate estimation error is left with the task to reveal the most precise simulation.

Table 5.5: Calculation of the relative error for all cases examined for the 15.5kW fire in a small scale compartment.

Small Scale Compartment - 15.5 kW			
Case	**Coarse_NoAd**	**Medium_NoAd**	**Fine_NoAd**
Doorway Temperature (K)	5.50%	1.70%	3.90%
Room Temperature (K)	7.30%	4.10%	5.90%
Doorway V-Velocity (m/s)	16.70%	17.10%	8.50%
V-velocity at Z=0.15H (m/s)	32.90%	45%	35.80%
V-velocity at Z=0.75H (m/s)	27.10%	47.10%	39.30%
Velocity Absolute Error Average	25.50%	36.40%	18.70%
Velocity Standard Deviation	0.0819	0.1673	0.1736
Relative Standard Deviation	0.32	0.46	0.93

The mass flows rates' averaged values of each simulation have been compared to the values obtained by integration of experimental data on the doorway plane and are presented in Table 5.6. The results show the certain dominance of the fine mesh, while the coarse mesh has –as expected- failed to compute the mass flow rates through the doorway completely. The greatest fluctuation between the values of the table appears between the inflow rates where the coarse simulation shows the significance of an adequate mesh resolution. The difference between the medium and fine tests is 7.2% for the inflow and 30% for the outflow, showing that the mesh resolution does not only need to be adequate but a mesh sensitivity study is also important.

Table 5.6: Calculation of the mass flow rate error for all cases examined for the 15.5kW fire in a small scale compartment.

Small Scale Compartment - 15.5 kW			
Case	**Coarse_NoAd**	**Medium_NoAd**	**Fine_NoAd**
Mass Inflow Error	41.70%	-5.80%	1.40%
Mass Outflow Error	19.30%	17.10%	-13.40%

5.6. Main Flow Field Characteristics

The flow characteristics and values presented in the graphs and tables of the previous section point the **Fine_NoAd** simulations out as the most precise. That is in terms of overall result quality both in temperature and velocity predictions as well as in terms of mass flow rate calculation. For that reason the flow field characteristics of those simulations and only will be presented in this chapter. The figures that follow present images reflecting certain quantities' evolution in the computational domains, obtained from the Smokeview utility provided with FDS. The time period/frame over which the images were obtained is chosen in order to introduce the viewer to a representative instance of the flow field.

In Figure 5.12 the temperature in the compartment is shown colored from blue to red for $0^{O}C$ to $1000^{O}C$ respectively. The stratification in the room is shown on almost the same height for both cases, just short of the middle of the room's height. The hot gas layer forming in the lower picture (15.5kW case) shows significantly lower "average" temperature. This is expected and also seen in the graphs of this chapter where the maximum temperature inside the room reached around 500K in the 15.5kW simulations while the 21.7kW simulations showed a maximum value of around 50K higher.

Some trails of hot gasses between the lower portion of the doorway and the burner help visualize the entrainment flow. The flow is in all cases fire-driven and therefore stronger in the experiment using the strongest fire. The difference in the pictures is minor due to the small difference in terms of fire output. The same is true for the outflow of hot gases from the doorway. The 21.7kW simulation shows a hotter stream exiting the compartment which leads to a stronger flow with more intense mixing of the two flows at and under the neutral plane height.

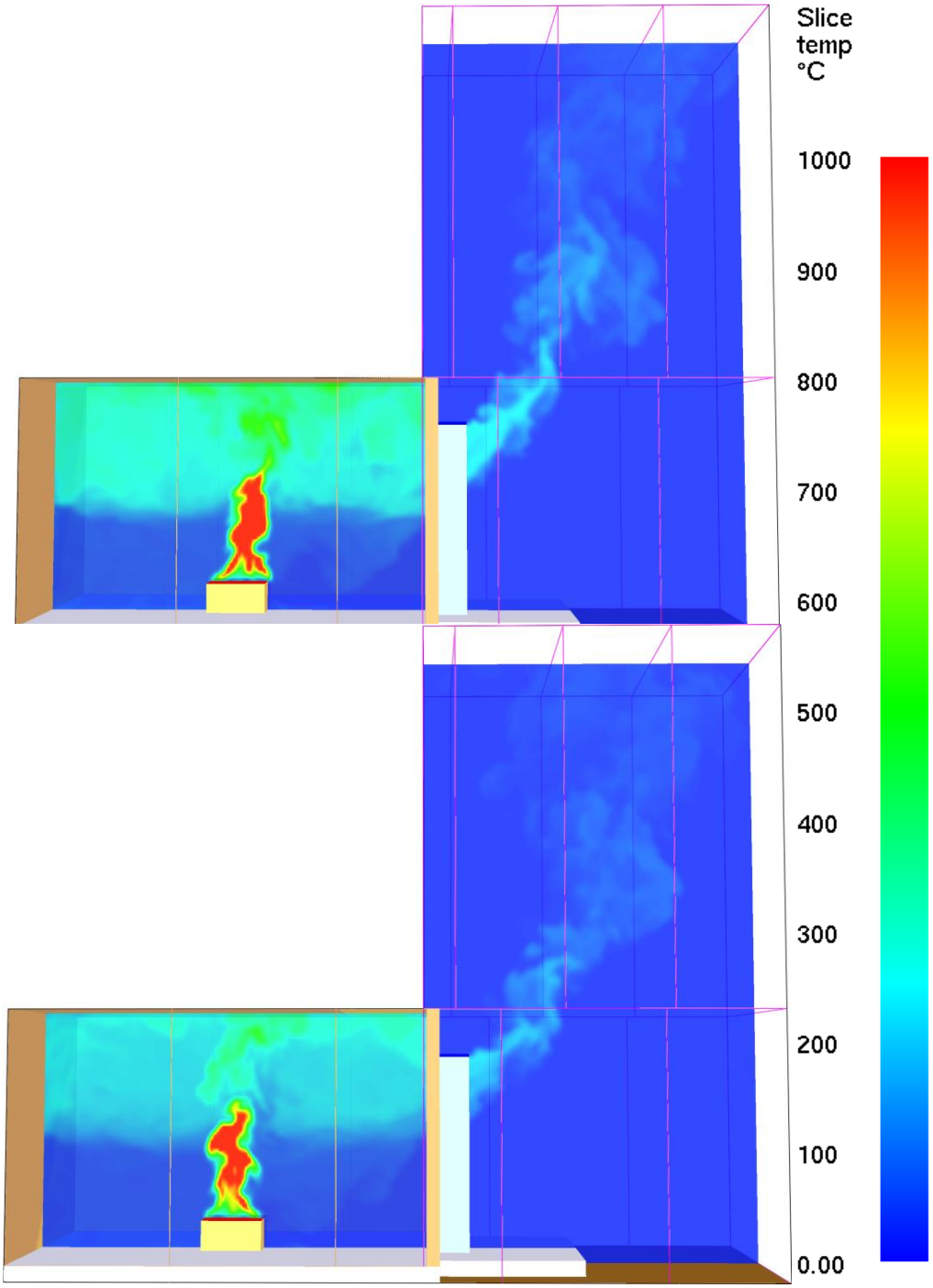

Figure 5.12: Temperature contours for the *Fine_NoAd* 21.7kW (top) and the *Fine_NoAd* 15.5kW (bottom) test cases.

The entrainment flow inside the room behind the doorway is made evident in Figure 5.13, where predictions of mean velocities are depicted. The neutral plane appears to be close to the 60% mark of the doorway height in both cases but that will be presented clearly later.

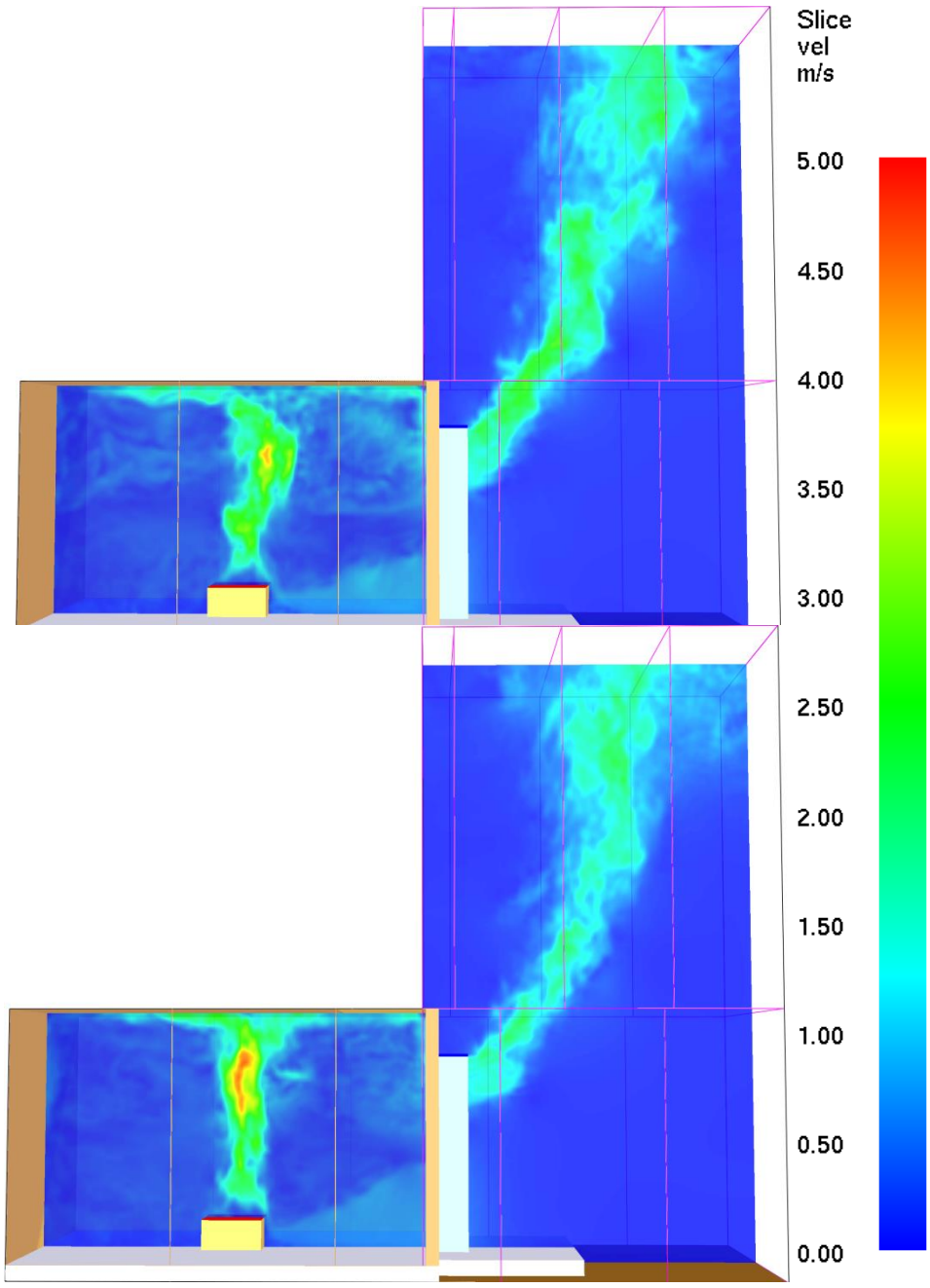

Figure 5.13: Mean velocity contours for the *Fine_NoAd* 21.7kW (top) and the *Fine_NoAd* 15.5kW (bottom) test cases.

The mixing in the back of the room is very similar in the simulations even though the 15.5kW simulation reveals a less intense flow in terms of appearing turbulences. The same observation can be made based on Figure 5.14 where the recirculation found behind the burner seems more homogenous in the 15.5kW case for the two gases' layers. This is also true for the area between the doorway and the burner as well, where the 21.7kW case shown in the top picture reveals significantly stronger entrainment between the outflow and the inflow layers. The characteristics of the flow reflect the necessity of proper fire modelling in order to predict the flow mechanisms taking place in the compartment accurately. In the same area, between vent and fire, the vena contracta diameter appears to be slightly smaller in the 21.7kW case, which is expected since the flow is stronger.

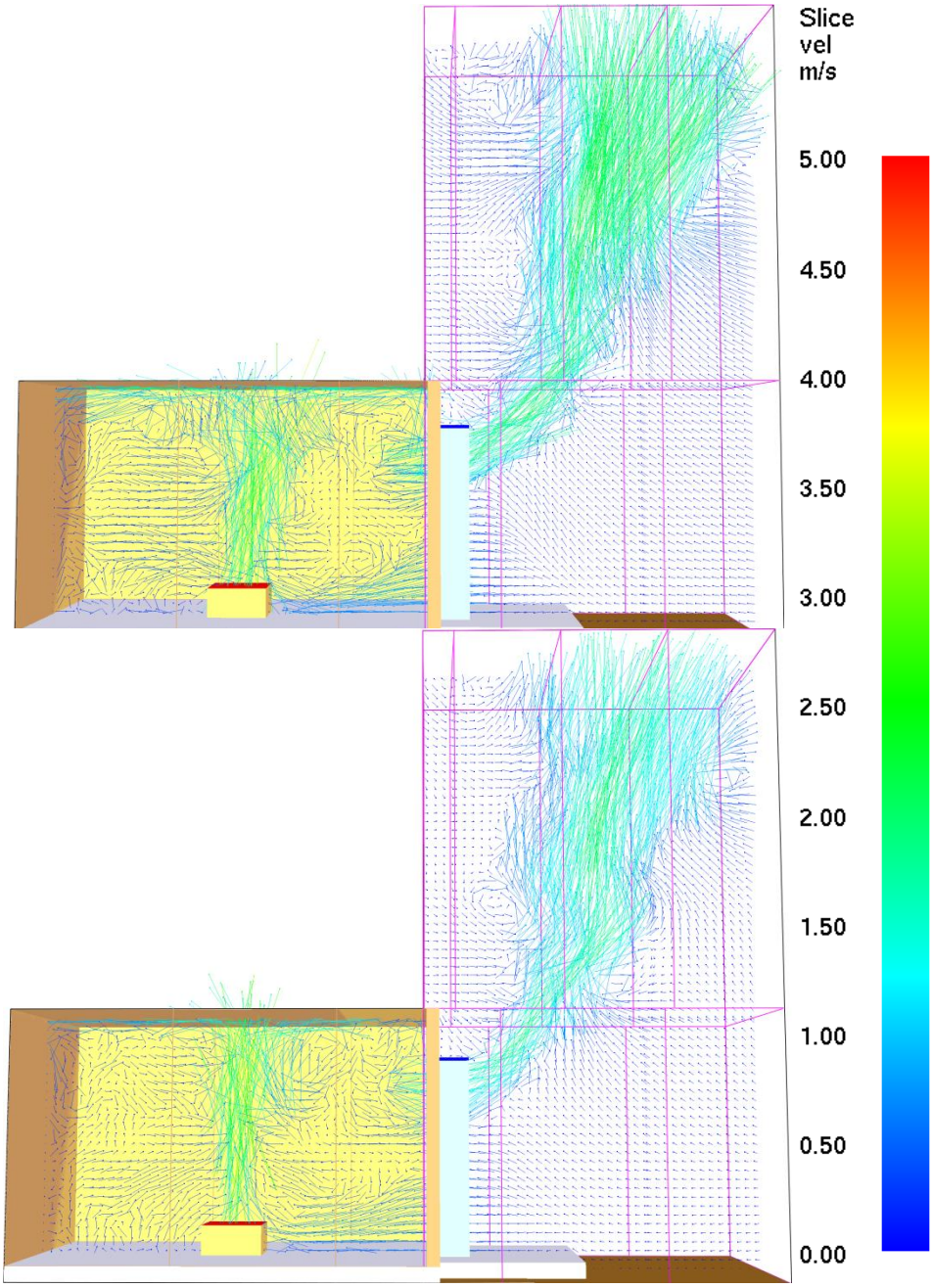

Figure 5.14: Mean velocity vectors for the *Fine_NoAd* 21.7kW (top) and the *Fine_NoAd* 15.5kW (bottom) test cases.

The ambient space that was used for the simulations is another area that requires attention. Even though the mesh was extended as far as 260% the suggested length, it is clear that streams of fresh air origin from the far limit of the simulation's domain and merge into what finally becomes the inflow of fresh air through the doorway. Missing out on these details may lead to false assumptions for the flow inside the compartment, possibly creating false flow patterns as found by Gutiérrez-Montes et al (2012).

Figure 5.15 presents a contour of the velocity component V on the doorway plane, meaning the velocity component with a direction perpendicular to the doorway plane. The two images present solely doorway plane, as viewed from the outside. The orange-red color on the bottom portion of the contours reveals the direction of the flow in the compartment, while the green-blue color on the higher portion of the door shows the direction of the flow towards the ambient space (outflow of hot gases).

It is evident, that both cases present the neutral plane at the same height, a little over 55% of the total door height. The velocity contour of the 21.7kW simulation is darker revealing that the inflow is more intense in this test. A stronger flow in such "steady-state" pre-flashover conditions is expected to give a smaller diameter of the vena contracta which is correctly presented in Figure 5.14. The velocity profiles shown also reveal that the flow on either side of the doorways is asymmetrical. That explains the asymmetries found in Figure 5.7 and Figure 5.11 presenting V-velocity results. It is therefore very important that the measuring devices are positioned properly.

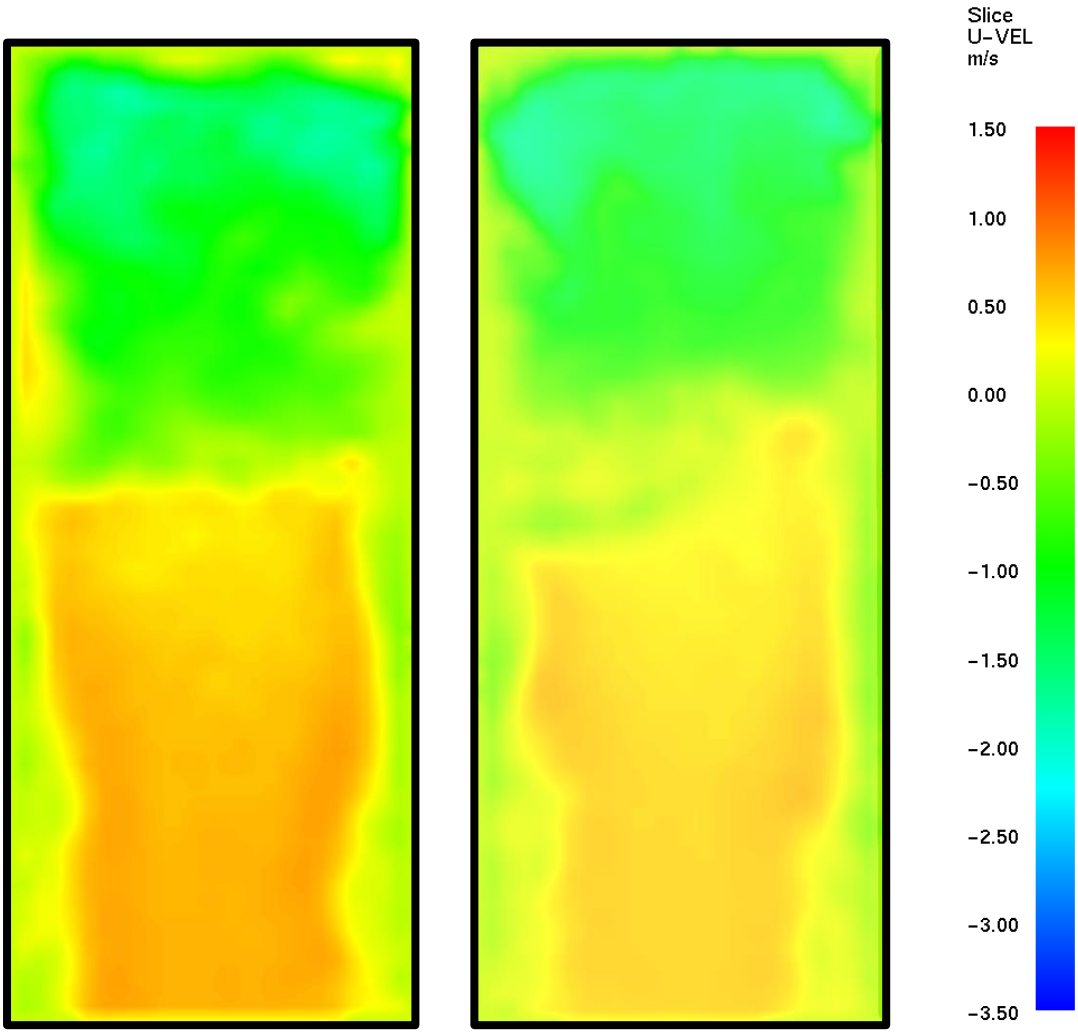

Figure 5.15: Velocity component V on the small scale compartment's doorway for the *Fine_NoAd* 21.7kW (left) and the *Fine_NoAd* 15.5kW (right)

6. Computational Simulation of Fire in a Large Scale Compartment

Similar to the small scale compartment simulation the procedure that was followed was a numerical simulation using the FDS code, Version 6.3.2. The simulations are based on the experiments made by Bryant (Bryant, 2011; Bryant, 2009a; Bryant, 2009b). The data acquisition was made possible by utilizing the sensors' position and other configuration characteristics as described by Bryant (2009a).

Some necessary assumptions were made in order to find the Golden Section between conforming to the code's guidelines and being true to the original experiment variables. The assumptions and decisions that were made will be discussed in this section.

6.1. Parametric Study

A parametric study in terms of different models and assumptions was made in order to evaluate the flow field characteristics.

The heat release rate (HRR) was examined for two values examined in this experimental configuration: 160kW and 320kW.

The corresponding heat release rate per unit area for each case can easily be calculated by dividing the desired kW value by the burner's area. That way, a HRRPUA value of $160/(0.3)^2$=1777.78kW/m^2 for the 160kW test case and a HRRPUA value of $320/(0.3)^2$=3555.56 kW/m^2 for the 320kW case are obtained.

The computational grid resolution was also examined using the same Cartesian cubic discretization technique as before. The sizes of the meshes' cells that were examined were 30mm (fine mesh), 50mm (medium mesh) and 100mm (coarse mesh). The effects of the alternatives that were used will be displayed through analytical comparative graphs in another section.

The cases that were examined and will be presented in this section are compared to experimental values that have been widely used throughout the literature. Six different cases were examined for the 160kW experiment and three for the 320kW experiment, the names of which again reflect the computational cell size and the thermal properties that were assigned to the walls. The names and basic characteristics of each case are presented in Table 6.1.

Table 6.1: Names, mesh cell sizes and walls' thermal properties of the examined cases.

Case Name	HRR simulated (kW)	Mesh Cell Size (mm)	D*/δx	Wall Thermal Boundary Conditions
Coarse_Ad	160	100	4.61	Adiabatic
Medium_Ad	160	50	9.22	Adiabatic
Fine_Ad	160	30	15.37	Adiabatic
Coarse_NoAd	160	100	4.61	Conductive
Medium_NoAd	160	50	9.22	Conductive
Fine_NoAd	160	30	15.37	Conductive
Coarse_NoAd	320	100	6.08	Conductive
Medium_NoAd	320	50	12.16	Conductive
Fine_NoAd	320	30	20.27	Conductive

All the test cases using the medium mesh are available in and were created for the FDS validation test suite, provided by the National Institute of Standards and Technology (McGrattan et al, 2015a)

In Table 6.2 the values of the criteria presented in section 3.2 are displayed in comparison to their minimum limits. Once again in most cases the cell sizes are in a safe zone away from the limits that are suggested in the literature for the given dimensions/fire sizes except for the cases marked in grey. The 50mm case was originally examined and presented throughout the literature (McGrattan, 2015).

Table 6.2: Comparison between calculated values of the three criteria and their suggested limits

Source	**Bryant (2009a)**				**Bryant (2009a)**			
HRR	*160 kW*				*320 kW*			
Cell Size	30mm	50mm	100mm	Limit	30mm	50mm	100mm	Limit
$D^*/\delta x$	***15.37***	***9.22***	***4.61***	≥ 10	***20.27***	***12.16***	***6.08***	≥ 10
l_1^*	***45.4***	***27.25***	***13.63***		***45.4***	***27.25***	***13.63***	
l_2^*	***37.5***	***22.5***	***11.26***		***37.5***	***22.5***	***11.26***	

Another aspect that was examined in this experiment as well concerned the wall thermal boundary conditions. The analysis was limited in the application of both conductive and adiabatic boundary conditions on the surfaces of the compartment.

6.2. Initial Values and Boundary Conditions

Again, the ambient temperature has been set to the standards used in the original experiment, being **21.5°C**.

Since the data that were used for comparisons are averaged over the time period when the conditions reached a quasi-steady state, it is necessary to find the time period when that steady state has occurred. Following the steps of the original simulations in FDS conducted by Bryant (2005), the time limit for all further simulations was set to be 1800 seconds. All data presented in the following sections represent time-averaged quantities of the last 900 seconds of the simulations. That is from the 900 second mark, to the 1800 second mark. Again, a TIME_SHRINK_FACTOR was employed, equal to 10, shrinking the computation time to 1/10 of what would be necessary if this parameter was not used, while speeding up the heating of certain materials roughly by 10.

As described in the literature, fires were generated using a natural gas burner placed in the center of the ISO room, with the top of the burner being 30cm above the room floor. Instead of using a very complex gas mixture reaction the burning fuel was replaced by methane (CH_4). The only constant

declared in the code concerning the fuel was the species and the SOOT_YIELD which was set equal to 0.001.

6.3. Simulation Details

Similar to the small scale experiment above, an attempt was made throughout the code process of creating the model to remain as close to the original proportions of the geometry as possible. The physical properties of the walls, the floor and the ceiling such as conductivity, specific heat, density and thickness were maintained as described in the literature.

Since all walls are assumed to always back up to the ambient, the attribute BACKING='VOID' was set for all of them with zero thickness. The only exception of this rule is the front wall which has a thickness equal to one computational cell, providing the necessary space for the flow through the door. For the simulations using adiabatic boundary conditions, all wall properties were removed from the input file except for the front wall's thickness attribute, thus allowing for a completely different solution procedure.

All sides of the gas burner were set as INERT, except for the upper side where the fuel and the soot yield were explicitly specified.

The dimensions of the glass panels (used for the SPIV measurements in front of the doorway) that were used in the simulation set the panels to be 30mm/50mm/100mm thick, protruding 270mm/250mm/200mm from the outside wall respectively for each cell size case.

The ambient environment was discretized using cells of the same size as for the compartment. The extension of the mesh in the space outside the experimental was again made following the instructions mentioned in Section 3.2. The final ambient area dimensions extend 2.16m/2.2m/2.1m away from the front wall in the z-axis, 2.4m wide in the x-axis and 3.78m/3.8m/3.4m high in the y-axis respectively for each cell size case. The axes labeling is different from that of the small scale compartment simulation following the standards described in the literature that had the gravity vector take effect on the y-axis while the depth of the room was measured on the z-axis. The three configurations described here are presented in Figure 6.1. A detail of the meshing that was used can be seen in Figure 6.2.

It must be noted that the suggested mesh extension (Zhang et al, 2010) in the plane perpendicular to the vent opening (here: z-x plane) was less than 1.2m. All the surfaces created by the extension of the mesh in the ambient environment were declared as VENT.

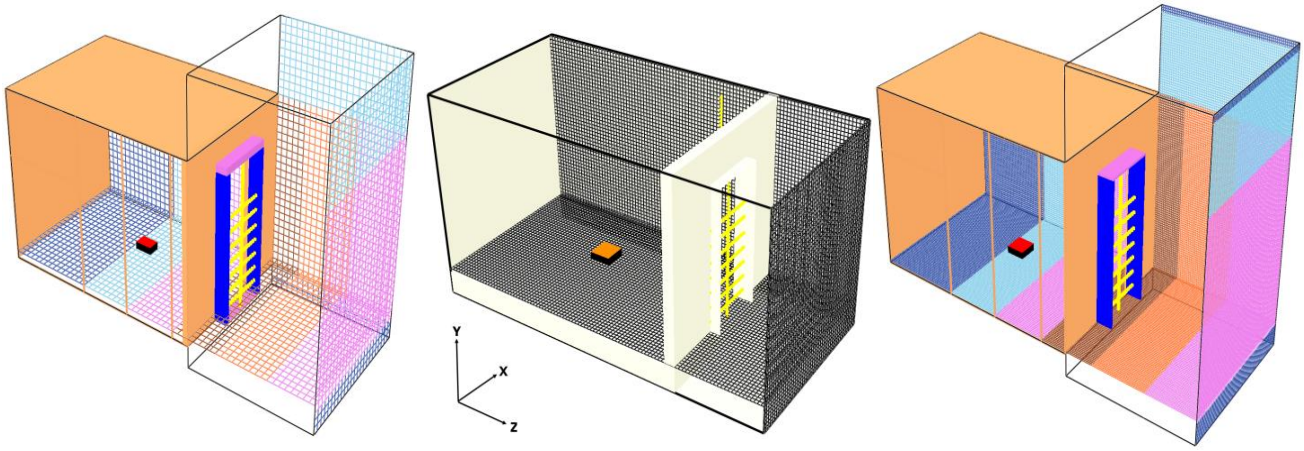

Figure 6.1: Graphic view of the three examined configurations using 100mm (left), 50mm (middle) and 30mm (right) grid.

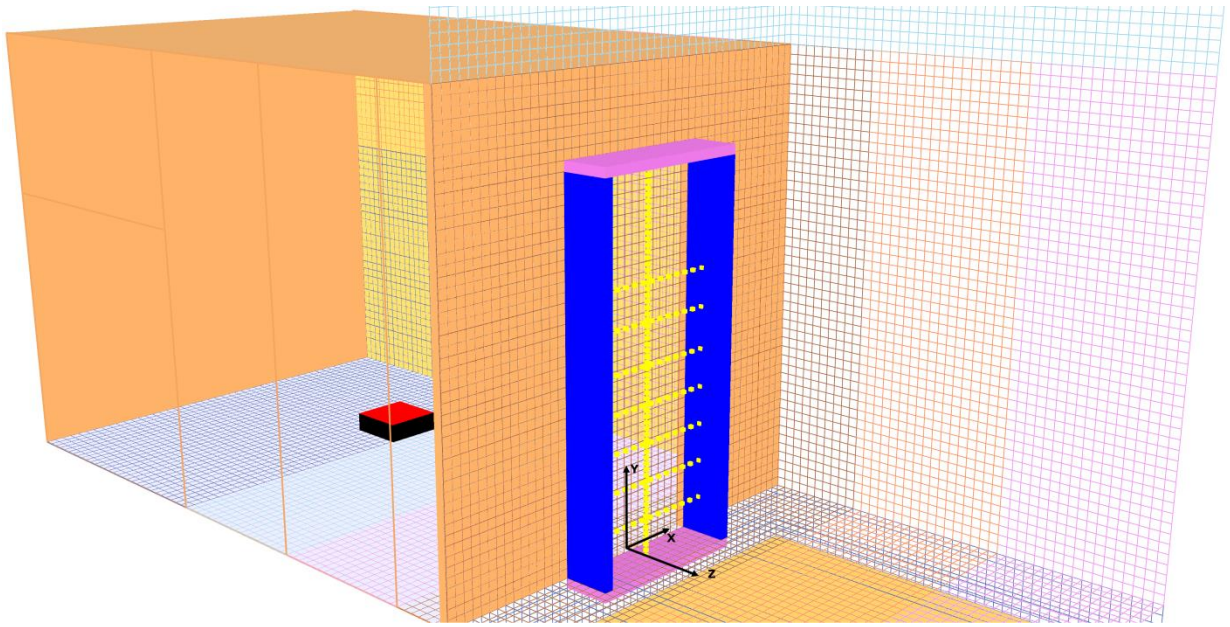

Figure 6.2: Detail of the computation mesh structure

6.4. Data Recording

The position of the temperature and velocity measuring devices was determined by descriptions found in the existing literature (Bryant, 2009b) and prior computational simulation data. That is in the center of the glass panels for the vertical array of doorway devices. Horizontal arrays of devices were also set on seven different heights of the doorway, again exactly as dictated by the existing literature. The heights are defined as certain percentages of the total doorway height, namely 10%, 20%, 30%, 40%, 50%, 61% and 71%.

The vertical arrays of devices consisted of virtual measuring devices placed from Y=0.0m to Y=1.950m, having either 0.03m, 0.05m or 0.1m distance between them. The horizontal arrays were placed as described above at the heights equal to Y=0.195m, Y=0.39m, Y=0.585m, Y=0.78m, Y=0.975m, Y=1.1895m and Y=1.3845m spanning from X=-0.40 to X=0.40 with either 30, 50 or 100mm intervals. A graphic presentation of the said measuring arrangements can be seen in Figure 6.3.

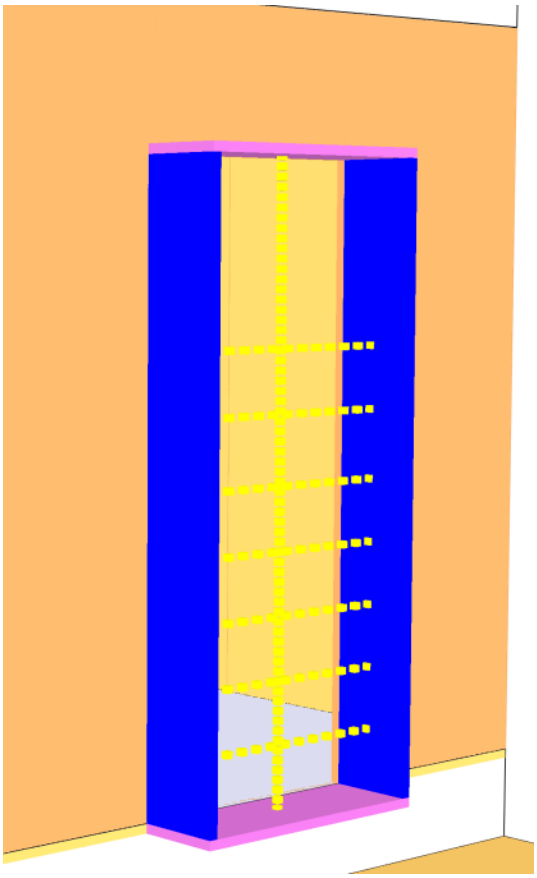

Figure 6.3: Graphic presentation of the doorway's devices' position used in the three configurations

6.5. Validation of Computational Results

6.5.1. Validation of the 160kW case

As shown in Figure 6.4, the temperature data of the simulations are quite inconsistent. At first glance the most precise results seem to derive from the medium and fine adiabatic test cases as well as from the Medium_NoAd, but the absolute error estimation will clear the case.

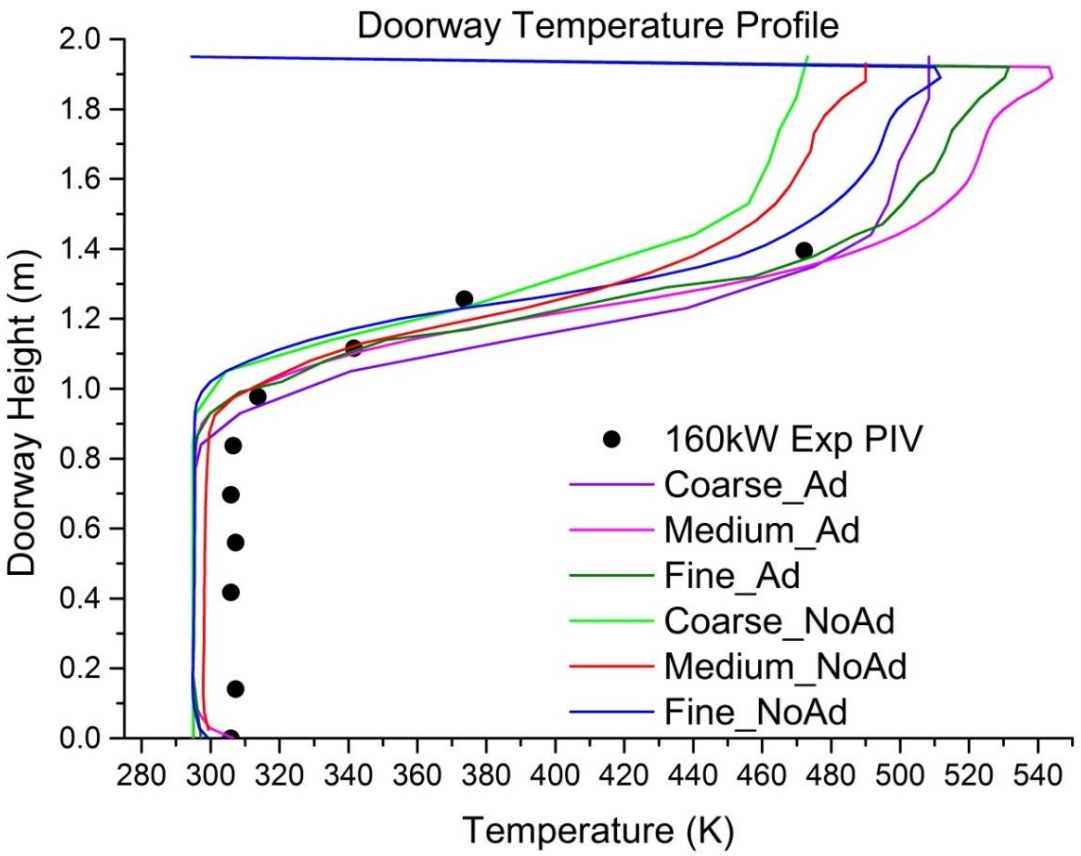

Figure 6.4: Temperature profile at the door of the large scale compartment (160kW)

One interesting aspect of this comparison is how different the coarse and medium-mesh simulations developed between the conductive and the adiabatic case compared to the fine-mesh simulations. At heights greater than that of the neutral plane it is obvious that the difference between the medium tests is more than double the difference between the fine tests and the difference between the coarse tests triples.

All tests described the experimental configuration properly, extending the computational grid to the ambient area by what was thought of being adequate. The test cases built for this study (meaning all the cases except for the Medium_NoAd) extended as far as 1.95m/2m from where the glass panels used for the PIV measurements ended, while the original test case built by Bryant (Medium_NoAd) extended 1.1m. The suggested extension according to Zhang et al (2010) is 1.2m.

Two more differences that might have played a role in the results also concern the definition of the ambient space. As mentioned in a previous chapter, the simulations' ambient space extended as high as 3.4m-3.8m. The original simulation grid developed by McGrattan et al (2015a) extended up to 2.4m being flush with the compartment's ceiling.

The last major difference that can be found between the original and the cases built for this study concerns the space underneath the compartment's doorway. In the literature it is mentioned that the floor of the ISO 9705 room was set 0.29 ± 0.01 m above the laboratory floor (Bryant, 2009b). It is possible that the space underneath the compartment was available for the air to flow freely or completely shut leaving no space for fresh air to flow through towards the doorway of the facility. All

the reports of the case Medium_NoAd presented in here simulate the aforementioned space as shut, while all the rest simulate that space as an open "vent" letting the air flow freely.

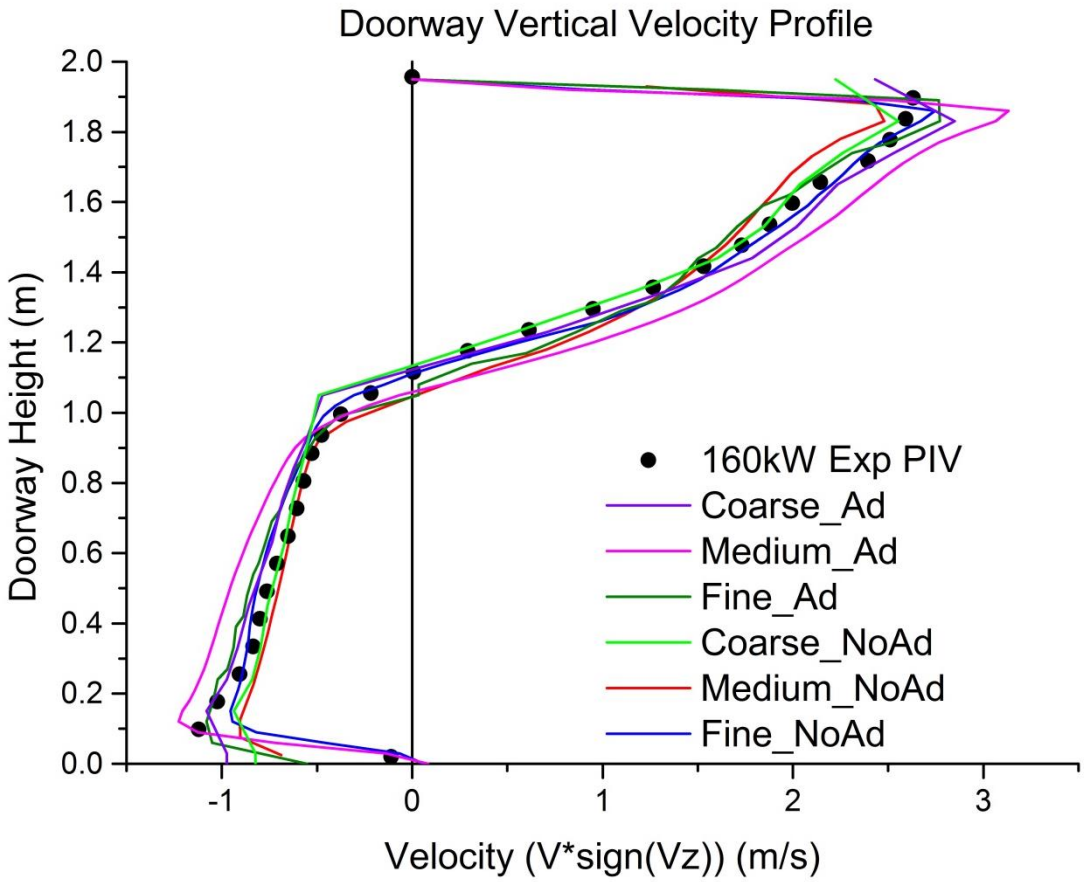

Figure 6.5: Mean velocity profile in the direction of the velocity's component V_Z, measured on the large scale compartment's doorway (160kW)

Figure 6.6 presents the mean velocity profile on the center of the doorway. The equation on the x-axis means that each value of the mean velocity that was computationally obtained, is presented with the sign of the V_Z component, expressing that way the direction of the flow. Negative values stand for inflow of fresh air while positive values stand for the outflow of hot gases.

It is pretty clear that almost all test cases follow the trend of the experimental data well. Estimated errors between the predictions and the experimental data are presented in Table 6.3. Table 6.3 does not reveal anything more than meets the eye. The Medium_Ad case is a little more far from the experimental values that the rest of the cases giving the fine mesh resolution cases the lead. Another interesting finding is the way the coarse simulations give better predictions of the velocity than the medium meshes, having double the cell size.

In Figure 6.6 the V_Z velocity component profiles are compared. Unfortunately data for the whole height of the door was not available but rather from 0.16m to 1.24m.

As expected the general trend of the lines is similar to that of Figure 6.5. A calculation of the absolute values' mean relative error between the experimental and computed values reveals the exact same results as before. Since the flow is buoyancy-driven, the temperature's profile shown in Figure 6.4 is

expected to reflect on the velocity profile, and especially on the W-component. Looking at the estimated error of the simulations in Table 6.3 shows exactly that. The Coarse_NoAd, Coarse_Ad and the Medium_Ad cases appear to have the greater values of error (>40%) while the rest remain close to each other, at lower values (<15%).

An interesting fact shown on this figure is the accuracy of the various cases in estimating the neutral plane's height. The results show better accuracy coming from the least expected cases since the poorest precision between the conductive models is given by the coarse and fine mesh, and the fine mesh between the adiabatic models.

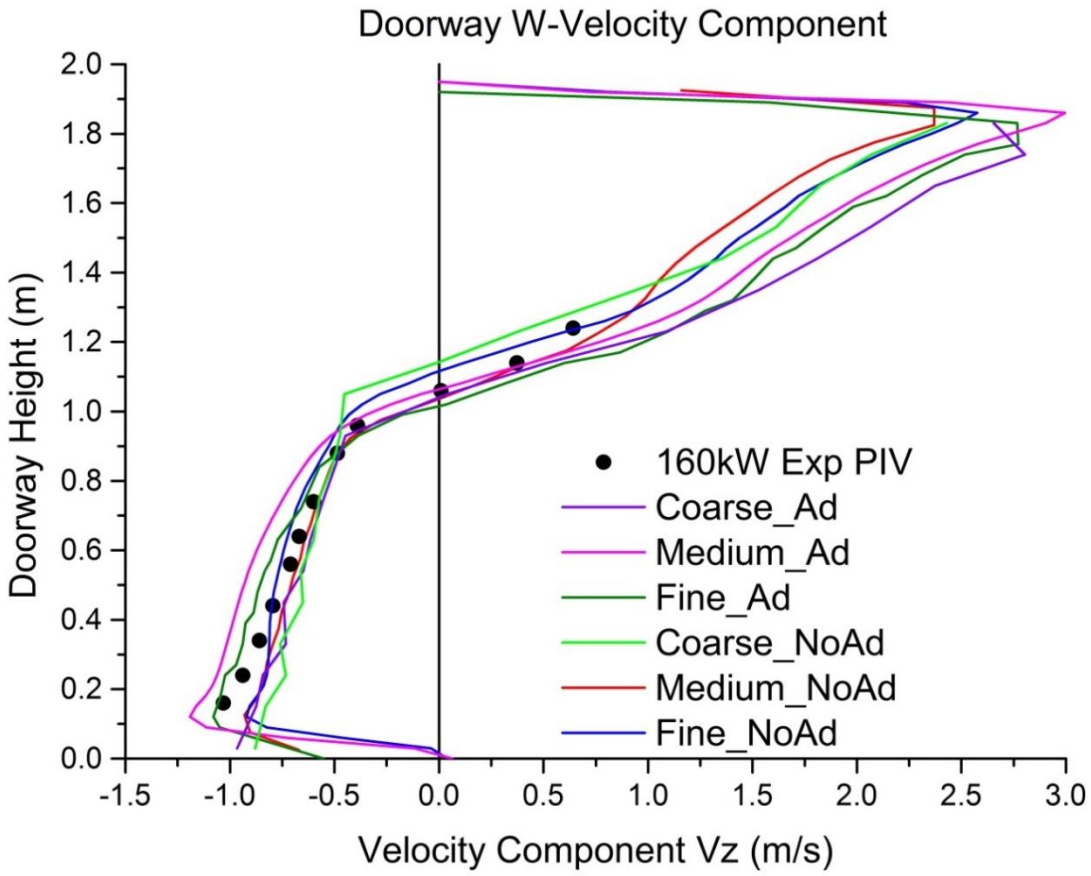

Figure 6.6: Velocity component W on the large scale compartment's doorway (160kW)

Velocity measurements were available in the literature for different door heights as well. The values that were obtained from the experiments represent the velocity component W measured at two certain heights (10% and 71% of the doorway height) using horizontal arrays of thermocouples. The lower measurements shown in Figure 6.7 are representative of the horizontal profile of the fresh air's velocity entering the compartment while the higher ones are representative of the horizontal profile the hot gases' velocity exiting the compartment through the doorway.

Experimental measurements were provided in the literature for the whole doorway's width. These values are shown in Figure 6.7 presented by the black symbols. The zero mark of the axis showing the door's width represents the center of the doorway.

The calculation of error estimates for each simulated case at each doorway height shows that the resulting values follow a distinct pattern for each examined case. More specifically, a case with a relatively small/large error value at the inflow zone does not show the same divergence from the experimental values in the outflow zone.

The pattern that seems to be followed in the results is that the medium-mesh cases tend to keep an almost constant error value for both directions of the flow. Contrary to that, the fine-mesh simulations show great variations of error between the two flow zones while the Coarse completely miss the experimental values in both zones except for the adiabatic case which describes the inflow profile perfectly.

In conclusion, the only significant findings that derive from this particular graph are the failure of the conductive coarse simulations to describe both the flow zones accurately and that the simulations using the fine and medium meshes lead to a better description of the experimental results of the outflow when using non-adiabatic properties for the walls of the compartment. For the inflow ($0.1*H_O$) the adiabatic simulations seem to give more accurate results while the conductive simulations clearly underestimated the velocity of the flow.

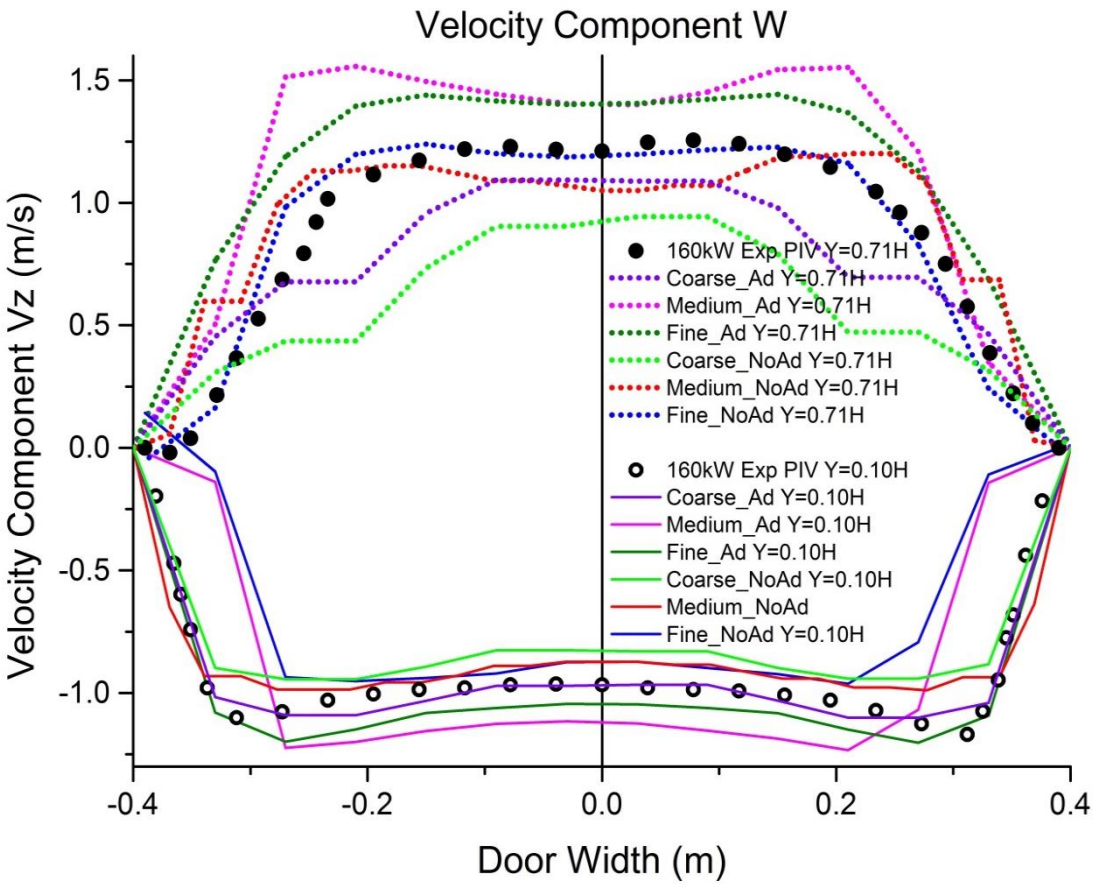

Figure 6.7: Velocity component W on the large scale compartment's doorway. Measurements are presented for two horizontal lines at the height of 0.195m ($y=0.10H_O$) and 1.3916m ($y=0.71H_O$).

Similar to Section 5.5, the simulations were compared in terms of average absolute error values deriving from the velocity measurements, standard deviation of the same values and relative standard deviation. All the necessary calculations were made using equations **(5.1)** and **(5.2)**. The absolute error

estimates are shown in Table 6.3. Line 8 of the table shows the average value of lines 4 to 7. The values that were calculated show an insignificant superiority of the non-adiabatic simulations. The most precise model is therefore decided in terms of the standard deviation values shown in column 8. Having half to one fifth the standard deviation of the adiabatic simulations, the "conductive" cases clearly outweigh the others being the most consistent. This is also supported by the coefficient of variation values, shown on the last line of the table.

Table 6.3: Calculation of the absolute error for all cases examined for the 160kW fire in a large scale compartment.

Large Scale Compartment - 160 kW						
Case	**Coarse_Ad**	**Medium_Ad**	**Fine_Ad**	**Coarse_NoAd**	**Medium_NoAd**	**Fine_NoAd**
Doorway Temperature (K)	3.89%	4.86%	4.19%	4.35%	2.80%	4.2%
Doorway V*sign(V_z) (m/s)	11.70%	30.10%	11.80%	9.20%	10.20%	12.60%
Doorway W-Velocity (m/s)	41.10%	75.70%	14.30%	50.30%	12.60%	13.60%
V_z at X=0.10H (m/s)	2.20%	21.10%	8%	13.50%	19.30%	24.40%
V_z at X=0.71H (m/s)	19.90%	17.70%	32.90%	38.00%	21.90%	11.60%
Velocity Absolute Error Average	18.70%	36.20%	16.80%	27.70%	16.00%	15.60%
Velocity Standard Deviation	0.1656	0.2688	0.1107	0.1964	0.055	0.0596
Relative Standard Deviation	0.89	0.74	0.66	0.71	0.34	0.38

The matter of mass flow rate estimation is also important just as with the small scale compartment experiment. The virtual devices used in FDS in this direction produced results which after being averaged over a certain time period as mentioned before, were compared to the experimental data. Table 6.4 presents those data validating the choice of the Fine_NoAd simulation as the most precise. The differences between the two extremes of the conductive cases are small, giving the lead to the Coarse_NoAd simulation, but the error values shown in Table 6.3 leave no choice but to consider the coarse model as inadequate in terms of accuracy.

Table 6.4: Calculation of the mass flow rate error for all cases examined for the 160kW fire in a large scale compartment.

Large Scale Compartment - 160 kW						
Case	**Coarse_Ad**	**Medium_Ad**	**Fine_Ad**	**Coarse_NoAd**	**Medium_NoAd**	**Fine_NoAd**
Mass Inflow Error	13.6%	-16%	6.1%	3.8%	-6%	-3.5%
Mass Outflow Error	-5.1%	-29%	-10.8%	-13%	-21%	-19.2%

6.5.2. Validation of the 320kW case

Bryant (2009b) experimented on a range of fires from 34kW to 511kW. The second and last case that will be compared to available experimental data for the given compartment in this study involves a fire of 320kW. The experimental data that is provided in the literature for this configuration is limited but enough for a validation of the computational results.

Three similar simulations were tested, different in terms of grid resolution as explained in Table 6.1.

Table 6.5 shows the absolute error average for each quantity, not taking the data obtained close to the neutral plane into account. This happens because at this specific height, changes in absolute values are relatively great leading a false evaluation of the rest of the experiment.

In the case of doorway temperature, the third line of the table reveals that the medium grid performed better that the other two, missing the doorway temperature by just 3.9%. Strangely, the coarse and fine simulations gave similar values in their results meaning that while the coarse test failed to estimate the temperature by 6.15%, the fine one missed it by 5.47%.

Since the doorway flow is buoyancy-driven, the velocity profiles are expected to reflect the results obtained by the temperature measurements. Figure 6.9 verifies that point showing a slight superiority of the medium and coarse grids at the lowest portion of the doorway and a small overestimation of it by the Fine_NoAd simulation.

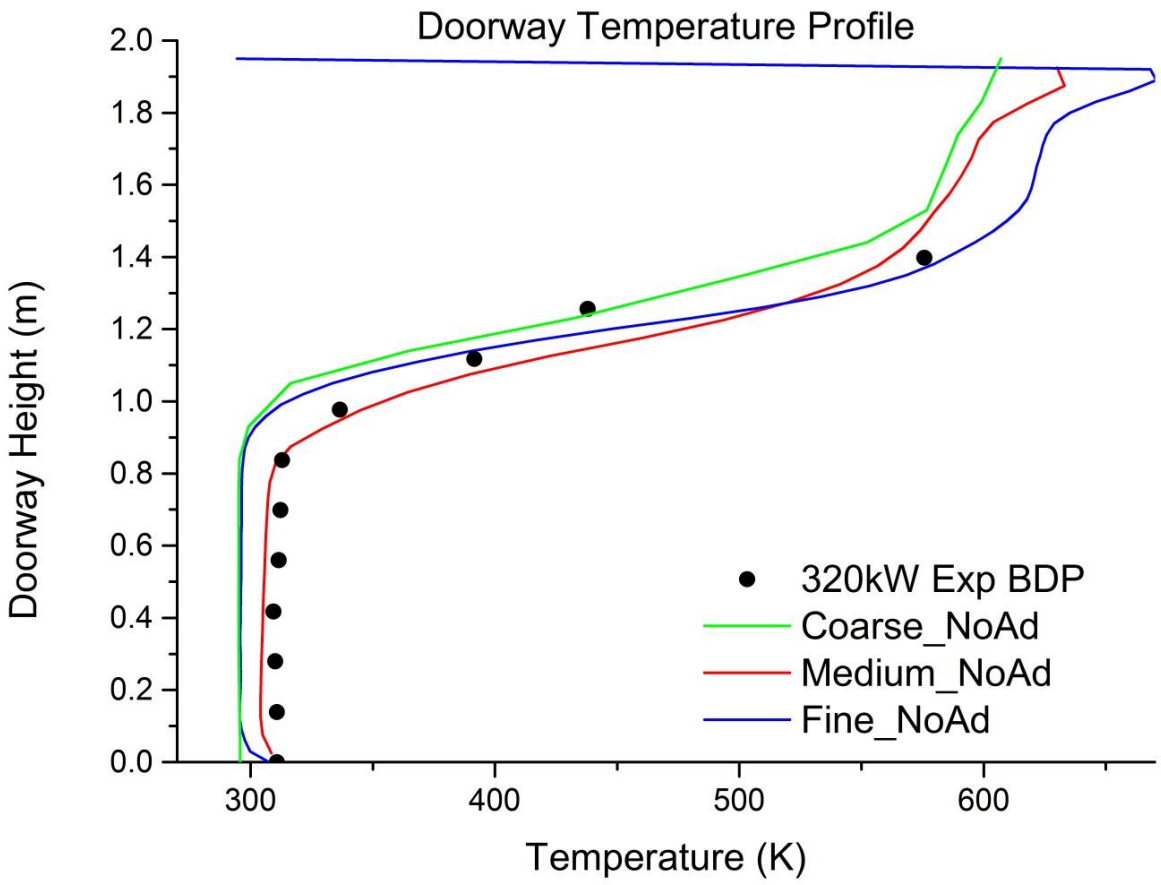

Figure 6.8: Temperature profile at the door of the large scale compartment (320kW)

At the highest part of the doorway, the trends are similar to those the temperature profiles, showing an agreement between the fine grid case's results and the experimental and the slight overestimation of the mean velocity by the coarse and medium grid simulations.

The estimation of absolute error for the mean velocity on the doorway shows a decline in the dominance of the medium grid simulation. The error estimation between the fine/medium mesh simulations and the experiment varies less than 1.4% which might be even lower if the simulations were repeated.

An important finding shown in Figure 6.9 is the almost perfect estimation of the neutral plane height by the simulation using the finest grid resolution. The correct estimation of the neutral plane can lead to a significantly better estimation of the mass in/outflow rate through the door which is a major goal of all CFD studies in this field.

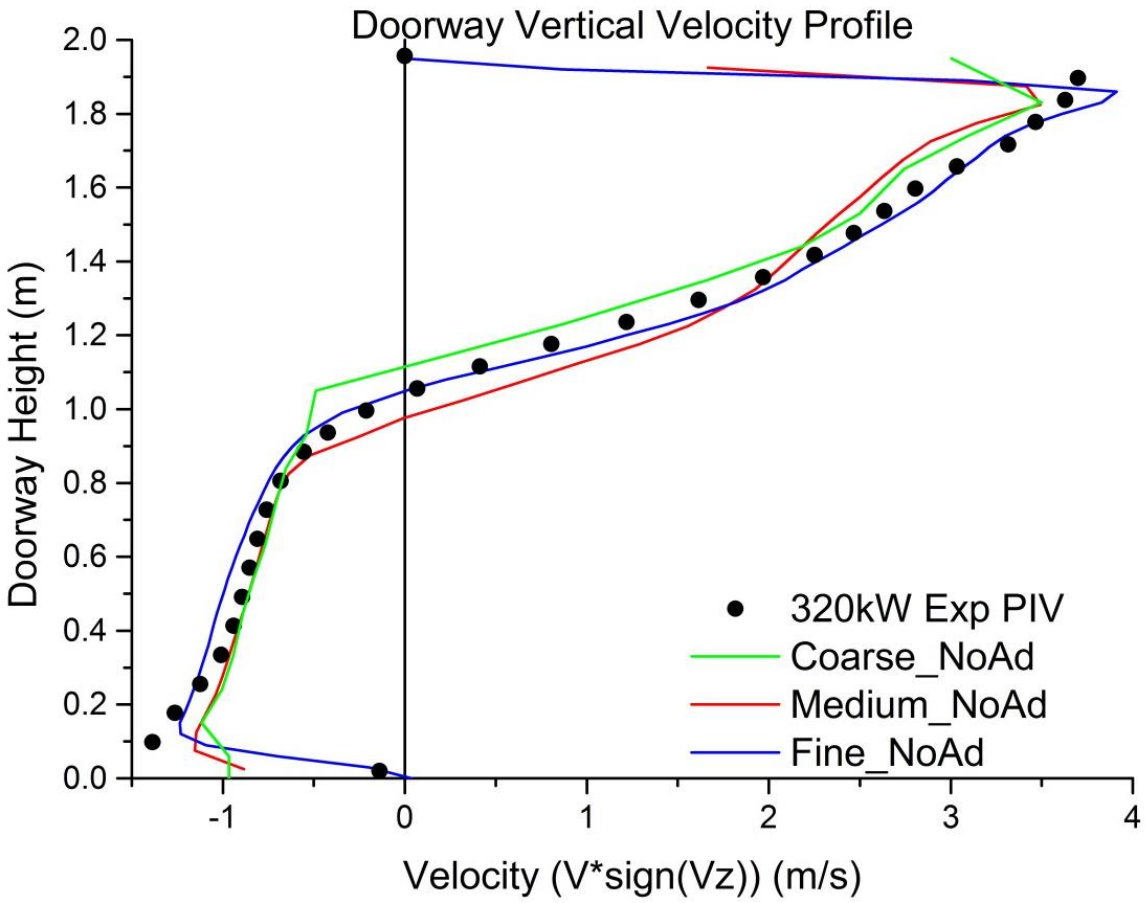

Figure 6.9: Mean velocity profile in the direction of the velocity's component V_Z, measured on the large scale compartment's doorway (320kW)

Figure 6.10 presents the V velocity component on the doorway of the three cases. The V_Z velocity component profile keeps the same shape as the mean velocity since the other components' contribution through the doorway plane is minor. The underestimation of the V_Z velocity component at both the lower and the upper part of the doorway is evident. Even though this is true for all the cases, the fine grid simulation gives better results except for the middle part of doorway height. Leaving the error estimates for the three points closer to the neutral plane height out of the overall results, the error estimates between the two most accurate cases' results vary by 4% as shown in Table 6.5.

Lines 6 and 7 of Table 6.5 show the average error calculation for the velocity results and their respective standard deviation. According to these values the reliability of the data is almost the same for all the simulations (using the coefficient of variation), giving the lead to the simulation using the fine mesh resolution. The overall best results of each table appear marked in grey color. This result comes to an agreement with the $D^*/\delta x$ criterion qualification at the first line of Table 6.2. The other two criteria on the same table describe all the mesh resolutions as adequate without taking the fire strength into account. Further investigation of this comparison might reveal interesting results.

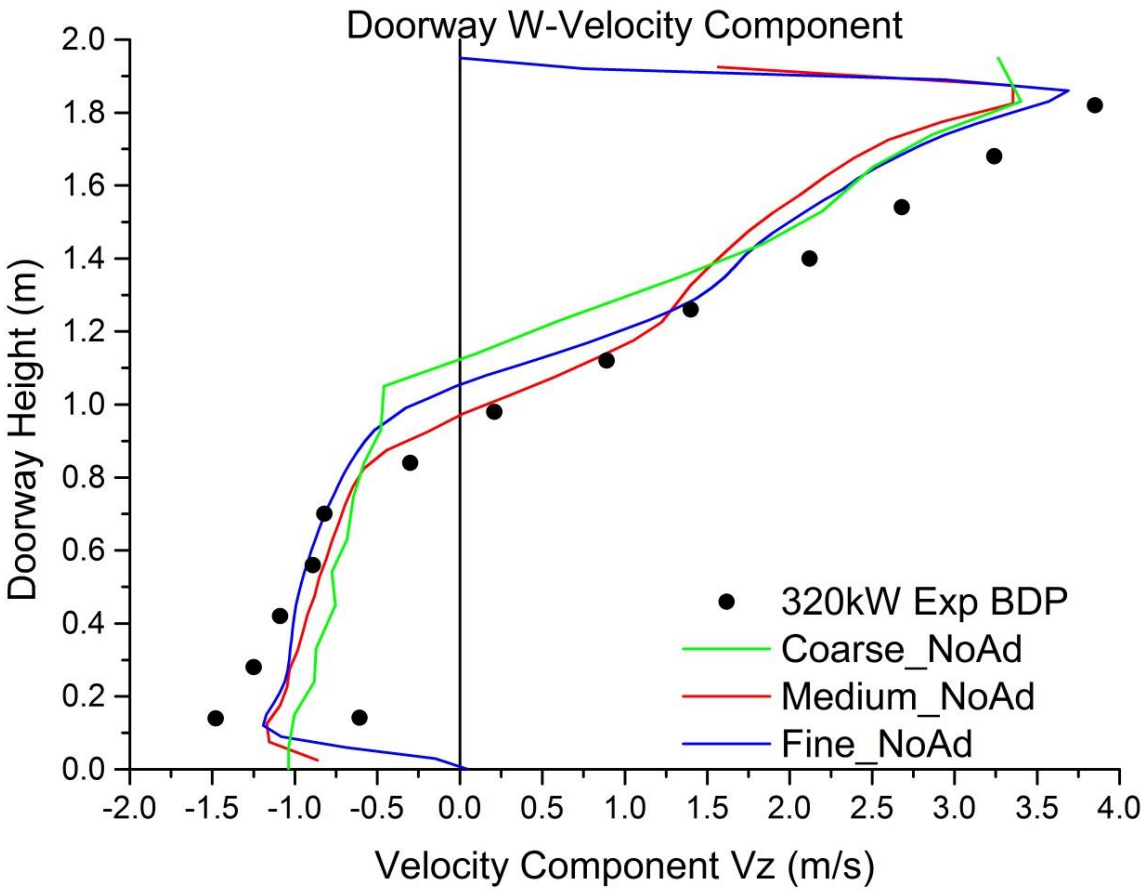

Figure 6.10: Velocity component W on the large scale compartment's doorway (320kW)

Table 6.5: Calculation of the absolute error for all cases examined for the 320kW fire in a large scale compartment.

Large Scale Compartment - 320 kW			
Case	**Coarse_NoAd**	**Medium_NoAd**	**Fine_NoAd**
Doorway Temperature (K)	6.15%	3.9%	5.47%
Doorway V*sign(V_z) (m/s)	14.40%	9.70%	8.34%
Doorway W-Velocity (m/s)	24.40%	16.20%	12.19%
Velocity Absolute Error Average	19.40%	12.90%	10.26%
Velocity Standard Deviation	0.0708	0.0458	0.0272
Relative Standard Deviation	0.36	0.36	0.26

Table 6.6 presents the error values obtained by the comparison between the computational and the experimental results. The best results appear to derive from the Medium_NoAd test. Since the difference between the mass flow rate error estimates of the medium and fine mesh simulation are small, the most precise test case appears to be the Fine_NoAd, showing a little over 20% lower average velocity error and 60% lower standard deviation from the Medium_NoAd simulation. This is again supported by the coefficient of variation (relative standard deviation) values, shown on the last line of Table 6.5.

Table 6.6: Calculation of the mass flow rate error for all cases examined for the 320kW fire in a large scale compartment.

Large Scale Compartment - 320 kW			
Case	**Coarse_NoAd**	**Medium_NoAd**	**Fine_NoAd**
Mass Inflow Error	1.5%	-6%	-6.5%
Mass Outflow Error	-14.8%	-18%	-21.5%

6.6. Main Flow Field Characteristics

The flow characteristics and values presented in the graphs and tables of the previous section point the Fine_NoAd simulation out as the most precise. That is, again, in terms of overall result quality both in temperature and velocity predictions as well as in terms of mass flow rate calculation.

In the same way as with the small scale compartment simulations, the flow field characteristics of the most accurate simulations will be presented in this chapter. The figures that follow present images reflecting certain quantities' evolution in the computational domains, obtained from the Smokeview utility provided with FDS. The time period/frame over which the images were obtained is chosen in order to introduce the viewer to a representative instance of the flow field.

Here, the thermal stratification effect difference between the two cases, shown in Figure 6.11, is very different from what was presented in the small scale compartment's results. The two layers are very clearly separated in the case of the strongest fire, while the 160kW simulation gives a "more mixed picture". This mixing picture shown is although misleading, since the temperature difference between the two layers is about 150^{o}K to over than 200^{o}K. The difference in temperature values reached at the doorway is close to 150^{o}K which means that the temperature difference of the hot gasses' zone is expected to give even larger values.

The combination of entrainment flow patterns developing inside the compartment and the radiation of the hot gasses leads to a lower zone (cold inflow gasses) of higher temperature as well. The entrainment phenomena are depicted in the figure but will later be better described by the next figures.

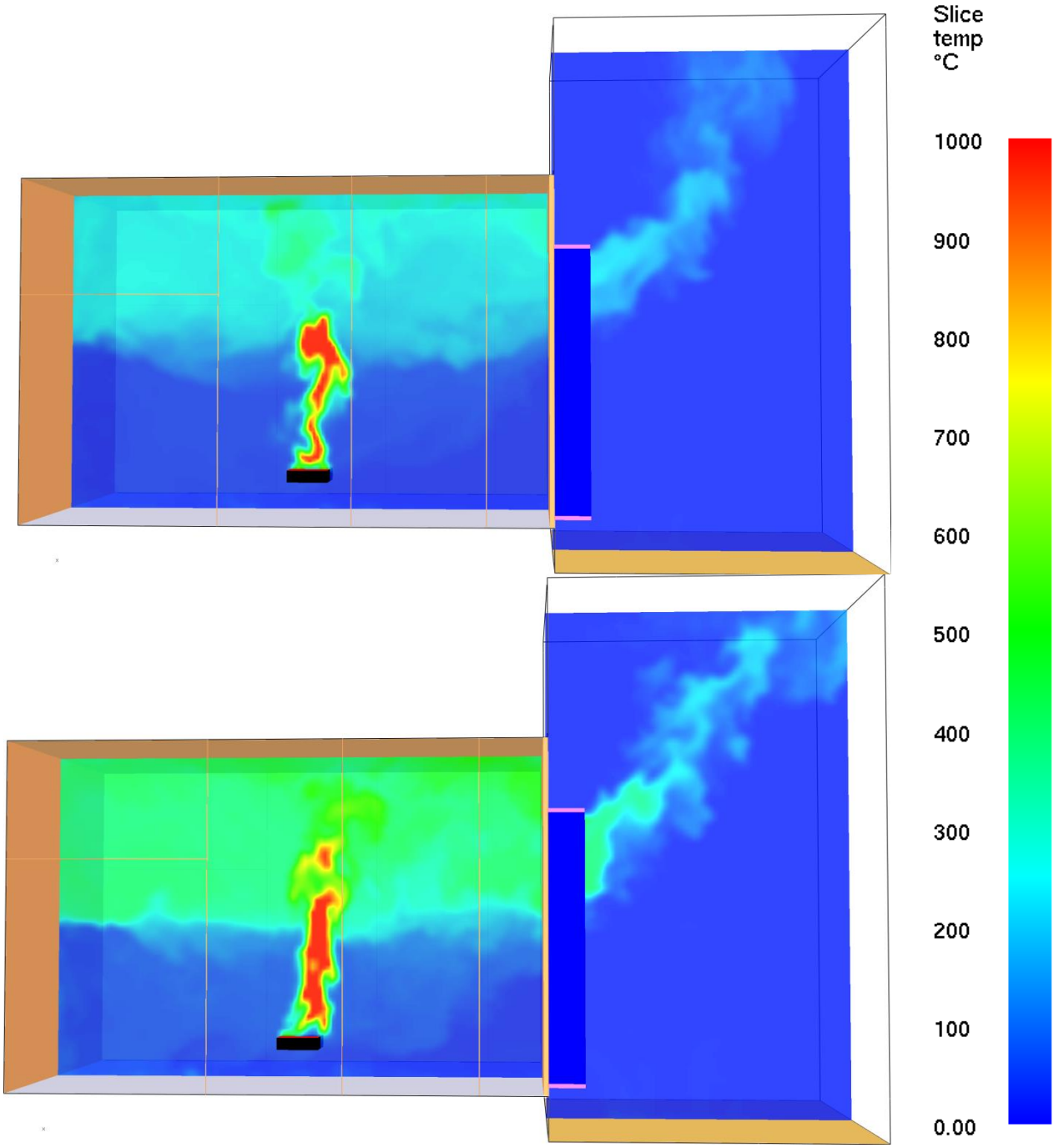

Figure 6.11: Temperature contours for the *Fine_NoAd* 160kW (top) and the *Fine_NoAd* 320kW (bottom) test cases.

The entrainment flow inside the room behind the doorway is made evident in Figure 6.12. The neutral plane appears to be close to the 50-60% mark of the doorway height in the two cases, found at the height were the color change between red and blue appears.

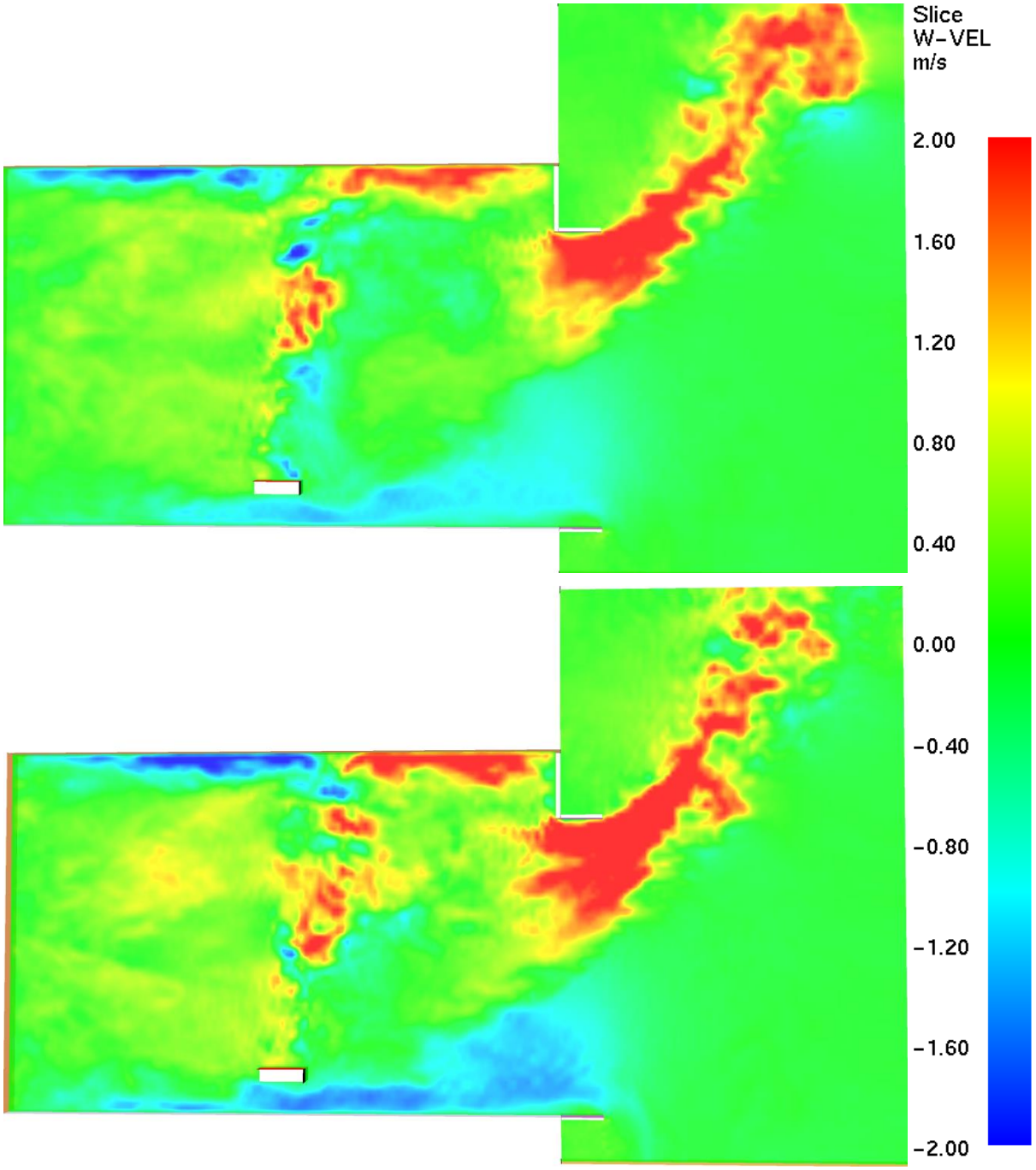

Figure 6.12: Velocity component W contours for the *Fine_NoAd* 160kW (top) and the *Fine_NoAd* 320kW (bottom) test cases.

The mixing in the back of the room is significantly stronger in the 320kW simulation, while this will be more clearly shown by a following figure comparison. The same is true for the ceiling jet streams shown in the two compared figures, where the stronger the fire is, the more intense the jet is.

The intensity of the flow is shown clearly in Figure 6.13. Here, the recirculation found behind the burner seems more homogenous in the free space of the 160kW case for the two gases' layers. This is also true for the area between the doorway and the burner as well, where the 320kW case shown in the bottom picture reveals significantly stronger turbulences between the outflow and the inflow layers.

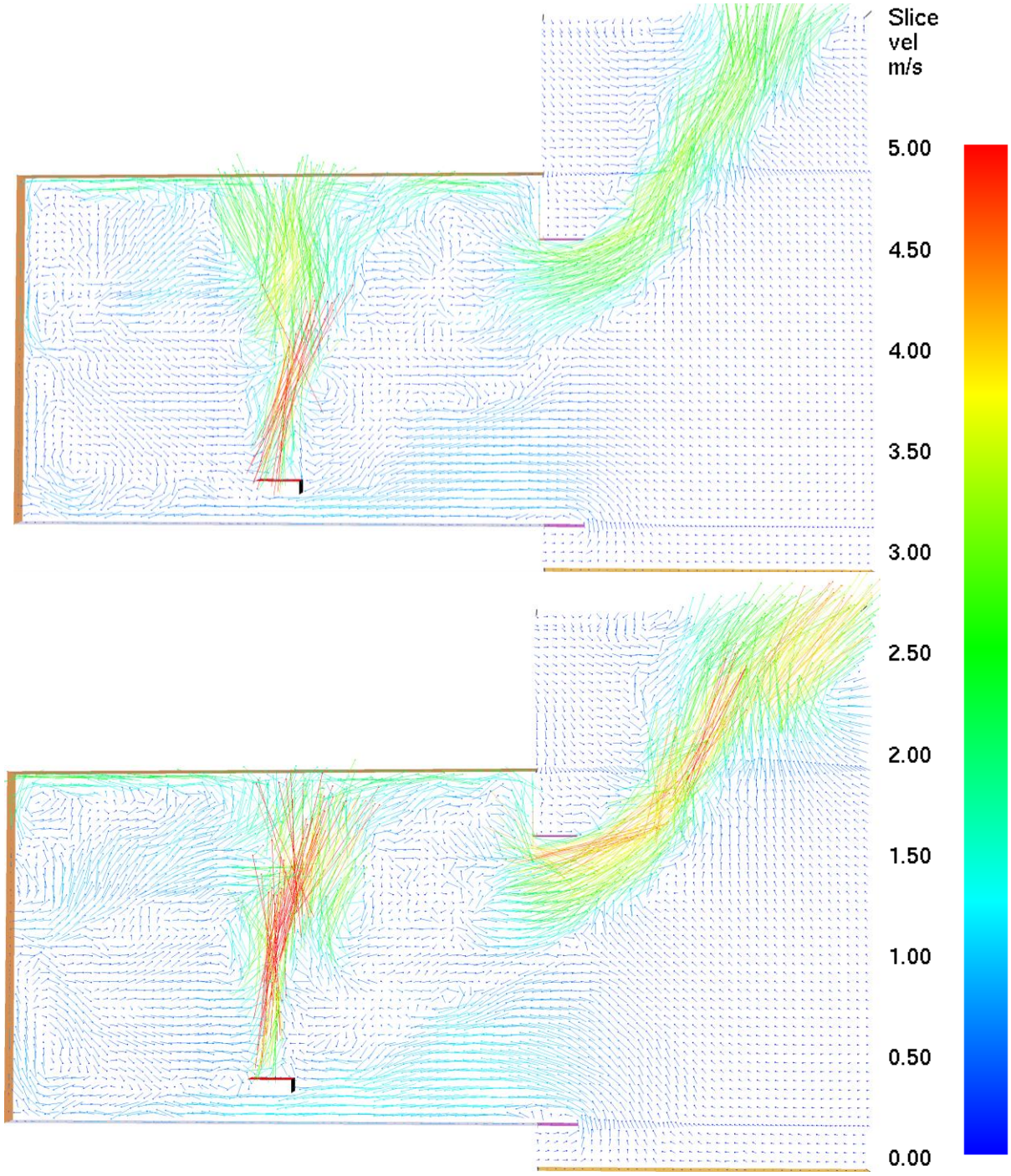

Figure 6.13: Mean velocity vectors for the *Fine_NoAd* 160kW (top) and the *Fine_NoAd* 320kW (bottom) test cases.

The vena contracta appears to be formed more smoothly in the 320kW case, which is expected since the flow is stronger keeping a rigid pattern. The bottom picture also shows the flow pattern causing the almost perfect thermal stratification appearing in Figure 6.11. The recirculation flows appearing on either side of the burner, lead the respective gas layer into confinement, allowing the plume jet to drive the gas mixing process. For that reason, four separate areas of different flow patterns could be distinguished, meaning the division of the compartment's domain in areas under/over the thermal stratification height and in front of/behind the burner.

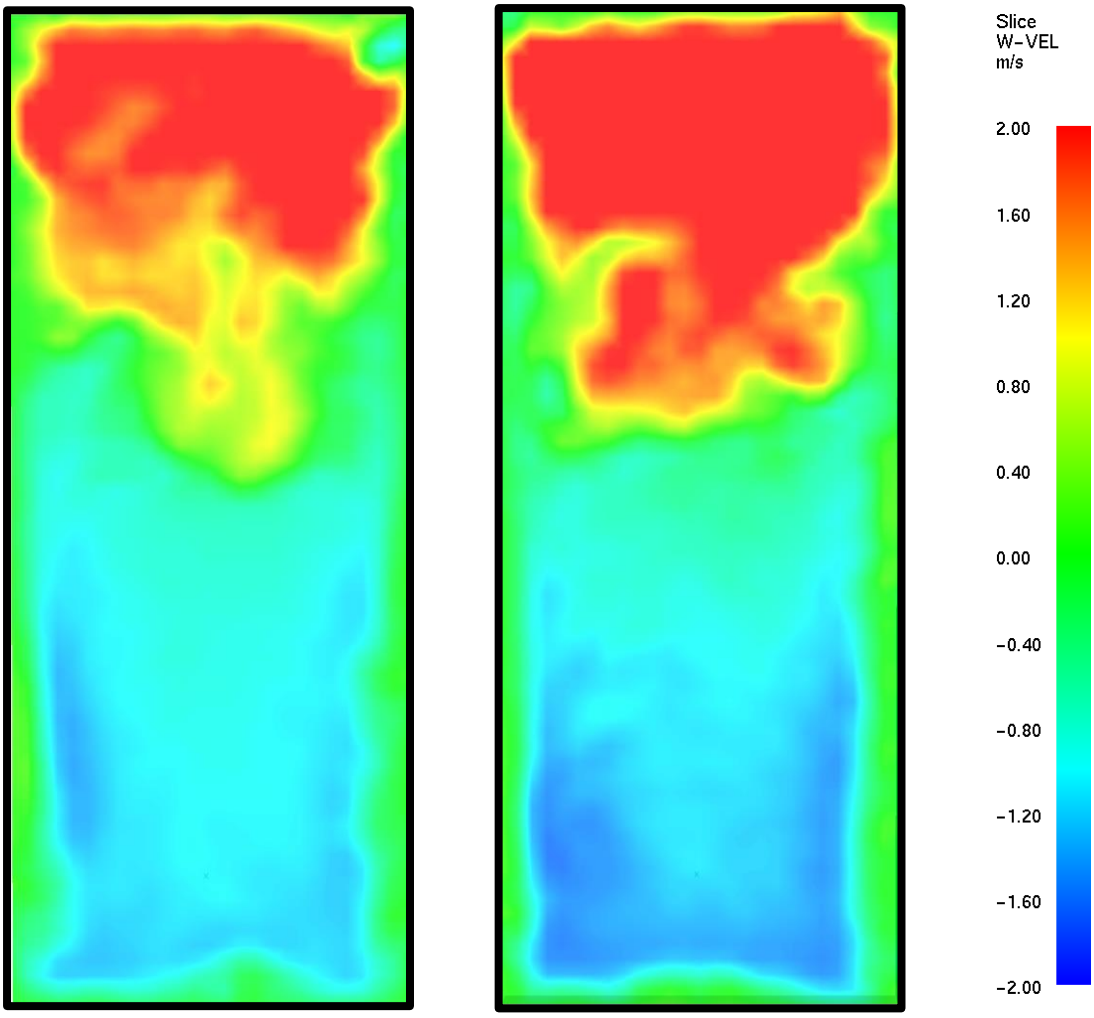

Figure 6.14: Velocity component W contour on the large scale compartment's doorway for the *Fine_NoAd* 160kW (left) and the *Fine_NoAd* 320kW (right) test cases.

Figure 6.14 presents a contour of the velocity component W on the doorway plane, meaning the velocity component with a direction perpendicular to the doorway plane. Again, the two images present solely doorway plane, as viewed from the outside. The orange-red color on the top portion of the contours reveals the direction of the flow towards the ambient space (outflow of hot gases), while the green-blue color on the bottom portion of the door shows the direction of the flow into the compartment.

It is evident, that the two cases present the neutral plane at different heights. The velocity contour of the 320kW simulation is darker revealing that mainly the outflow is more intense in this test, reaching a lower height. The velocity profiles shown also reveal that the flow on either side of the doorways is asymmetrical. That explains the asymmetries found in the figures presented in the Validation of the 160kW case above.

7. Assessment of Opening Mass Flow Rate Correlations

The necessity of accurate prediction of the flow through doors or windows due to compartment fires is important for many reasons. In that direction, it is necessary to evaluate the results' accuracy and consistency by comparison to experimental data.

Correlations provided in the literature have been presented and analyzed in section 2.4. The use of these correlations demands proper use of variables expressing the vent's discharge coefficient. Since different sets of constants have been used in the literature for the inflow and outflow coefficients, it is necessary to evaluate the precision of these sets in estimating the mass flow rate through the vent. For that reason, the following comparisons are presented utilizing different pairs of these constants, as proposed in the literature. The values will be evaluated in pairs (sets of C_{IN} and C_{OUT}) rather than separately, since in some cases the estimation of the mass flow rate out of the compartment is strongly dependent on the result of a correlation providing the mass flow rate towards the inside of the compartment. The sets of values that will be used for the discharge coefficients (C_d) are presented in Table 7.1.

Table 7.1: Discharge coefficients' values, used in the parametric study.

C_{IN}	0.7	0.68	0.68
C_{OUT}	0.7	0.68	0.73

The percentages shown in the tables that follow represent the relative error between the computational and the experimental values. The experimental values were obtained by integration of the mass flow on the doorway of each experimental facility and are shown in the second line of each table. The third line of each table shows the strength of the fire used in each particular experiment while the first line shows the origin of the expected mass flow rate value. The third line of the tables also shows the kind of vent used in the experimental configuration. The experiments using heat release rates equal to 62.9kW and 105.3kW can be traced in Steckler's work (Steckler et al, 1982) as "Test 18" and "Test 20" respectively.

The last two columns of each table present the statistical quantities of absolute average and standard deviation of the values on their left.

Table 7.2 presents the mass flow rate into the compartment, using a coefficient of C_{IN}=0.7. The values obtained by the proper calculation of the provided correlations have been compared to the experimental values of mass flow rate through the door resulting in the percentages shown. The most precise results appear marked in grey color, as is the code name of the corresponding correlation.

Table 7.2: Relative error of predicted air mass flow rate entering the compartment for C_{IN}=0.7

Origin:	Suard et al (2015)	Suard et al (2015)	Steckler et al (1982)	Steckler et al (1982)	Bryant (2011)	Bryant (2011)	Absolute Average	Standard Deviation
Mass Flow Rate	0.0417 kg/s	0.04999 kg/s	0.533 kg/s	0.618 kg/s	0.7033 kg/s	0.8170 kg/s		
Correlation	**15.5kW Doorway**	**21.7kW Doorway**	**62.9kW Doorway**	**105.3kW Doorway**	**160kW Doorway**	**320kW Doorway**		
IN1	41%	-4%	45%	45%	27%	-4%	28%	0.195
IN2	20%	11%	-18%	-56%	16%	18%	23%	0.164
IN3	70%	29%	68%	68%	56%	34%	54%	0.183
IN4	24%	17%	4%	6%	23%	26%	17%	0.095
IN5	19%	10%	1%	3%	15%	17%	11%	0.075
IN6	43%	19%	31%	32%	34%	25%	31%	0.082
IN7	39%	4%	45%	36%	26%	-1%	25%	0.186
IN8	54%	26%	58%	41%	42%	21%	40%	0.147
IN9	63%	36%	66%	48%	54%	33%	50%	0.136
FDS	1.4%	8.2%	-	-	-3.5%	-6.5%	4.9%	0.030

FDS simulations gave the most precise results, although no simulation was performed regarding the experiments conducted by Steckler et al (1982). The overall best results amongst the correlations examined appear highlighted in the tables. Correlation IN5 shows the least averaged error value, with the lowest deviation between its' values as well.

Table 7.3 shows the respective mass outflow rate error percentages when C_{IN}=0.7 and C_{OUT}=0.7. Correlation OUT2 is found to estimate the mass flow rate out of the compartment the most accurately showing the smallest range of error values compared to the other correlations.

Table 7.3: Relative error of predicted air mass flow rate exiting the compartment for C_{IN}=0.7, C_{OUT}=0.7

Origin:	Suard et al (2015)	Suard et al (2015)	Steckler et al (1982)	Steckler et al (1982)	Bryant (2011)	Bryant (2011)	Absolute Average	Standard Deviation
Mass Flow Rate	0.05393 kg/s	0.04959 kg/s	0.567 kg/s	0.630 kg/s	0.8347 kg/s	0.9619 kg/s		
Correlation	**15.5kW Doorway**	**21.7kW Doorway**	**62.9kW Doorway**	**105.3kW Doorway**	**160kW Doorway**	**320kW Doorway**		
OUT1	20%	18%	57%	49%	19%	-5%	28%	0.203
OUT2	-7%	12%	-2%	1%	-3%	0.3%	4%	0.045
OUT3	12%	44%	-15%	-49%	-4%	5%	22%	0.199
OUT4	19%	27%	54%	38%	20%	3%	27%	0.175
OUT5	3%	31%	8%	-9%	7%	10%	11%	0.099
FDS	-13.4%	-2.8%	-	-	-19.2%	-21.5%	14%	0.083

The results of the same comparisons using C_{IN}=0.68 can be found in Table 7.4. Correlation IN5 once more shows the lowest value of standard deviation between the correlations, meaning that it has the most homogenous results. It is worth noting that the second best results come from correlation IN4, having though almost double average error and an almost 50% greater standard deviation.

In the last line, the FDS simulations appear to have the lowest value of standard deviation in addition to the lowest average value, giving a very precise estimation regarding the mass flow rate into the compartment.

Table 7.4: Relative error of predicted air mass flow rate entering the compartment for C_{IN}=0.68

Origin:	Suard et al (2015)	Suard et al (2015)	Steckler et al (1982)	Steckler et al (1982)	Bryant (2011)	Bryant (2011)	Absolute Average	Standard Deviation
Mass Flow Rate	0.0417 kg/s	0.04999 kg/s	0.533 kg/s	0.618 kg/s	0.7033 kg/s	0.8170 kg/s		
Correlation	**15.5kW Doorway**	**21.7kW Doorway**	**62.9kW Doorway**	**105.3kW Doorway**	**160kW Doorway**	**320kW Doorway**		
IN1	37%	-6%	41%	41%	24%	-6%	26%	0.166
IN2	17%	8%	-21%	-57%	12%	15%	22%	0.179
IN3	65%	25%	63%	63%	51%	30%	50%	0.178
IN4	24%	17%	4%	6%	23%	26%	17%	0.095
IN5	16%	7%	-2%	0%	12%	14%	9%	0.066
IN6	38%	16%	28%	28%	30%	22%	27%	0.075
IN7	39%	4%	45%	36%	26%	-1%	25%	0.186
IN8	54%	26%	58%	41%	42%	21%	40%	0.147
IN9	63%	36%	66%	48%	54%	33%	50%	0.136
FDS	1.4%	8.2%	-	-	-3.5%	-6.5%	4.9%	0.030

Table 7.5 shows mass outflow rate error percentages when C_{IN}=0.68 and C_{OUT}=0.68. As before, correlation OUT2 is the most precise, with correlation OUT5 in the second place. The catalytic difference between the two -added to the 3% greater average error-, giving OUT2 the lead, is the standard deviation value of correlation OUT5 standing just below three times that of OUT2.

Table 7.5: Relative error of predicted air mass flow rate exiting the compartment for C_{IN}=0.68, C_{OUT}=0.68

Origin:	Suard et al (2015)	Suard et al (2015)	Steckler et al (1982)	Steckler et al (1982)	Bryant (2011)	Bryant (2011)	Absolute Average	Standard Deviation
Mass Flow Rate	0.05393 kg/s	0.04959 kg/s	0.567 kg/s	0.630 kg/s	0.8347 kg/s	0.9619 kg/s		
Correlation	**15.5kW Doorway**	**21.7kW Doorway**	**62.9kW Doorway**	**105.3kW Doorway**	**160kW Doorway**	**320kW Doorway**		
OUT1	17%	15%	53%	45%	16%	-8%	26%	0.185
OUT2	-10%	9%	-4%	-2%	-5%	-3%	6%	0.033
OUT3	9%	41%	-17%	-50%	-7%	2%	21%	0.198
OUT4	19%	27%	54%	38%	20%	3%	27%	0.175
OUT5	0%	27%	5%	-12%	4%	7%	9%	0.096
FDS	-13.4%	-2.8%	-	-	-19.2%	-21.5%	14%	0.083

The mass outflow rate error percentages have also been calculated for the pair of discharge coefficients when C_{IN}=0.68, C_{OUT}=0.73 and are presented in Table 7.6. Once again, correlation OUT2 is by far the most precise. It is noticeable though that the FDS simulations present the second most consistent relative error values.

Table 7.6: Relative error of predicted air mass flow rate exiting the compartment for C_{IN}=0.68, C_{OUT}=0.73

Origin:	Suard et al (2015)	Suard et al (2015)	Steckler et al (1982)	Steckler et al (1982)	Bryant (2011)	Bryant (2011)	Absolute Average	Standard Deviation
Mass Flow Rate	0.05393 kg/s	0.04959 kg/s	0.567 kg/s	0.630 kg/s	0.8347 kg/s	0.9619 kg/s		
Correlation	**15.5kW Doorway**	**21.7kW Doorway**	**62.9kW Doorway**	**105.3kW Doorway**	**160kW Doorway**	**320kW Doorway**		
OUT1	25%	23%	64%	55%	24%	-1%	32%	0.233
OUT2	-3%	17%	3%	5%	2%	5%	6%	0.056
OUT3	14%	48%	-13%	-48%	-2%	7%	22%	0.206
OUT4	19%	27%	54%	38%	20%	3%	27%	0.175
OUT5	7%	37%	13%	-5%	12%	15%	15%	0.115
FDS	-13.4%	-2.8%	-	-	-19.2%	-21.5%	14%	0.083

The comparisons made above help clear the field of which is the most precise way in determining the mass flow rate -of air/gasses- entering or exiting the compartment. Another comparison can be made in order to determine the most suitable value of the discharge coefficient in general. In order to achieve that, the second from right column of each table (absolute average values) will be averaged as an attempt to express the mean error resulting from the use of the particular value of C_d.

Table 7.7 and Table 7.8 present the described procedure, regarding the mass inflow and outflow rates' error values respectively. Note that only the correlations making use of the discharge coefficients appear in the tables.

Table 7.7: Mean average error estimation of mass inflow rate correlations when C_{IN}=0.68 and C_{IN}=0.7

Average error of all 6 experiments		
Correlation	**C_{IN}=0.68**	**C_{IN}=0.7**
IN1	26 %	28 %
IN2	22 %	23 %
IN3	50 %	54 %
IN5	9 %	11 %
IN6	27 %	31 %
Average	**26.8%**	**29.4%**
Standard Deviation	**0.1482**	**0.1573**

Since there are none but minuscule differences in both mean average and standard deviation values, it would be superficial and pointless to try and pick one of the two values of the coefficient as more suitable. The same is true for the results of Table 7.8 presenting the same statistic quantities for the discharge coefficients regarding the flow exiting the compartment.

The couple of C_{IN}=0.68 and C_{OUT}=0.68, first proposed by Prahl and Emmons (1975), shows a very slight dominance over the remaining two values' couples. The reader should not disregard the accuracy needed when substituting all the variables needed by the correlations, such as the neutral plane and thermal stratification heights (discontinuity height Z_D) for a precise calculation and evaluation of the deriving results. This accuracy could be the key to a more exact comparison.

Table 7.8: Mean average error estimation of mass outflow rate correlations for all three sets of the discharge coefficients

Average error of all 6 experiments			
Correlation	**C_{IN}=0.68 C_{OUT}=0.68**	**C_{IN}=0.7 C_{OUT}=0.7**	**C_{IN}=0.68 C_{OUT}=0.73**
OUT1	26%	28%	32%
OUT2	6%	4%	6%
OUT3	21%	22%	22%
OUT5	9%	11%	15%
Average	**15.5%**	**16.3%**	**18.8%**
Standard Deviation	**0.0954**	**0.1078**	**0.1100**

The estimation of the thermal discontinuity height Z_D is a problem often met in the literature. Many attempts towards its' precise estimation have been made, using both empirical and semi-empirical correlations. Most of the existing correlations demand the prior estimation of either the mass outflow rate or the mass inflow rate or worse, both. One correlation, provided by Rockett (1976), utilizes the mean temperature values of the two zones and the height of the neutral plane in a third degree polynomial equation (Equation (7.1)) to predict the height of Z_D.

$$\frac{T_{amb}}{T_{out}}\left(\frac{1}{Z_N}-1\right)^3=\left(1-\frac{Z_D}{Z_N}\right)\left(1+\frac{Z_D}{2Z_N}\right)^2\left(1+\frac{\dot{m}_{fuel}}{\dot{m}_{in}}\right)^2 \tag{7.1}$$

The last factor on the right hand side of the equation is generally considered to be equal to 1, since the mass flow rate of the fuel is close to zero. Following this principle, equation (7.2) is obtained. This exact correlation was the one used in the present study in order to calculate the value of Z_D needed in the mass in/outflow rate correlations.

$$\frac{T_{amb}}{T_{out}}\left(\frac{1}{Z_N}-1\right)^3=\left(1-\frac{Z_D}{Z_N}\right)\left(1+\frac{Z_D}{2Z_N}\right)^2 \tag{7.2}$$

The only way to assess the results of the equation mentioned above is to compare it to experimental values. In that direction the experiments conducted by Steckler et al (1982) positioning the burner in the center of the compartment, are used to compare the analytical to the experimental values. The researchers provided measurements of all the data needed for the analytical expression as well as measurements of the thermal discontinuity height. The first column of Table 7.9 shows the test cases' numbers, as described by Steckler et al (1982). The second column describes the relative height of the doorway expressed as a fraction of 1.83m. The third column shows the exact height of the thermal discontinuity plane as measured during the experiments, and the last column shows the estimated height difference as a percentage of "divergence" from the experimental value. The divergence expresses the relative error between the two values, signed negatively when the correlation underestimates the height or positively when it overestimates the height.

The correlation provided by Rockett (1976) does not take the existence of a sill at the bottom of the vent in to account and should therefore not be used for cases using windows as the only vent of the enclosure.

The final result shows a -13.5% relative error in the estimation of the thermal discontinuity height. Bearing that in mind, the reader should consider that a more precise way of obtaining the data needed by the correlations for the mass in/outflow rate, would most definitely lead to more accurate predictions.

Table 7.9: Relative error of the correlation provided for the estimation of the thermal discontinuity height (Z_D)

Test No.#	Case	Experimentally determined Z_D – (Steckler et al, 1982)	Relative error using Rockett's (1976) correlation [Equation (7.2)]
10	2/6 Door	0.91317	**-0.50%**
11	3/6 Door	0.94062	**-14.05%**
12	4/6 Door	0.97173	**-16.51%**
612	4/6 Door	0.98088	**-13.11%**
13	5/6 Door	1.01016	**-11.08%**
14	6/6 Door	1.02846	**-13.21%**
18	6/6 Door	1.02663	**-7.73%**
710	6/6 Door	1.01748	**-20.60%**
810	6/6 Door	1.01931	**-19.61%**
16	7/6 Door	1.04859	**-14.01%**
17	8/6 Door	1.06506	**-15.80%**
19	6/6 Door	1.04127	**-12.76%**
20	6/6 Door	1.00101	**-16.53%**
21	6/6 Door	0.97905	**-13.68%**
Average Error (of doorway cases)			**-13.5%**

8. Summary and Conclusions

This study focuses on the CFD simulation of opening flows in compartment fires. It is concerned with the evaluation and validation of both computational simulations' results and the results obtained from correlations provided by the literature, compared to experimental data. Effort was put into the most accurate simulation of the flow field phenomena, while achieving optimum agreement between numerical and experimental data.

Numerical simulations utilizing the FDS code were performed, including parametric study in terms of grid size resolution, heat release rates and thermal wall thermal boundary conditions. The results of the simulations were compared to the respective experimental values indicating the most accurate configurations, while keeping the required computational time cost low. The simulations included fires of heat release rate from 15.5kW to 320kW. The comparison between the different grid sizes and ambient space grid extensions contributed in the evaluation of three mesh resolution criteria and the confirmation of the grid extension in the ambient area criterion. The extension of the computational grid was guided to be at least equal to one hydraulic diameter of the vent. The computational mesh resolution comparisons proved the 10mm cell to be the most accurate for the small scale compartment fire and the 30mm cell to be the most accurate for the large scale compartment fire. All the simulations' comparisons showed an overall failure of the test cases using adiabatic wall properties to predict the mass flow rate accurately.

Correlations estimating the mass flow rate through a compartment's vent were gathered, examined and grouped, written in a homogenous simplified format (Section 2.4). The results of the correlations for each experiment were compared in terms of absolute relative error to the results of the simulations. Statistical analysis of the correlations determined that a correlation provided by Tewarson (1984) was able to give the overall best prediction of the mass flow rate into the compartment, overestimating the mass flow rate by 9% to 11%. Having 4.9% relative error value, the FDS simulations proved to perform better than any correlation in the estimation of the mass flow rate entering the compartment. In terms of flow out the compartment, correlation OUT2 performed overall better, having a mean absolute error of 4% to 6%.

All the mean absolute error values of the mass flow rate estimation techniques were examined, in order to shed light on the issue of which discharge coefficient values' set is the most proper for the case of a compartment fire using a doorway as a single vent. The value of 0.68 for both the inflow and outflow (Prahl and Emmons, 1975) showed a doubtful better behavior than the remaining two. This validation process could easily be refined by using better estimates of the variables needed by the correlations. The estimation of the thermal discontinuity height inside the compartment is one variable used above that needs significant improvement. The correlation of Rockett (1976) proved to underestimate the thermal discontinuity height by 13.5% leading to accumulated computational error showing in the final results. This value was acquired after comparing the correlation's results to experimental values provided by Steckler et al (1982).

None of the above analytical processes and problems explains the failure of the FDS simulations to give better mass flow rate estimations for the gasses exiting the compartment. Future work utilizing the effects of radiation in the simulations' results might aid in that direction, combined with an a posteriori analysis of the grid size effects in the results of the simulation. Higher simulation duration periods than the ones used in the present study might reveal change in the final results.

9. References

1. Argyropoulos C.D., Markatos N.C., Recent advances on the numerical modelling of turbulent flows, Applied Mathematical Modelling 39 (2015) 693–732.
2. Audouin L., Chandra L., Consalvi J.-L., Gay L., Gorza E., Hohm V., Hostikka S., Ito T., Klein-Hessling W., Lallemand C., Magnusson T., Noterman N., Park J.S., Peco J., Rigollet L., Suard S., Van-Hees P., Quantifying differences between computational results and measurements in the case of a large-scale well-confined fire scenario, Nuclear Engineering and Design 241 (2011) 18–31.
3. Awbi H.B., Nemri M.M., Scale Effect in Room Airflow Studies, Energy and Buildings, 14 (1990) 207-210.
4. Awbi H.B., Air Movement in Naturally-Ventilated Buildings, Renewable Energy, Volume 8, Issues 1–4 (1996) 241–247.
5. Babrauskas V., Williamson R.B., Post-flashover Compartment Fires: Basis of a Theoretical Model, Fire and Materials, Vol. 2, No. 2 (1978) 39-53.
6. Babrauskas V., Estimating Room Flashover Potential, Fire Technology (1980) 94-103.
7. Beyler C.L., SFPE Classic Paper Review: Fire-induced Flow Through an Opening by Joseph Prahl and Howard W. Emmons, Journal of Fire Protection Engineering, Vol. 14, No.2 (2004) 95-100.
8. Bryant R.A., Particle Image Velocimetry Measurements of Buoyancy Induced Flow through a Doorway, National Institute of Standards and Technology Internal/Interagency Report 7252 (2005).
9. Bryant R.A., A comparison of gas velocity measurements in a full-scale enclosure fire, Fire Safety Journal 44 (2009a) 793–800.
10. Bryant R.A., The application of stereoscopic particle image velocimetry to measure the flow of air into an enclosure containing a fire, Experiments in Fluids (2009b).
11. Bryant R.A., Evaluating practical measurements of fire-induced vent flows with stereoscopic PIV, Proceedings of the Combustion Institute 33 (2011) 2481–2487.
12. Cetegen B.M., Zukoski E.E., Kubota T., Entrainment in the Near and Far Field of Fire Plumes, Combustion Science and Technology, Vol. 39 (1984) 305-331.
13. Chamberlain G.A., Persaud M.A., Wighus R., Drangsholt G., Blast and Fire Engineering for Topside Structures. Test Programme F3, Confined Jet and Pool Fires. Final Report, SINTEF Report NBL A08102, Norwegian Fire Research Laboratory (2008).
14. Chow W.K., Application of Computational Fluid Dynamics in Building Services Engineering, Building and Environment, Vol. 31, No. 5 (1996) 425-436.
15. Chow W.K., Air pumping action of a plume in a room fire, Building Simulation, Vol. 6, No. 1 (2013) 95-102.
16. Crocker J.P., The effect of sprinkler sprays on fire on fire induced doorway flows, M.Sc. Thesis, Department of Fire Protection Engineering, WPI, Worcester, MA (2008)
17. Delichatsios M.A., Procedure for Calculating the Air Entrainment into Turbulent Pool and Jet Fires, Journal of Fire Protection Engineering, Vol. 2(3) (1990) 93-98.
18. Dembsey N.A., Pagni P.J., Williamson R.B., Compartment Fire Near-field Entrainment Measurements, Fire Safety Journal 24 (1995) 383-419.
19. Emmons H.W., Vent Flows, SFPE Handbook of Fire Protection Engineering, 3rd Ed., Section 2, Chapter 3, 32-41 (2002).

20. Ferng Y.M., Lin C.H., Investigation of appropriate mesh size and solid angle number for CFD simulating the characteristics of pool fires with experiments assessment, Nuclear Engineering and Design 240 (2010) 816–822.
21. Gutiérrez-Montes C., Sanmiguel-Rojas E., Burgos M.A., Viedma A., On the fluid dynamics of the make-up inlet air and the prediction of anomalous fire dynamics in a large-scale facility, Fire Safety Journal 51 (2012) 27–41.
22. Hasib R., Kumar R., Shashi, Kumar S., Simulation of an experimental compartment fire by CFD, Building and Environment 42 (2007) 3149–3160.
23. He Y., Measurement of doorway flow field in multi-enclosure building fires, International Journal of Heat and Mass Transfer 42 (1999) 3253-3265.
24. He Y., Jamieson C., Jeary A., Wang J., Effect of Computation Domain on Simulation of Small Compartment Fires, Fire Safety Science, Proceedings of the Ninth International Symposium (2008) 1365-1376.
25. Heselden A.J.M., Fire Problems of Pedestrian Precincts Part 1. The Smoke Production of Various Materials, Fire Research Station, Fire Research Note No.856 (1971).
26. Himoto K., Tsuchihashi T., Tanaka Y., Tanaka T., Modeling thermal behaviors of window flame ejected from a fire compartment, Fire Safety Journal 44 (2009) 230–240.
27. Hoffmann N., Markatos N. C., Thermal Radiation Effects on Fires in Enclosures, Applied Mathematical Modelling 12 (1988).
28. Hoffmann N., Galea E.R., Markatos N.C., Mathematical modelling of fire sprinkler systems, Applied Mathematical Modelling 13 (1989).
29. Hostikka S., McGrattan K.B., Hamins A., Numerical Modeling of Pool Fires Using LES and Finite Volume Method for Radiation, Fire Safety Science – Proceedings of the Seventh International Symposium (2003) 383-394.
30. Hostikka S., Development of fire simulation models for radiative heat transfer and probabilistic risk assessment, VTT Publications 683, VTT Technical Research Centre of Finland, Espoo, Finland, (2008).
31. Hu L., Zhang X., Zhang X., Yang L., A re-examination of entrainment constant and an explicit model for flame heights of rectangular jet fires, Combustion and Flame Vol. 161, Issue 11 (2014) 3000–3002.
32. Ierardi J.A., Barnett J.R., A Quantitative Method for Calibrating CFD Model Calculations, Proceedings of the CIB-CTBUH International Conference on Tall Buildings (2003).
33. ISO 9705, Fire tests—full-scale room test for surface products. International Organization for Standardization, Geneva, Switzerland (1993).
34. Jia F., Galea E.R., Patel M.K., The numerical simulation of fire spread within a compartment using an integrated gas and solid phase combustion model, Journal of Applied Fire Science, Vol. 8, Issue 4 (1998) 327-352.
35. Jiang Y., Chen Q., Buoyancy-driven single-sided natural ventilation in buildings with large openings. International Journal of Heat and Mass Transfer, Vol. 46 (2003) 973-988.
36. Johansson N., Van Hees P., A Simplified Relation Between Hot Layer Height and Opening Mass Flow, Fire Safety Science – Draft Proceedings of the Eleventh International Symposium (2014).
37. Johansson N., Svensson St., Van Hees P., An evaluation of two methods to predict temperatures in multi-room compartment fires, Fire Safety Journal 77 (2015) 46-58.
38. Karlsson B., Quintiere J.G., Pressure Profiles and Vent Flows for Well-Ventilated Enclosures, Enclosure Fire Dynamics (1999).
39. Kawagoe K., Fire Behaviour in Rooms, Building Research Institute, Report No. 27, Japan (1958)

40. Koched A., Prétrel H., Vauquelin O., Audouin L., Experimental Determination of the Discharge Coefficient of a Doorway Using the SPIV Technique for Fire-Induced Flow Applications, Proceedings of the thirteenth international Fire Science & Engineering Conference (2013) 229–240.
41. Koched A., Prétrel H., Vauquelin O., Audouin L., Experimental determination of the discharge flow coefficient at a doorway for fire induced flow in natural and mixed convection, Fire and Materials (2014) 114-128.
42. Lacour S., Porterie B., Loraud J.C., Morvan D., Modelling of Fire-Induced Flow in Enclosures, Computational Fluid Dynamics Journal, Vol.6, No.4 (1998) 53-69.
43. Lapuerta C., Suard S., Babik F., Rigollet L., Validation process of ISIS CFD software for fire simulation, Nuclear Engineering and Design 253 (2012) 367– 373.
44. Lee Yee-Ping, Delichatsios M.A., Ohmiya Y., The physics of the outflow from the opening of an enclosure fire and re-examination of Yokoi's correlation, Fire Safety Journal 49 (2012) 82–88.
45. Lewis M.J., Moss M.B., Rubini P.A., CFD Modelling of Combustion and Heat Transfer in Compartment Fires, Fire Safety Science – Proceedings of the Fifth International Symposium (1997)463-474.
46. Lin C.H., Ferng Y.M., Hsu W.S., Investigating the effect of computational grid sizes on the predicted characteristics of thermal radiation for a fire, Applied Thermal Engineering 29 (2009) 2243–2250.
47. Lucchesi C., Vauquelin O., Prétrel H., Bournot Ph., Doorway flow from a reduced scale isothermal air/helium approach, International Journal of Thermal Sciences 50 (2011) 1920-1929.
48. Ma T.G., Quintiere J.G., Numerical simulation of axi-symmetric fire plumes: accuracy and limitations, Fire Safety Journal 38 (2003) 467–492.
49. Madrzykowski D., Vettori R.L., Simulation of the Dynamics of the Fire at 3146 Cherry Road NE Washington D.C., May 30, 1999, Report by the National Institute of Standards and Technology (2000).
50. Markatos N.C., Malin M.R., Cox G., Mathematical Modelling of Buoyancy-Induced Smoke Flow in Enclosures, Int. Journal Heat Mass Transfer, Vol. 25, No. 1 (1982) 63-75.
51. Markatos N.C., Pericleous K.A., Cox G., A Novel Approach to the Field Modelling of Fire, PCH PhysicoChemical Hydrodynamics Vol. 7, No. 2/3 (1986) 125-143.
52. Markatos N.C., Kotsifaki C.A., One-dimensional, two-fluid modelling of turbulent premixed flames, Applied Mathematical Modelling 18 (1994).
53. McCaffrey B.J., Rockett J.A., Static pressure measurements of enclosure fires, Journal of Research of the National Bureau of Standards 82 (1977) 107–117.
54. McCaffrey B.J., Purely Buoyant Diffusion Flames: Some Experimental Results, National Institute of Standards and Technology (1979).
55. McCaffrey B.J., Momentum Implications for Buoyant Diffusion Flames, Combustion and Flame (1983) 52: 149-167.
56. McGrattan K., Hostikka S., McDermott R., Floyd J., Weinschenk C., Overholt K., Fire Dynamics Simulator, Sixth Edition, Technical Reference Guide: Validation, National Institute of Standards and Technology Special Publication 1018-3, Vol. 3 (2015a)
57. McGrattan K., McDermott R., Weinschenk C., Fire Dynamics Simulator, Sixth Edition, User Guide, National Institute of Standards and Technology Special Publication 1019 (2015b)
58. Melis St., Audouin L., Effects of Vitiation on the Heat Release Rate in Mechanically- Ventilated Compartment Fires, Fire Safety Science – Proceedings of the Ninth International Symposium (2008) 931-942.

59. Merci B., Vandevelde P., Experimental study of natural roof ventilation in full-scale enclosure fire tests in a small compartment, Fire Safety Journal 42 (2007) 523–535.
60. Merci B., Van Maele K., Numerical simulations of full-scale enclosure fires in a small compartment with natural roof ventilation, Fire Safety Journal 43 (2008) 495–511.
61. Nakaya I., Tanaka T., Yoshida M., Steckler K., Doorway Flow Induced by a Propane Fire, Fire Safety Journal, 10 (1986) 185 – 195.
62. Peacock R.D., Forney G.P., Reneke P.A., CFAST - Consolidated Model of Fire Growth and Smoke Transport (Version 6) Technical Reference Guide, National Institute of Standards and Technology Special Publication 1026r1 (2011).
63. Pierce J.B.M., Moss J.B., Smoke production, radiation heat transfer and fire growth in a liquid-fuelled compartment fire, Fire Safety Journal 42 (2007) 310–320.
64. Prahl J., Emmons H.W., Fire Induced Flow through an Opening, Combustion and Flame 25 (1975) 369-385.
65. Prétrel H., Querre Ph., Forestier M., Experimental Study of Burning Rate Behaviour in Confined and Ventilated Fire Compartments, Fire Safety Science – Proceedings of the Eighth International Symposium (2005) 1217-1228.
66. Prétrel H., Vauquelin O., Candelier F., Brunner A., Effect of vertical density stratification on the buoyancy-induced flow at a doorway opening, Journal of Fire Sciences, Vol. 32(4) (2014) 295–315.
67. Quintiere J.G., McCaffrey B.J., Harkleroad M., The Burning of Wood and Plastic Cribs in an Enclosure, National Institute of Standards and Technology, Vol. 2 (1980).
68. Quintiere J.G., Rinkinen W.J., Jones W.W., The Effect of Room Openings on Fire Plume Entrainment, Combustion Science and Technology, Vol 26 (1981) 193-201.
69. Quintiere J.G., Steckler K., Corley D., An Assessment of Fire Induced Flows in Compartments, Fire Science and Technology, Vol. 4, No. 1 (1984) 1-14.
70. Quintiere J.G., Fundamentals of Enclosure Fire "Zone" Models, Journal of Fire Protection Engineering, Vol. 1(3) (1989) 99-119.
71. Quintiere J.G., Fire Behavior in Building Compartments, Proceedings of the Combustion Institute, Vol. 29 (2002) 181–193.
72. Quintiere J.G., Wang L., A general formula for the prediction of vent flows, Fire Safety Journal 44 (2009) 789–792.
73. Rockett J.A., Fire Induced Gas Flow in an Enclosure, Combustion Science and Technology Vol. 12 (1976) 165-175.
74. Stavrakakis G.M., Markatos N. C., Simulation of Airflow in One- and Two-room Enclosures Containing a Fire Source, International Journal of Heat and Mass Transfer 52 (2009) 2690–2703.
75. Steckler K.D., Quintiere J.G., Rinkinen W.J., Flow Induced by Fire in a Compartment, Proceedings of the Nineteenth Symposium (International) on Combustion/The Combustion Institute (1982) 913-920.
76. Steckler K.D., Baum H.R., Quintiere J.G., Fire Induced Flows through Room Openings – Flow Coefficients, Twentieth Symposium (International) on Combustion/The Combustion Institute (1984) 1591-1600.
77. Suard S., Koched A., Prétrel H., Audouin L., Numerical simulations of fire-induced doorway flows in a small scale enclosure, International Journal of Heat and Mass Transfer 81 (2015) 578–590.
78. Tang F., Hu L.H., Wang Q., Lu K.H., Yang L.Z., An experimental investigation on temperature profile of buoyant spill plume from under-ventilated compartment fires in a reduced pressure atmosphere at high altitude, International Journal of Heat and Mass Transfer 55 (2012) 5642–5649.

79. Tewarson A., Fully Developed Enclosure Fires of Wood Cribs, Twentieth Symposium (International) on Combustion/The Combustion Institute (1984) 1555-1566.
80. Thomas P.H., Heselden A.J.M., Law M., Fully-developed Compartment Fires –Two Kinds of Behaviour, Fire Research Technical Paper No. 18 (1967)
81. Thomas P.H., Two-Dimensional Smoke Flows from Fires in Compartments: Some Engineering Relationships, Fire Safety Journal 18 (1992) 125-137.
82. Utiskul Y., Theoretical and Experimental Study on Fully-Developed Compartment Fires, Ph.D. Thesis, University of Maryland (2006).
83. Walton W.D., Thomas Ph.H., Estimating Temperatures in Compartment Fires, SFPE Handbook of Fire Protection Engineering, 3rd Ed., Section 3, Chapter 6, 171-188 (2002).
84. Wang J., Hua J., Kumar K., Kumar S., Evaluation of CFD Modeling Methods for Fire-induced Airflow in a Room, , Journal of Fire Sciences 24 (2006) 393-411.
85. Wang L., Quintiere J.G., An analysis of compartment fire doorway flows, Fire Safety Journal 44 (2009) 718–731.
86. Wang L., Lim J., Quintiere J.G., On the prediction of fire-induced vent flows using FDS, Journal of Fire Sciences 30(2) (2011) 110-121.
87. Wang Z., Jia F., Galea E.R., Patel M.K., Ewer J., Simulating one of the CIB W14 round robin test cases using the SMARTFIRE fire field model, Fire Safety Journal 36 (2001) 661-677.
88. Wen J.X., Huang L.Y., CFD modelling of confined jet fires under ventilation-controlled conditions, Fire Safety Journal 34 (2000) 1-24.
89. Xiao B., Comparison of Numerical and Experimental Results of Fire Induced Doorway Flows, Fire Technology 48 (2012) 595–614.
90. Xue H., Ho J.C., Cheng Y.M., Comparison of different combustion models in enclosure fire simulation, Fire Safety Journal 36 (2001) 37-54.
91. Yeoh G.H., Yuen R.K.K., Chen D.H., Kwok W.K., Combustion and Heat Transfer in Compartment Fires, Numerical Heat Transfer, Part A (2002) 42: 153-172.
92. Yeoh G.H., Yuen R.K.K., Chueng S.C.P., Kwok W.K., On modelling combustion, radiation and soot processes in compartment fires, Building and Environment 38 (2003) 771 – 785.
93. Yii Ee. H., Fleischmann Ch.M., Buchanan A.H., Vent Flows in Fire Compartments with Large Openings, Journal of Fire Protection Engineering, Vol. 17 (2007) 211-237.
94. Zhang X., Yang M., Wang J., He Y., Effects of Computational Domain on Numerical Simulation of Building Fires, Journal of Fire Protection Engineering (2010) 225-251.
95. Zhao G., Beji T., Merci B., Application of FDS to Under-Ventilated Enclosure Fires with External Flaming, Fire Technology (2015).